VISCOUS FLOW AROUND A CIRCULAR CYLINDER NEAR A PLANE WALL

KNUT INGE ENGELBRETH

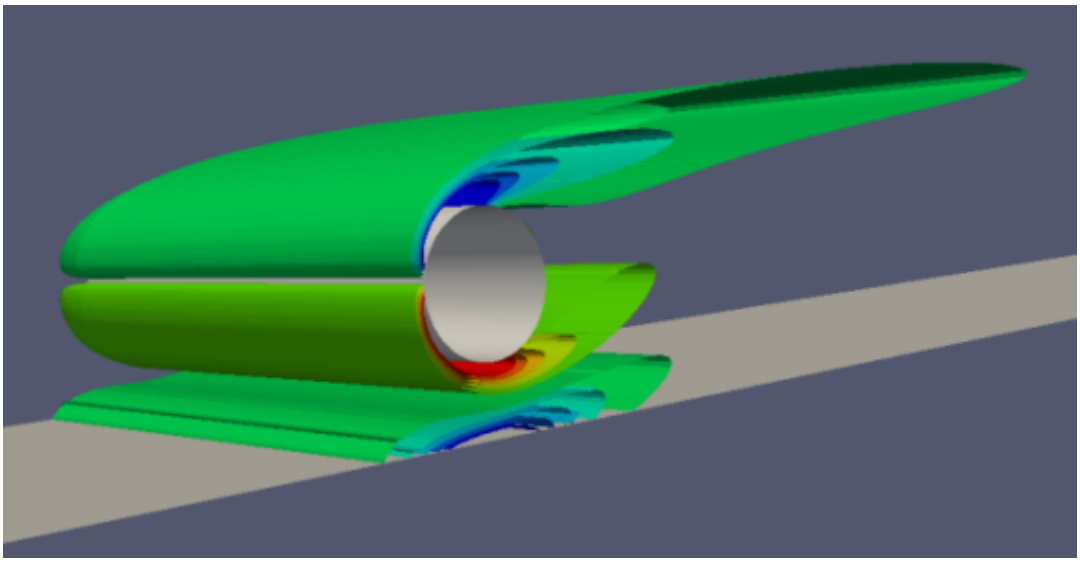

MASTER THESIS

Marine Hydrodynamics

NTNU – Trondheim
Norwegian University of
Science and Technology

Department of Marine Technology
Norwegian University of Science and Technology (NTNU)

June 2011

NTNU
Norges teknisk-naturvitenskapelige universitet
Institutt for marin teknikk

HOVEDOPPGAVE I MARIN HYDRODYNAMIKK

VÅR 2011

FOR

Stud.techn. Knut Inge Engelbreth

VISKØS STRØMNING OMKRING EN SIRKULÆR SYLINDER NÆR EN PLAN FLATE
(Viscous flow around a circular cylinder near a plane wall)

Kandidaten skal bruke programsystemet OpenFOAM til å simulere viskøs strømning omkring sirkulær sylinder. Viktige numeriske parametere undersøkes og valg som gjøres dokumenteres. Sylinderen bringes nær en fast horisontal flate (rørledning nær havbunn) med en innkommen strøm hvor det kan tas hensyn til grensesjiktet langs flaten. Detaljerte analyser med forskjellig grid (oppløsning og fordeling) gjøres 2D, og for et utvalg parametere gjøres også 3D simuleringer.
I den grad tiden tillater det undersøkes også forskjellige geometrier på flaten under sylinderen. Det legges vekt på en god resultatpresentasjon med visualisering av de fysiske størrelsene.

Kandidaten skal i besvarelsen legge frem sitt personlige bidrag til løsning av de problemer som oppgaven stiller. Påstander og konklusjoner som legges frem, skal underbygges med matematiske utledninger og logiske resonnementer der de forskjellige trinn tydelig fremgår. I besvarelsen skal det klart fremgå hva som er kandidatens eget arbeid, og hva som er tatt fra andre kilder.
Kandidaten skal utnytte de muligheter som finnes til å skaffe seg relevant litteratur for det problemområdet kandidaten skal bearbeide.
Besvarelsen skal være oversiktlig og gi en klar fremstilling av resultater og vurderinger. Det er viktig at teksten er velskrevet og klart redigert med tabeller og figurer. Besvarelsen skal gjøres så kortfattet som mulig, men skrives i klart språk.
Besvarelsen skal inneholde oppgaveteksten, forord, innholdsfortegnelse, sammendrag, hoveddel, konklusjon med anbefalinger for videre arbeid, symbolliste, referanser og eventuelle vedlegg. Alle figurer, tabeller og ligninger skal nummereres.
Det forutsettes at Institutt for marin teknikk, NTNU, fritt kan benytte seg av resultatene i sitt forskningsarbeid, da med referanse til studentens besvarelse.

Besvarelsen leveres i to eksemplar innen 14. juni 2011.

Bjørnar Pettersen
Professor

Faglig veileder: Stipendiat Mia Prsic

Abstract

Marine pipelines placed at or near the seabed are exposed to currents and waves. In the presence of a sedimentary seabed, the interaction between the surrounding water motions and the pipeline may cause erosion of sediments beneath the pipeline. Due to this erosion or due to the installation procedure, free spans may occur in sections along the span of the pipeline. A simplified description of the flow is obtained by approximating the seabed as a plane and impermeable wall. Most of the previous experimental and numerical studies on this flow are performed at Reynolds numbers, Re, in the range 10^3-10^5 as this range is of most relevance for offshore engineering purposes. Numerical modeling at such Reynolds numbers generally involves different kinds of artificial flow modeling.

In this study, the software OpenFOAM is applied for numerical simulations of the viscous flow around a circular cylinder at $Re = 100$. At this Reynolds number the flow around an unconfined circular cylinder is characterized by vortex shedding and yet turbulence is avoided, which provides the possibility of accurate calculations of the flow. The flow is investigated with reference to visualizations of pressure, velocity and vorticity; and the flow characteristics are quantified in terms of drag and lift acting on the cylinder and vortex shedding frequency. Numerical simulations of an unconfined cylinder in uniform cross-flow constitutes the basis of the present study, and these simulations are included in an attempt to validate the results and the applied computational method. The results for this flow are within the scatter of the reported values in the literature.

In this study, the flow around a cylinder near a plane wall is of main interest. Three different gap ratios $G/D = 0.2; 0.5; 1.0$ are applied. The results are generally in accordance with published data from numerical simulations; best agreement is found at $G/D = 0.2$ and $G/D = 0.5$. The results are supportive to the suggestion of vortex shedding suppression to be caused by the interaction between the lee-side recirculating flow and the gap flow, which inhibits large-scale vortex roll-up. Further, the results at $G/D = 1.0$ indicates cancellation of opposite signed vorticity in the near-wall region, in accordance with suggestions in the literature.

Additionally, the geometry of the wall is altered, introducing a hollow below the cylinder. This shape imitates a fully developed scour profile. These simulations are expected to bring new results to this topic of research. The flow is characterized by evident vortex shedding. Further, at this gap a distinct mean lift in the direction towards the wall is observed and both the drag coefficient and the frequency of vortex shedding is reduced as compared to the flow around a cylinder in uniform cross-flow. The obtained results exhibits similarity to published experimental data for the flow at $Re = 1 \cdot 10^4$.

Two-dimensional simulations are performed for all of the flow configurations, and a few three-dimensional simulations are performed for a cylinder in uniform cross-flow and a cylinder located a distance $G/D = 0.5$ from a plane wall. Due to the two-dimensional flow patterns, insignificant differences are found between the two-dimensional and three-dimensional simulations.

In this study, emphasize is given to the influences on the solution of the following numerical parameters: time step, domain size, grid geometry, element size and element spacing. These parameters are thoroughly investigated in terms of convergence studies.

Also included in this thesis is a review of some features of these flows and an overview of the governing equations, OpenFOAM and the applied solver `icoFoam`.

Preface

This is the final result of my master thesis work in marine hydrodynamics at the Department of Marine Technology at the Norwegian University of Science and Technology (NTNU).

The software OpenFOAM which is applied in the present study has limited graphical user interface and must be considered to have a high entry level compared to similar commercial software available. This represented a challenge in the start of this work as I was unfamiliar with this software.

I would like to give thanks to my supervisor professor Bjørnar Pettersen for his enthusiasm and motivation and to my co-supervisor PhD student Mia Prsic who has provided help and advices, specifically on the use of the different software and computer facilities.

Chengwang Lei kindly and rapidly answered my request and provided me with original data from the study of Lei et al. [1].

The use of the high performance computing facility Njord as a part of the Notur program is acknowledged.

Trondheim, June 2011

Knut Inge Engelbreth

Contents

Nomenclature

Latin letters

a, b, c	lengths characterizing the domain size
^{a}	calculations performed by Fast Fourier Transform (FFT)
$A_{m,0}$	coefficients in H
c	thermal conductivity
C_D	drag coefficient
$\overline{C_D}$	mean drag coefficient
C_L	lift coefficient
$\overline{C_L}$	mean lift coefficient
C'_L	fluctuating lift coefficient
$\sqrt{\overline{C'^2_L}}$	root-mean-square lift coefficient
d	averaged grain diameter
D	cylinder diameter
f_i	external body forces
f_v	vortex shedding frequency
F_D	drag force
F_L	lift force
g	acceleration due to gravity
G	gap
H	finite difference formulation of the convective and diffusive terms
h	enthalpy
k	kinetic energy
K, L, M , N, 0	number of elements
Ma	Mach number
n	normal direction
$n, n+1$	successive time steps
$\mathcal{O}$	order of magnitude
p	pressure
q_b	sediment transport
Δr	element length in the radial direction
Re	Reynolds number
s	specific gravity of sediments
Δs	element length along the cylinder surface
S	scour depth
S_i	finite difference formulation of source term
St	Strouhals number
t	time
Δt	length of time step
δt	length of time step in the finite difference formulation
T	period
T	temperature

u	horizontal velocity component
$u_{i,j}$	velocities in Cartesian tensor notation
U	velocity
U_0	free stream velocity
U_*	bed shear velocity
$x_{i,j}$	directions in space in Cartesian tensor notation
x	stream-wise direction
Δx	element length in the x-direction
y	stream normal direction in the 2D-plane
Δy	element length in the y-direction
z	stream normal direction normal to the 2D-plane
Δz	element length along the cylinder span (in the z-direction)

Greek letters

δ	boundary layer thickness
δ_{ij}	Kronecker delta
ϵ	dissipation
κ	steepness factor of a shear flow
ρ	density
ν	kinematic viscosity
μ	dynamic viscosity
τ	shear stress
θ	Shields parameter
ω_z	vorticity with reference to the z-axis
ϕ	flux
λ	bulk viscosity
Λ	aspect ratio of elements
$\triangle$	differential
$\triangle_i$	finite difference formulation of the differential operator
∇	operator
$^*,^{**},^{***}$	intermediate values in the calculations of successive time steps

Abbreviations

CFD	Computational Fluid Dynamics
FFT	Fast Fourier Transform
OpenFOAM	Open Source Field Operation and Manipulation
PISO	Pressure-Implicit with Splitting of Operators
RANS	Reynolds-Averaged Navier-Stokes
VIV	Vortex induced vibrations
2D	Two-dimensional
3D	Three-dimensional

1 Introduction

1.1 Background and motivation

Marine pipelines are widely used for the transport of hydrocarbons. Submarine pipelines placed at or near the seabed are exposed to currents and waves. In the presence of an erodible seabed, there may also be erosion of sediments beneath the pipeline. This process is termed *scour*.

Due to the installation procedure or due to the development of scour beneath the pipeline, free spans may occur in sections along the length of the pipeline. Scour and the development of free spans constitute a threat to the stability and structural integrity of the pipeline due to the loss of support in sections along the pipeline's span [2, p. 117].

Generally, the interaction between a cylindrical structure – such as a free spanning marine pipeline – and a steady transverse flow causes vortex shedding and oscillating pressure forces on the structure. These forces can excite vortex induced vibrations (VIV), which are recognized as important contributions to fatigue and reduced lifetime for the pipeline.

1.1.1 Offshore pipelines on the Norwegian continental shelf

There are approximately 20 000 kilometers of pipelines laid offshore in the North Sea for the purpose of petroleum transport, of which 5100 km are laid on the Norwegian shelf [3]. Gassco handles all transport of Norwegian gas for export and manages a network of about 7800 km of pipelines [4]. Most pipelines on the Norwegian shelf are rigid, only 240 km are flexible pipelines [3].

The dimensions of the pipelines may vary from 8-12 inches (20-30 cm) up to 44 inch (112 cm) for the largest gas export pipelines [4], [5, p. 15]

According to Jakobsen et. al [3], 1500 km of the pipelines on the Norwegian shelf are trenched, 2300 km are laid directly on the seabed and 1300 km are in unknown condition (i.e either buried, trenched or laid directly on the seabed). The total length of known buried pipelines in the North Sea is limited to only 110 km. The majority of rigid pipelines with dimensions smaller than 16 inches are trenched or buried.

In 2009, the Norwegian petroleum production totaled 115.45 million Sm^3 of oil and 103.47 million Sm^3 oil equivalents of gas [6, p. 325]. In addition there were smaller amounts of natural gas liquids (NGL) and condensate. 93% of the gas produced was exported for a total value of 186 859 million NOK [6, p. 266]. Hence, reliable operation and integrity of the pipelines are of great importance.

1.1.2 Characteristics of the flow around a circular cylinder in steady cross-flow

The flow around a circular cylinder in steady cross-flow is extensively studied and Zdravkovich [7] presents a thorough review of this work. The fundamentals of this flow configuration are outlined in the following:

The governing parameter for viscous flows is the Reynolds number, expressing the ratio of inertia to viscous forces. The Reynolds number is defined as:

$$Re = \frac{UD}{\nu} \tag{1.1}$$

Here U is the free-stream flow velocity, D is the diameter of the cylinder and ν is the kinematic viscosity. The flow around bluff bodies are characterized by the formation of a wake at the lee-side of the structure which depends on Re. Figure 1 (a)-(f) depicts the flow around a circular cylinder in uniform cross-flow for Re in the range 32-161. Generally, the wake is two-dimensional in this regime [8].

For circular cylinders at $Re > 47$ [10], the wake is characterized by the alternate shedding of eddies which are shed at frequency f_v. This frequency can be expressed by the non-dimensional Strouhals number St:

$$St = \frac{f_v D}{U} \tag{1.2}$$

Vortex shedding causes oscillating forces on the cylinder; lift oscillating at the frequency of eddy shedding f_v, and drag oscillating at twice this frequency [11, pp. 186]. Lift; F_L, is the force component in the stream-normal direction, while drag; F_D, is the force component in the stream-wise direction. These forces can be expressed non-dimensionally by the lift coefficient; C_L, and drag coefficient; C_D, respectively:

$$C_L = \frac{2F_L}{\rho U^2 D} \tag{1.3}$$

$$C_D = \frac{2F_D}{\rho U^2 D} \tag{1.4}$$

For further details on the mechanisms of vortex shedding, reference is given to [9].

Offshore pipelines and risers are often subject to $Re = \mathcal{O}(10^4 - 10^7)$. Generally, numerical simulations at these Reynolds numbers involves artificial turbulence modeling such as Large Eddy Simulations and the $k-\epsilon$-model in Reynolds-Averaged Navier Stokes equations. $Re = 100$ is chosen in the present study in order to avoid turbulence, but still get vortex shedding. The flow around a circular cylinder in uniform cross-flow at $Re = 100$ is extensively studied, both in experimental and numerical studies: A collocation of some results is given in table 1 where 'peak-peak' denotes the difference between the largest and smallest values of oscillatory quantities, 'Exp.' denotes results in experimental studies and 'Num.' denotes results in numerical studies. All values are exact results, except those by Norberg [10] which are obtained from empirical functions of Re based on a comprehensive review for Re in the range of 47-$2 \cdot 10^5$.

Table 1: Reference values for a circular cylinder in uniform cross-flow at Re=100

Study	Method	$\overline{C_D}$	$\sqrt{\overline{C_L'^2}}$	C_L peak-peak	St
Norberg [10]	Exp./num.		0.227		0.164
Tritton [12]	Exp.	1.26			0.157 - 0.164
Wieselberger from [13]	Exp.	1.43			
Hendersson [14]	Num.	1.35			
Williamson [15]	Exp.	1.33		0.70	0.160 - 0.164
Lei ($G/D = 3.0$) [1]	Num	1.46	0.244		0.177
Cao and Wan (3D) [16]	Num	1.39		0.67	0.168

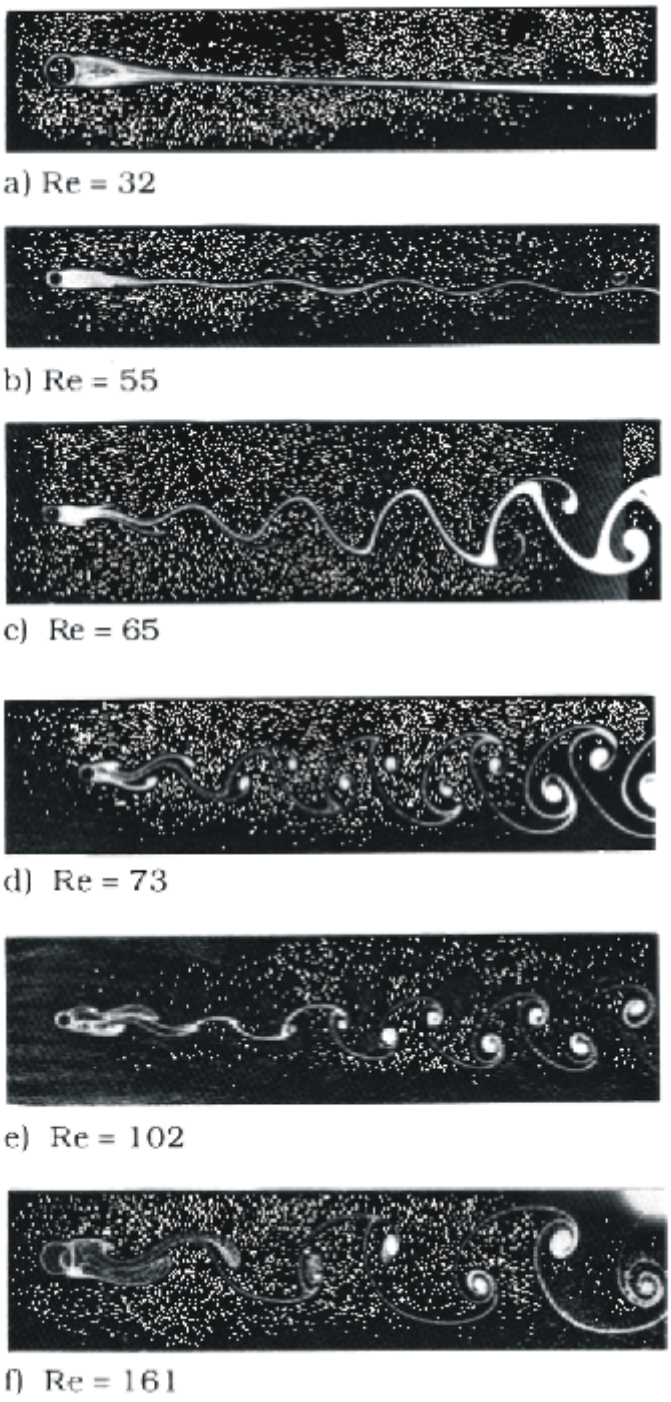

Figure 1: The flow around a circular cylinder in a range of *Re*. Reproduced from [9, p. 4, fig. 1.3]

1.1.3 Transition to turbulence for a circular cylinder in steady cross-flow

The transition to turbulence occurs in various regions around the cylinder dependent on the Reynolds number, illustrated in figure 2. In the figure, L denotes laminar flow, Tr denotes transitional flow, T denotes turbulent flow, BL denotes boundary layer and S denotes separation. The first transition occurs in the wake at $Re \simeq 190$, succeeded by transition in shear layer at $350 < Re < 400$ and then later by transition in boundary layer at $1{\cdot}10^5 < Re < 2{\cdot}10^5$ [7, p. 18].

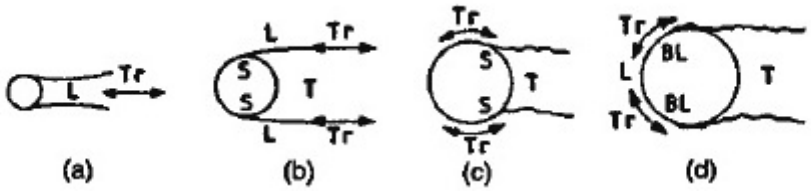

(a) Transition in the wake; (b) Transition in shear layer; (c), (d) Transition in boundary layer

Figure 2: Transition to turbulence in different regions dependent on Re. Reproduced from [7, p. 5, fig. 1.2]

In the following, wake transition is outlined based on the presentation by Williamson [8]: Transition to three-dimensional flow occurs at $Re \simeq 190$. However, contaminating end boundary conditions at the cylinder are known to trigger transition at lower Re. These contaminations may physically be interpreted as regions of vortex dislocations moving across the span. The wake transitional regime involves two modes of vortex shedding: mode A and mode B. These two modes are illustrated by a visualization from a numerical simulation at $Re = 265$ by Heggernes [17] in figure 3. Mode A is associated with lower shedding frequencies and a span-wise wavelength of $3.96D$-$4.01D$. Mode B is associated with higher shedding frequencies and span-wise wavelength $\sim 1D$.

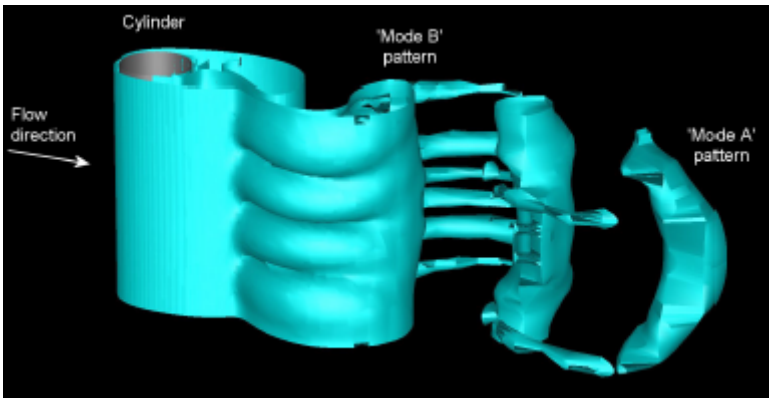

Figure 3: Visualization of mode A and B by an isosurface of the vorticity at $Re = 265$. Reproduced from [17, p. 38 fig 4.3]

At transition from two-dimensional to three-dimensional flow, mode A occurs first. As the Reynolds number increases, a gradual transfer to mode B occurs in the range $Re = 230$-260. At the upper end of this range, mode B dominates. In the gradual transfer between the two modes, mode A and B do not occur simultaneously, but the vortex shedding intermittently swaps between the two. For further reading on three-dimensional wake transition and the physical origin of mode A and B, reference is given to Williamson [8] and to the references herein.

Recently, Cao and Wan [16] demonstrated the application of the open source code OpenFOAM to simulate three-dimensional flows past a single circular cylinder and past two tandem circular cylinders at Reynolds numbers in the range 100-300. The lengths of the cylinders were $4.1D$ in these simulations.

1.1.4 Characteristics of the flow around a circular cylinder near a plane boundary

The flow around a pipeline and forces on it are affected by the proximity of the seabed. At first, the flow may be illustrated by considering the seabed as a plane and rigid wall. The flow around a circular cylinder in the proximity of a plane boundary is investigated by several researchers. This flow configuration is of academic interest and has several other practical applications for the purpose of engineering: wind past suspension bridges, flow around heat exchanger tubes near a wall and air-cooling of electronic components mounted at printed circuit boards [18].

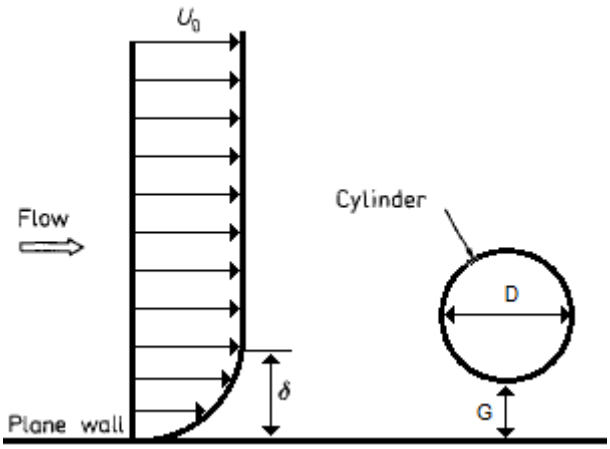

Figure 4: Sketch of the flow geometry for a cylinder near a plane wall

The cylinder and the wall is separated by a gap G and generally, a boundary layer forms at the wall. A sketch of the flow geometry is given in figure 4. According to the review by Zdravkovich [19, p. 872] the influence of the wall is primarily dependent on the following parameters in addition to the Reynolds number Re: gap-to-diameter ratio G/D, the relative boundary layer thickness δ/D and δ/G, and the flow characteristics of the boundary layer, i.e. whether the boundary layer is laminar, transitional or turbulent. Laminar and turbulent boundary layers are associated with small and large values of lift, respectively [19, p. 874].

Early experiments were performed by Taneda [20] with a towed cylinder at $Re = 170$ and different gap ratios G/D. Due to the towing of the cylinder, no boundary layer formed at the wall. At $G/D = 0.1$ one single row of vortices was observed and at $G/D = 0.6$ a double row of vortices was observed. To the knowledge of this author, this is the only published experimental study at such low Re.

Most of the published experimental and numerical work are done at Re in the order of 10^3-10^5 with the suppression of vortex shedding observed mainly in the range of G/D =0.2-0.4 [21, 22, 23, 24, 25] for boundary layer thickness δ/D approximately in the range 0.1-0.9. However, larger values of the critical gap for vortex shedding suppression are reported for thicker boundary layers [26, 22]. Grass et al. [22] suggest that this increase in critical gap could be due to the large velocity differential Δu across the cylinder,

advocating the importance of velocity gradient in the approaching flow. Taniguchi and Miyakoshi [26] note that the critical values of G/D for vortex shedding suppression corresponds to the point where the wall side of the cylinder comes in contact with the outer part of the turbulent boundary layer forming at the wall. There are also examples where the critical gap at which vortex shedding is suppressed decreases with the thickness of the boundary layer [23].

Generally, the drag decreases for decreasing gap ratio [1, 27]. At small gap ratios, a steady mean lift in the direction away from the wall is observed [21, 24], although dependent on the boundary layer some incidents of lift in the opposite direction are reported [24, 27].

At Re in the range 10^3-10^4, separation regions are observed both upstream and downstream of the cylinder at small gap ratios [21, 22, 28]. The upstream separation region is reported to form an obstacle to the approaching flow and its presence reduces the flow velocity through the gap and deflects upstream fluid over the top of the cylinder [22, 28]. The downstream separation region is reported to deflect the jet flow originating from the gap away from the wall to form a free jet [22].

Taniguchi and Miyakoshi [26] suggest the vortex street to form by concentration of vorticity by roll-up of separated shear layers originating from both sides of the cylinder; the free-stream side shear layer containing clockwise vorticity, while the wall side shear layer containing counterclockwise vorticity. The boundary layer formed at the wall is containing clockwise vorticity [26]. Grass et al. [22] suggest the free jet inhibits large-scale vortex roll-up in the wall side wake region. Further, cancellation of opposite signed vorticity in the wall boundary layer and the wall side shear layer is suggested as the cause of vortex shedding suppression [1, 26, 22].

At gaps smaller than the critical gap for vortex suppression, flow separation of the wall boundary layer is observed to coincide with the outward deflection of the wall side shear layer. Observations clearly indicate interaction between the wall side shear layer and the wall boundary layer: each (counterclockwise) vortex shed from the wall side of the cylinder is accompanied by a clockwise vortex in the near-wall region. As a result the wall boundary layer is destabilized and the flow detaches from the wall and ejects upwards. [25, 29]. Contrary to previous suggestions [1, 22, 26], Price [29] and Sarkar and Sarkar [18] find that the two shear layers do not cancel each other.

Lin et al. [28] presents a summary of previous experimental studies of a circular cylinder near a plane boundary and suggests the flow phenomena in the wake can be roughly classified into three regions due to the influence of the gap: (1) the characteristics of vortex shedding is similar to that of an isolated cylinder, (2) the plane boundary influence the vortex shedding and the periodic shedding from the upper shear layer is evident, (3) periodic vortex shedding is suppressed.

Lei et al. [1] performed 2D numerical simulations in the range Re = 80-1000 and report the strength of vorticity in the shear layers to decrease and the thickness of the shear layers to increase with decreasing Re. The consequence is suppression of vortex shedding at larger gap ratios for lower Re. For high Re, the critical value approaches $G/D \simeq 0.2$. This study by Lei et al. is one of the few published numerical studies of the flow around a circular cylinder near a plane boundary performed at $Re = 100$.

1.1.5 Basic features of a circular cylinder exposed to a linear shear flow

For vortex shedding from a cylinder near a wall, Grass et al [22] suggested the importance of the velocity differential Δu over the cylinder in the approaching flow. Hence, the

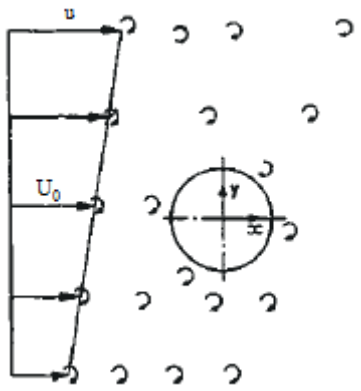

Figure 5: Shear flow. Reproduced from [7, p. 460 fig. 15.1] and modified.

influence of shear in the approaching flow is of interest. Zdravkovich [7, pp. 454] describes the influence of introducing a linear shear in the inflow for a cylinder in infinite fluid. The inflow velocity profile u is then expressed in terms of:

$$u = U_0 \left(1 + \kappa \frac{y}{D}\right) \tag{1.5}$$

where U_0 is the free stream velocity at $y = 0$ (the cylinder's axis of symmetry) and κ is the steepness factor:

$$\kappa = \frac{D}{U_0} \frac{du}{dy} \tag{1.6}$$

According to Zdravkovich [7, p. 465], the steepness factor κ replaces the Reynolds number Re as the governing parameter for the flow around a cylinder subject to a linear shear flow. At $Re = 100$, steep shear flows prevent vortex shedding, and incipient eddy shedding takes place for $\kappa < 0.14$ [7, p. 467].

1.1.6 Mechanisms of scour under a marine pipeline

This section outlines the physical description of sediment transport and scour due to a steady current based on the presentation given by Sumer and Fredsøe [5] and Nielsen [30]. Attention is given to the onset and development of scour and the influence of key parameters on scour. Scour due to oscillating currents and waves are omitted.

Most of the natural oceanic seabed is not totally rigid or impermeable, but rather consists of sediments with a finite size and mass. These sediments are influenced by the bounding water motions, and specifically the bed shear stress τ. The sediment transport, q_b, is governed by the bed shear stress [31] by the relation $q_b \sim \tau^{3/2}$ [5, p. 32]. The bed shear stress in the case of an undisturbed flow (i.e. no structure present) is denoted τ_∞.

The presence of a structure (e.g. a pipeline) at, or close to, the seabed will generally cause a local change in the flow and an appurtenant increase in the bed shear stress which in turn leads to erosion of sediments. Excessive scour represents a threat to the stability and structural integrity of the pipeline [2, p. 117].

For *non-cohesive granular* soil, the limit for sediment transport to occur is determined by the Shields parameter θ, defined as [5, p. 10]:

$$\theta = \frac{U_*^2}{g(s-1)d} \tag{1.7}$$

where $U_* = \sqrt{\tau/\rho}$ is the bed shear velocity, ρ is the fluid density, g is acceleration due to gravity, s is specific gravity of sediment grains and d is the grain size. θ must be above a critical value θ_{cr} in order for sediment transport to occur. θ_{cr} is dependent on the parameter dU_{*0}/ν which may be termed the grain Reynolds number in which U_{*0} is the undisturbed bed shear velocity with $\tau = \tau_\infty$. Data presented by Sumer and Fredsøe [5, p. 10] indicates the critical value of the Shields parameter is approximately constant $\theta_{cr} \approx 0.05$ for $dU_*/\nu > 500$.

The scour process is divided into two categories based on the Shields parameter: *Clear-water scour* is the condition where no sediment transport takes place in the undisturbed flow far from the structure ($\theta < \theta_{cr}$). *Live-bed scour* is the opposite condition where sediment transport takes place over the entire bed ($\theta > \theta_{cr}$).

Some values for mean grain size d for different types of seabed are given in table 2. Specific gravity for rock types such as granite, gneiss and quartzite are in the range 2.6 - 3.0 [32].

The development of scour can usually be divided into four stages: onset of scour, tunnel erosion, lee-wake erosion and the final equilibrium stage. It must be underlined that scour behaves in a three-dimensional fashion and that scour takes place locally along the pipeline and then propagates along the length of the pipeline in both directions. Scour holes will then form at sections along the pipeline and between these sections are the span shoulders where the weight of the pipe is supported. A two-dimensional description of scour is outlined in the following.

Onset of scour is the first stage in the scour process. A pipeline placed on a seabed in a transverse current experiences a pressure difference between the upstream side and the downstream side. This pressure difference gives rise to a seepage flow in the sediment bed under the pipeline. At a sufficiently large current velocity, sand and water will eventually break through beneath the pipeline [5, p. 17]. Increased burial of the pipe is understood to increase the resistance against the onset of scour.

Tunnel erosion succeeds the onset of scour. In this stage there is a small gap between the pipe and the seabed, depicted in figure 6. As a result very large flow velocities occur in the gap, and this is accompanied by very large bed shear stresses just below the pipeline [5, p. 31]. Violent scour is hence expected under the pipeline immediately after the onset of scour. Scour propagation along the pipeline is most dominant at this stage [34]. Attributed to the gap flow is also a strong suction below and behind the pipeline resulting in a negative lift force and relatively high drag [9, p. 65]. The lift is then negative throughout the remaining scour process.

Table 2: Mean grain size for different types of seabed. From [33, p. 10]

Seabed	d [mm]
Silt and clay	0.0625
Fine sand	0.25
Medium sand	0.5
Coarse sand	1.0
Gravel	4.0
Pebble	25
Cobble	125
Boulder	500

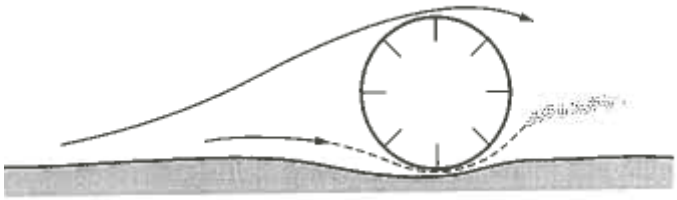

Figure 6: Tunnel erosion. Reproduced from [5, p. 31 fig 2.11]

Lee-wake erosion follows the tunnel erosion. Due to the rapid tunnel erosion a dune forms downstream of the pipeline. As time elapse and scour develops, the dune gradually moves downstream and may eventually disappear as the equilibrium scour profile is attained, as depicted in figure 7. Numbers at scour profiles in the figure denote time [min]. As the gap between the pipe and the seabed increases, vortex shedding starts to occur in the flow behind the pipeline. Vortices are alternately shed from the free stream side and the bed side of the pipe. The latter vortices sweep the bed, as they are convected downstream. Indications are that these vortices substantially increase the sediment transport and contributes to lee-side erosion [5, p. 34].

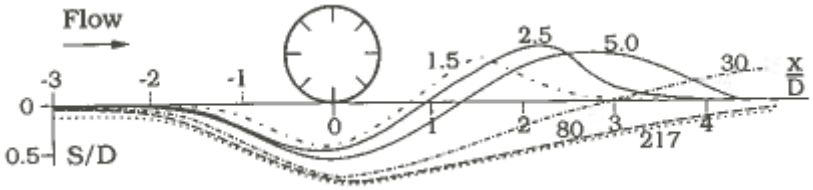

Figure 7: Development of scour. Reproduced from [5, p.33 fig 2.13]

The equilibrium stage is eventually attained when the scour process comes to an end. This occurs when the bed shear stress at the bed below the pipeline is constant and equal to the bed shear stress in the undisturbed flow, i.e. $\tau = \tau_\infty$ The equilibrium scour depth is denoted S, usually expressed non-dimensional by the ratio S/D, and dependent on the Shields parameter θ. The scour depth is zero for very small values of θ and increases as θ approaches θ_{cr}. Very small variations are observed in the scour depth as θ increases above the critical value θ_{cr}. This led Sumer and Fredsøe [5, p. 41] to suggest a mean value of $S/D = 0.6$ with standard deviation of 0.2 for this scour depth.

Sumer and Fredsøe [9] summarizes the results in an experimental study by Jensen et al. [35] at $Re = 10^3$, where a cylinder is located at five different stages of the scour process and the forces on the cylinder are measured: For the cylinder located above an equilibrium scour profile, a negative mean lift is observed. Additionally, the results in the study of Jensen et al. [35] are compared to those of the flow around a circular cylinder near a plane wall. At a similar gap below the cylinder, $\overline{C_L}$ is negative in the scour case and positive in the case of a plane wall. Similarly, $\overline{C_D}$ is slightly reduced in the scour case. The front stagnation point is moved towards the free-stream side and this is suggested as the cause of the negative lift.

1.1.7 Mathematical modeling of scour under marine pipelines

This section outlines methods for mathematical modeling of scour, which are considered in order to gain further knowledge of the phenomena and to predict the development of

local scour and the resulting forces on the pipeline. According to a review by Sumer [36], there are three categories of mathematical scour models: (1) Potential-flow models, (2) Numerical models which basically are solving Navier-Stokes equations (3) Integrated models predicting the entire scour process along the pipeline in terms of time series. It should be noted that potential-flow models are by virtue not capable of handling lee-wake erosion [36].

Only a limited number of numerical investigations address the complete Navier-Stokes equation for the purpose of scour modeling [36]. Brørs [37] applies Reynolds-Averaged Navier-Stokes equations with a $k-\epsilon$ model and a sediment transport model to predict flow and scour below a bed mounted circular cylinder. The flow and scour should ideally be calculated simultaneously. However, this is too computationally expensive [38]. Additionally, the time scales of scour and the flow field are quite different; the flow field changes much faster than the bed change due to scour [38]. The general approach in the method of Brørs is (1) run the flow simulation a number of time steps (in the order of hundred), (2) compute the bed change and (3) evaluate the new bed profile and adapt the grid. Liang et al. [38] apply a similar, yet more refined, method which includes sand slide on steep slopes. Additionally they investigate several turbulence models for scour application.

Recently, Yeganeh-Bakhtiary et al [39] suggested a two-phase model to investigate tunnel erosion beneath a pipeline. The two phases involved are the fluid phase and the sediment phase which both are simulated by two-dimensional Reynolds-Averaged Navier-Stokes equations with a $k-\epsilon$ turbulence model.

1.2 Scope of work in the present study

On the basis of the preceding section, it is of interest to study the viscous flow around a circular cylinder in the proximity of a fixed boundary. The purpose of this study is to apply the software OpenFOAM for numerical simulations of the viscous flow around a circular cylinder near a plane wall at $Re = 100$. The aim is to investigate and to further illuminate the associated flow phenomena. Three different gap ratios: $G/D = 0.2; 0.5; 1.0$ are applied. These gap ratios are expected to represent three distinct different gap regimes: Suppression of vortex shedding is expected at the smallest gap; $G/D = 0.2$. At this gap ratio the cylinder is quite close to the wall, yet the choice of this gap simplifies the grid design compared to the case where the cylinder touches the wall ($G/D = 0$). Vortex shedding is expected at $G/D = 1.0$, and an additional intermediate gap $G/D = 0.5$ is investigated.

Further, the geometry of the wall is altered to imitate the shape of a fully developed scour profile. However, no attempts are made to perform calculations of scour or sediment transport. These simulations are expected to add new results to this topic of research.

The low Reynolds number in the present study provides the possibility of accurate calculations avoiding the use of artificial modeling of the flow such as turbulence modeling which is necessary at higher Reynolds number in Reynolds-Averaged Navier Stokes (RANS) equations and Large Eddy Simulations (LES).

The investigations of the flow address the main physical properties: pressure, velocity and vorticity by different means of visualization. The flow characteristics are quantified in terms of lift, drag and frequency of vortex shedding, all being expressed non-dimensionally by the lift and drag coefficient and Strouhals number, respectively. These quantities are related to the gap ratio in terms of G/D and G/δ. The results are compared to reported

values in the literature.

In an attempt to validate the results and the applied computational method, the flow around an unconfined circular cylinder in uniform cross-flow is considered a benchmark. This flow configuration is extensively studied in the present study and the results are compared to relevant results in the literature.

The numerical parameters of most importance in the present study are considered to be the domain size, grid geometry, element size, element spacing and time step. The influences of these parameters are investigated both for the cylinder in uniform cross-flow and for the cylinder near a plane wall, except the time step which is only investigated for the cylinder in uniform cross-flow.

Two-dimensional simulations are performed for all of the above mentioned flow configurations. A few three-dimensional simulations are performed for an unconfined cylinder in uniform cross-flow and a cylinder located at $G/D = 0.5$ from a plane wall.

1.3 Outline of the present thesis

Chapter 1 gives an introduction advocating the relevance of this flow and presents some of the basic features of the flow around a circular cylinder in uniform cross-flow, cylinder near a plane wall and scour under marine pipelines.

Chapter 2 presents the governing equations for the fluid flow problem.

Chapter 3 gives an overview of the computational work; emphasizing the structure of OpenFOAM and its utilities: the icoFoam-solver and the applied numerics.

Chapter 4 presents the numerical simulation of flow around a circular cylinder in uniform cross-flow; starting with a description of the setup and the main results, followed by a thorough investigation of numerical parameters. The chapter concludes with a discussion of the results.

Chapter 5 presents the simulations of flow around a circular cylinder located at different gaps to a plane wall; starting with a description of the setup, main results and an investigation of numerical parameters, followed by visualizations of pressure, velocity and vorticity at different gaps and a discussion of the flow phenomena for these flows. The chapter concludes with a discussion of the results and a comparison to results in the literature.

Chapter 6 presents the simulations of flow around a cylinder located above a fixed scour profile; starting with a description of the setup and the main results, followed by a discussion of the results and flow phenomena and visualizations of pressure, velocities and vorticity.

Chapter 7 concludes the present thesis, summarizing the main results and presenting recommendations for further work.

2 Governing equations

This section is based on the presentation given by White [40, pp. 59-73] and Issa [41]. The fluid flow is governed by the laws of conservation which applies to a physical system: (1) The conservation of mass, (2) the conservation of momentum and (3) the conservation of energy. The fluid itself is assumed to be of homogeneous composition. In the following, the laws of conservation are adapted for the use in fluid motion. Cartesian tensor notation is applied in the equations.

The conservation of mass may be expressed in terms of the equation of continuity in its general form:

$$\frac{\partial \rho}{\partial t} + \frac{\partial \left(\rho u_i\right)}{\partial x_i} = 0 \tag{2.1}$$

where i, j =1, 2, 3. x_1 and x_2 denotes the stream-wise and stream normal directions in the 2D plane. x_3 denotes the stream normal direction into the third dimension of space, making the domain three dimensional (3D). u_1, u_2 and u_3 are the corresponding velocity components, t is time and ρ is the density of the fluid.

The conservation of momentum may be expressed by the Navier-Stokes equation in its general form:

$$\rho\left[\frac{\partial u_i}{\partial t} + u_j\frac{\partial u_i}{\partial x_j}\right] = -\frac{\partial p}{\partial x_i} + \frac{\partial}{\partial x_j}\left[\mu\left(\frac{\partial u_i}{\partial x_j} + \frac{\partial u_j}{\partial u_i}\right) + \delta_{ij}\lambda\frac{\partial u_i}{\partial x_i}\right] + f_i \tag{2.2}$$

where p is the pressure, ν is the dynamic viscosity of the fluid. δ_{ij} is the Kronecker delta function: $\delta_{ij} = 1$ if $i = j$ and $\delta_{ij} = 0$ if $i \neq j$. λ is the coefficient of bulk viscosity and is related to volume expansion only. f_i represents external body forces, e.g. gravitational and electromagnetic fields.

The speed of sound in water is approximately $a = 1490$ m/s [42, p. 608] and the free-stream velocity is unity. Hence, the Mach number in the present study is of the order 10^{-3}:

$$\mathrm{Ma} = \frac{u}{a} \tag{2.3}$$

The fluid is assumed to be incompressible, which is a valid assumption as the Mach number, Ma, is well below the limit $\mathrm{Ma} < 0.3$. External body forces such as gravity are neglected. Further, constant viscosity is assumed. The equations (2.1) and (2.2) then simplify to (2.4) and (2.5), respectively.

$$\frac{\partial u_i}{\partial x_i} = 0 \tag{2.4}$$

$$\frac{\partial u_i}{\partial t} + u_j\frac{\partial u_i}{\partial x_j} = -\frac{1}{\rho}\frac{\partial p}{\partial x_i} + \nu\frac{\partial}{\partial x_j}\left(\frac{\partial u_i}{\partial x_j} + \frac{\partial u_j}{\partial u_i}\right) \tag{2.5}$$

The law of conservation of energy may be expressed by the equation of energy:

$$\rho\frac{Dh}{Dt} = \frac{Dp}{Dt} + \frac{\partial}{\partial x_j}\left(c\frac{\partial T}{\partial x_j}\right) + \mu\left(\frac{\partial u_i}{\partial x_j} + \frac{\partial u_j}{\partial u_i}\right)\frac{\partial u_i}{\partial x_j} \tag{2.6}$$

where h is the enthalpy, c is the thermal conductivity and T is the temperature.

With the preceding assumptions of constant density and viscosity, the equations for continuity (2.4) and momentum (2.5) are entirely uncoupled from temperature and may

be solved to obtain velocities and pressure for a given flow problem. Temperature may then subsequently be solved from the energy equation (2.6). However, temperature and heat transfer are omitted in the present study and the energy equation (2.6) is thus superfluous.mited in the present study and the energy equation (2.6) is thus superfluous.

The equations for continuity (2.4) and momentum (2.5) are non-linear and coupled due to the presence of u_i and p. As a matter of fact, there exists no general analytical solution to this system of equations [40, p. 96]. Hence, numerical methods should be pursued in order to solve the equations.

3 Computational work

The present study utilizes the software Open Source Field Operation and Manipulation (OpenFOAM) which is an open source code software for computational fluid dynamics (CFD). The software is released by OpenCFD Ltd. and is available for free download from the Internet address www.openfoam.com for Linux operating systems.

OpenFOAM can be executed at a regular laptop in a Linux-operating environment, and it also supports parallelization: allowing the simulations to run on multiple processors in parallel. In the present study, simulations are performed in parallel at the high performance computer cluster Njord as part of the NOTUR program.

3.1 The structure of an OpenFOAM case

OpenFOAM is constituted by a set of C++ modules and has limited graphical user interface: The built-in utility `paraFoam` provides possibilities of visualizing the grid and the obtained results. Anyhow, it is advantageous for the user to have some knowledge of C++ programming in order to utilize this software efficiently. The software is open source, and hence the user has full access to the source code of any solver, utility and library. OpenFOAM also provides the user with numerous possibilities and accompanying demands to make choices. The file structure of an OpenFOAM case is shown figure 8 and outlined in the following based on the description in the OpenFOAM User Guide [43, sec. 4.1].

The case directory contains three main directories named *constant*, *system* and '*time*'. The full name of any '*time*' directory is constituted by the actual time for that directory, e.g. for the initial time $t = 0$, the time directory is named *0*. The time directories contain field data such as pressure and velocity. The data can either be initial values and boundary conditions prescribed by the user, or results from OpenFOAM written to file.

The *constant* directory contains files which specify the physical properties involved. In the present study the directory contains one such file named `transportProperties` which contains the value of $\nu = 1{\cdot}10^{-2}$ m^2/s. As both the structural dimension and the undisturbed flow velocity have the dimension of unity, the value of ν determines the Reynolds number: $Re = 100$. The *constant* directory contains a second directory, *polymesh*, which contains all the information about the mesh for the specific case.

The *system* directory contains files associated with the solution procedure: `controlDict`, `fvSchemes`, `fvSolution` and `decomposeParDict`. The parameters in the file `controlDict` determines run control such as start/end time and time step. In addition there is the possibility to set parameters for data output. In the present study the `controlDict` is modified to include calculation of forces and force coefficients at each time step in addition to sampling of instantaneous values of pressure and velocity at a given point in the fluid domain. An example of a typical OpenFOAM `controlDict` is given in Appendix A. `fvSchemes` determines the discretization schemes used in the solution, while `fvSolution` determines the solvers and parameters for algorithm control. `decomposeParDict` determines the parameters for decomposing the mesh into separate domains in order to run the case in parallel on multiple processors.

3.2 Pre-processing

Prior to the execution of the numerical simulation itself, pre-processing is performed. This includes the definition of the fluid domain and the subsequent division of the fluid domain

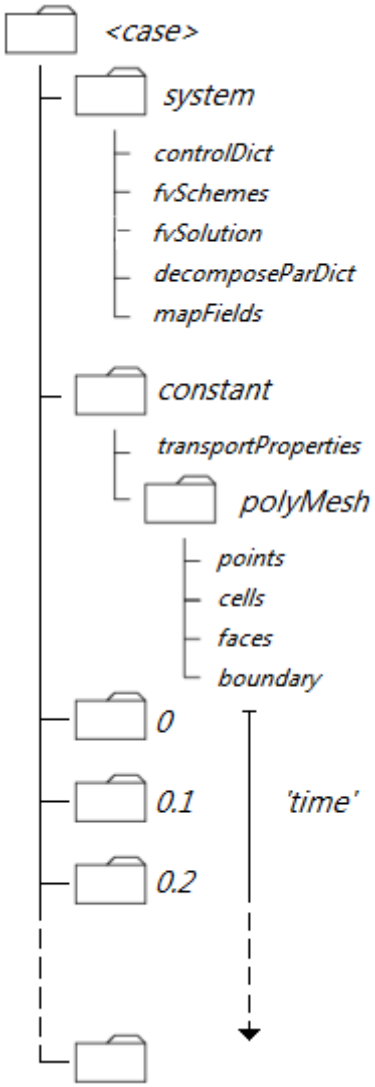

Figure 8: The file structure of an OpenFOAM case. Reproduced from [43, fig. 4.1, sec. 4.1] and modified.

into a grid of discrete three-dimensional (3D) elements of finite volume. In the present study the computational grid is created by the use of NTNU/SINTEF in-house software Mega. The mesh is created in the file format .msh and then converted to OpenFOAM format by the OpenFOAM utility `gmshToFoam`. Further, the pre-processing involves the specification of relevant fluid properties and the appropriate boundary conditions.

3.3 icoFoam - an OpenFOAM solver

OpenFOAM uses a finite volume method for space discretization [44]. Other numerical methods of space discretization are the finite difference method and the finite element method. In the following, a brief outline of the finite volume method is given based on the presentation by Versteeg and Malalasekera [45, pp. 2-5]. In the finite volume method, the governing equations are integrated over all the finite volumes of every element of the computational domain. This ensures the fulfillment of the physical laws of conservation of the fluid properties for each element with reference to section 2. Further, the integrated equations are converted to a system of algebraic equations. This is done by substituting

the terms in the integrated equations by formulations similar to finite difference formulations. These equations may then be solved by means of iterative methods.

OpenFOAM has a wide range of standard solvers designed for specific applications in different categories of continuum mechanics. For the present study, the solver `icoFoam` is expected to be appropriate as it is a transient solver for laminar flow of an incompressible Newtonian fluid [43, sec. 3.5].

The Pressure-Implicit with Splitting of Operators (PISO) algorithm by Issa [41] is one of the methods available to resolve the pressure-velocity coupling of the governing equations. Issa originally presented a finite difference formulation of the PISO algorithm, while `icoFoam` applies a finite volume formulation of the PISO algorithm. Finite volume formulations of the PISO algorithm are outlined by Jasak [46] and Rusche [47]. In the following, the finite difference formulation of Issa [41] is presented alongside the finite volume formulation in the OpenFOAM source code of `icofoam.c` [48]. For details on the finite difference formulation, reference is given to [41].

n and $n+1$ denote successive time steps. The governing equations for continuity (2.4) and momentum (2.5) may then be expressed in finite difference form for each mesh point [41]:

$$\Delta_i u_i^{n+1} = 0 \tag{3.1}$$

$$\frac{\rho}{\delta t}\left(u_i^{n+1} - u_i^n\right) = H(u_i^{n+1}) - \Delta_i p^{n+1} + S_i \tag{3.2}$$

where Δ_i is the finite difference representation of $\partial/\partial x_i$, δt is the length of the time step, the operator H is the finite difference representation of the convective and diffusive terms. In general, H takes the form $H(u_i) = A_m u_{i,m}$ where m identifies the grid nodes and A is a coefficient. S_i is a source term which was omitted in equation (2.5) although present in equation (2.2).

An equation for pressure may be derived from equations (3.1) and (3.2) [41]:

$$\Delta_i^2 p^{n+1} = \Delta_i H(u_i^{n+1}) + \Delta_i S_i + \frac{\rho}{\delta t}\Delta_i u_i^n \tag{3.3}$$

In the continuation, the latter equation replaces equation. (3.1). The PISO algorithm consists of several steps where equations (3.2) and (3.3) are used to determine velocity and pressure fields, respectively. Then *, ** and *** denote intermediate values during the calculation from time step n to $n+1$.

The main steps of the PISO algorithm are as follows:
(1) The predictor step:
- Make an initial guess of the pressure p^n
  (In the present study, use the value from the previous time step)
- Use the initial value of pressure p^n to solve the discretized momentum equation for a new velocity u_i^*.

(2) The corrector steps
- Use the new velocity u_i^* to solve the pressure equation for p^*.
- Use the new pressure p^* and velocity u_i^* to solve the momentum equation for a new velocity u_i^{**}

The corrector steps are repeated, taking the last calculated velocity and pressure as input.

3.3.1 The predictor step

The pressure field p^n obtained at the previous time step $t = n$ is used in the solution of the implicit momentum equation (3.2) which are solved for an intermediate velocity field u_i^*:

$$\frac{\rho}{\delta t}\left(u_i^* - u_i^n\right) = H(u_i^*) - \Delta_i p^n + S_i \tag{3.4}$$

In `icoFoam.c`, the equivalent finite volume representation is:

```
fvVectorMatrix UEqn
(

      fvm::ddt(U)
    + fvm::div(phi, U)
    - fvm::laplacian(nu, U)

);
solve(UEqn == -fvc::grad(p));
```

where the finite volume representations are as follows, `ddt` denotes $\partial/\partial t$, `div()` denotes $\nabla\cdot()$, `laplacian()` denotes $\nabla^2()$, `U` denotes u_i, `nu` denotes ν, `phi` refers to the flux $\phi = \rho u_i$ [43, sec. 4.4.5]. `fvm` and `fvc` indicate that the term is to be solved by the finite volume method (i.e implicitly) or by finite volume calculation (i.e explicitly), respectively.

3.3.2 The corrector steps

The predictor step is followed by a set of corrector steps in a so-called PISO-loop. The first corrector step starts with a modification of the equations for momentum (3.2) and pressure (3.3). The diagonal elements of H are extracted from H and moved to the left hand side of the corrector step equations. The remaining part of H is preserved on the right hand side. Thus, the diagonal elements on the left hand side are treated implicitly, while the remaining elements on the right hand side are treated explicitly. This is done to ensure a more stable, yet accurate solution [41]. The diagonal elements of H may be expressed as $A_0 u_i$, giving rise to a definition of $H'(u_i)$ [41]:

$$H'(u_i) = H(u_i) - A_0 u_i \tag{3.5}$$

A new pressure equation may then be derived for the first corrector step [41]:

$$\Delta_i \left[\left(\frac{\rho}{\delta t} - A_0\right)^{-1} \Delta_i\right]\left(p^* - p^n\right) = \Delta_i u_i^* \tag{3.6}$$

Using the solution for u_i^* obtained in the predictor step, the pressure equation (3.6) may be solved for the pressure field $(p^* - p^n)$. Correspondingly, a new momentum equation may be derived [41]:

$$\left(\frac{\rho}{\delta t} - A_0\right)\left(u_i^{**} - u_i^*\right) = -\Delta_i\left(p^* - p^n\right) \tag{3.7}$$

which may be solved for u_i^{**} once $(p^* - p^n)$ is known.

In `icoFoam.c`, the corrector step starts with the modification of H and the momentum equation, followed by calculation of `phi` from the obtained values of `U` from the predictor

step:

```
volScalarField rUA = 1.0/UEqn.A();
U = rUA*UEqn.H();

phi  = (fvc::interpolate(U) & mesh.Sf())
     + fvc::ddtPhiCorr(rUA, U, phi);

adjustPhi(phi, U, p);
```

Then, in `icoFoam.c`, the pressure equation is defined and solved. The new pressure field is subsequently used to obtain new corrected velocities by the momentum equation:

```
fvScalarMatrix pEqn
(

    fvm::laplacian(rUA, p) == fvc::div(phi)

);

pEqn.setReference(pRefCell, pRefValue);
pEqn.solve();

U -= rUA*fvc::grad(p);
U.correctBoundaryConditions();
```

The corrector step may then be repeated, replacing the velocities and pressures of the intermediate steps by its subsequent steps in equations (3.6) and (3.7): Thus replace u_i^* by u_i^{**}, u_i^{**} by u_i^{***}, p_i^n by p_i^* and p_i^* by p_i^{**}. The corrector step should at least be performed twice, but typically not more than four times according to the OpenFOAM User Guide [43, sec. 4.5.3]. Two corrector steps provide sufficient accuracy for most practical applications according to Issa [41]. On this basis 2 corrector steps are applied in the present study. This is determined by the value of the PISO-parameter `nCorrectors` in the file `fvSolution` in the *system* directory of the relevant case.

3.3.3 Solving the equations for velocity (U) and pressure (p)

The following is based on the OpenFOAM User Guide [43, sec. 4.5]. The equations for `p` and `U` are linear, and their solvers are prescribed in the file `fvSolution` in the *system* directory. The default settings are chosen for these solvers in the present study. The solver for `p` is preconditioned conjugate gradient (PCG) with a Diagonal incomplete-Cholesky (DIC) preconditioner. This set of solver and preconditioner is applicable to symmetric matrices. The purpose of the preconditioner is to increase the rate of convergence of the preconditioned system compared to the original system. The solver for `U` are a Preconditioned conjugate gradient (PBiCG) with a Diagonal incomplete-LU (DILU) preconditioner. This is the asymmetric equivalent of PCG and DIC.

The solvers for the `p` and `U` equations are iterative and based on reducing the residual. The initial residual is obtained from the current value of the field. The residual is then evaluated after each iteration. The solver stops the iteration process if the residual falls below the prescribed solver tolerance. The solver tolerance of `p` and `U` are 10^{-6} and 10^{-5},

Table 3: Numerical schemes applied in OpenFOAM in the present study

Terms and operators	Numerical scheme
Interpolation	Linear
Gradient	Gauss linear
Surface normal gradient	corrected
Time derivative	Euler
Divergence	Gauss linear
Laplacian	Gauss linear corrected

respectively. OpenFOAM also provides the possibility of prescribing a relative solver tolerance between the initial residual and the final residual. In order to force the solution to converge to the solver tolerance, the relative tolerance is set to 0.

3.3.4 Numerical schemes

OpenFOAM offers a wide range of numerical treatment of different terms in the equations. This section presents the numerics applied in the present study and is based on the description given in the OpenFOAM User Guide [43, sec. 4.4]. A summary of the applied numerical schemes is given in table 3. The numerical schemes are prescribed in the file `fvSchemes` in the *system* folder. For details on the different schemes available, reference is given to the OpenFOAM User Guide [48, sec. 4.4].

Values are typically interpolated from cell centers to face centers and a `linear` interpolation scheme is applied in the present study. A standard second order finite volume discretization of Gaussian integration scheme, `Gauss linear`, is applied for the gradient terms, e.g. `grad(p)`. This scheme requires interpolation of values from cell centers to cell faces, hence an interpolation scheme must be specified. In this case a `linear` interpolation scheme is applied. Surface normal gradients are evaluated at cell faces. A cell face connects two cells and now the gradient is taken of the values at centers of these two cells. The surface normal gradient is then the gradient component which is normal to the cell face. In the present study an explicit non-orthogonal correction scheme is specified by the keyword `corrected`. The implicit, first order `Euler` scheme is applied for the time derivative `ddt`. The `Gauss` scheme is the only available option for the divergence term, `div(phi, U)`. Again, this requires the specification of an interpolation scheme being `linear` in the present study. The `Gauss` scheme is the only available option for the laplacian term, `laplacian(nu, U)` This requires the specification of an interpolation scheme for `nu` and a surface normal gradient scheme. The applied schemes in the present study are `linear` and `corrected`, respectively.

3.4 Boundary conditions and initial values

In this section is outlined the general boundary conditions relevant for this study. The assigned boundary conditions are presented alongside a definition sketch for each case in the succeeding sections. This section is based on the OpenFOAM User Guide [43, sec. 5.2]. The boundary conditions and initial values must be set in the `p` and `U` files in the first time directory (e.g. *0*) of the case. OpenFOAM provides a range of different built-in boundary conditions. As OpenFOAM is an open source software, the user has the opportunity to create other boundary conditions such a parabolic velocity profile at the inlet (imitating

a developed boundary layer). In this study no effort is made to investigate different boundary conditions and only simple boundary conditions are applied. The boundary conditions can then be divided into the following main types: `patch, empty, cyclic, symmetryPlane` and `wall`.

The type `patch` provides the possibility to declare a constant value, `fixedValue`, of the field variable (`p, U`) or a normal gradient `fixedGradient` (or `zeroGradient`) of the field. Another option is `calculated` which enables `p` to be determined from `U` or vice versa.

Due to the three-dimensionality of the OpenFOAM discretization, the type `empty` is assigned to the front and back faces of the mesh to enforce two-dimensional simulation. The type `cyclic` is suitable for 3D simulations: If it is applied to the front and back faces, it enables these faces to be treated as if they were physically connected. In this manner the geometry is repeated along the span. However, by the use of the pre-processing software in this study, it is a little complicated to apply this boundary condition on any mesh geometry being more than trivial.

The type `symmetryPlane` introduces a symmetry plane and is less intervening than a fixed value when applied to the stream-normal boundaries. The symmetry planes should be separated some distance to avoid artificial influence on the solution. `symmetryPlane` is assigned to the front and back faces in the three-dimensional simulations in the present study.

The type `wall` is particularly relevant for turbulent flows where the wall boundary is treated with special wall modeling (wall functions). In the present study, the desired wall boundary conditions can be obtained with the specification of a patch; `zeroGradient` for pressure and `fixedValue` of zero velocity.

In the present study, some common boundary conditions are applied in all cases: The inlet condition is a uniform velocity at the inlet and a zero normal pressure gradient. The cylinder is considered a rigid and impermeable wall and hence the no-slip velocity and a zero normal pressure gradient are appropriate. Along the downstream outlet a zero normal velocity gradient and an absolute pressure of zero are prescribed. The pressure condition will influence the solution a certain distance upstream, wiping out pressure differences in the stream-normal direction and influencing the wake if the outlet is located too close to the cylinder. A proper location of this boundary is ensured by investigation of domain size.

For a cylinder in infinite fluid the boundary conditions applied to the lateral sides are symmetry planes. Hence, these boundaries should be located sufficiently distant from the cylinder. This is ensured by the investigation of domain size.

The PISO algorithm also requires initial values for the internal fields of `p` and `U`. In the first simulations these values are set to 0 and the simulations are successful at first. Later, numerical errors and difficulties are encountered. A solution to this is to change the initial value of the internal fields to quite a small number different from zero: $1 \cdot 10^{-12}$. These numerical errors related to the internal field are presumed to be due to either three-dimensional simulations or to the parallel computing on decomposed cases in general.

3.5 Post-processing and data analysis

Post-processing is the step of visualizing and interpreting the results obtained in the simulation. The OpenFOAM utility `paraFoam` is used for post-processing. This utility

uses the open source visualization application ParaView [43, sec. 6.1]. Paraview provides numerous visualization possibilities. For further details, reference is given to [43, sec. 6.1].

After the simulations, vorticity fields may be calculated by the utility `vorticity` and velocity gradients at walls may be calculated by the utility `wallGradU`. Values of mean and root-mean-square of drag and lift coefficients are obtained by simple time series analyses in Microsoft Excel.

The lift acting on the cylinder oscillates at the frequency of vortex shedding. Thus, the vortex shedding frequency may be obtained from time series of the lift coefficient. However, lift is a quantity obtained by integration over the surface of the cylinder. A more direct indication of vortex shedding is the oscillatory pressure in the near wake close to the cylinder surface. Hence, the vortex shedding frequency may be obtained from time series of the pressure. For every time step in the simulations, the pressure and velocity components are obtained at a fixed location (x=0.6, y=0.2, z=0 in a Cartesian coordinate system with origin at the cylinder center) in the near wake of the cylinder. The point is illustrated in figure 9.

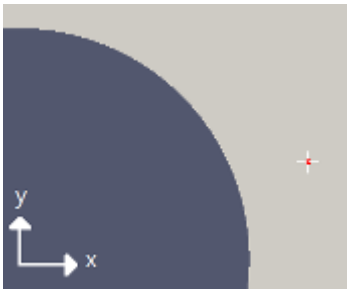

Figure 9: Probe location in the near wake of the cylinder

The frequency of C_L and p may be calculated straight forward as number of cycles divided by elapsed time. The frequency may also be calculated from spectral analysis by Fast Fourier Transform (FFT) of the time series. These analyses are performed in Matlab. The script for FFT is written based on the description of the built-in function `fft` in Matlab Help [49] and attached in Appendix B.

3.6 Numerical stability, convergence and accuracy

To ensure numerical stability in the solutions of explicit methods where diffusion is negligible the following criterion; the CFL-condition, must be fulfilled [50, pp. 136]:

$$\frac{U\triangle t}{\triangle x} < 1 \tag{3.8}$$

The expression on the left hand side is termed the *Courant number* where $\triangle t$ is the time step, $\triangle x$ is the element length and U is the velocity. For further reading on numerical methods, reference is given to [50, 45].

The following criterion for convergence is suggested: the value of any parameter should not differ by more than 1-3% between two subsequent time steps, between two subsequent element sizes or between two subsequent grids. Convergence is assessed in terms of the mean drag coefficient, the root-mean-square lift coefficient and the Strouhals number. The criteria are adapted from Ong [2] applying a similar, though less rigorous, criterion of 5% change between consecutive grids. Convergence of the grid is assessed by refining the mesh in terms of applying successively smaller elements. The grid is considered to

be sufficiently fine when the parameters do not differ by more than 1-3% between two succeeding grids.

For a cylinder in infinite fluid and uniform inflow the true value of the mean lift coefficient is zero. Thus, if the value of lift coefficient is close to zero, small changes in the lift coefficient may cause large relative changes. Hence, the mean lift coefficient is unsuitable in order to assess convergence for this case. On this basis the root-mean-square of the lift coefficient is considered to be a more appropriate value in order to assess convergence. For the cylinder in uniform inflow, the following acceptance criterion is suggested for the mean lift coefficient: the absolute value should be smaller than or equal to 0.05.

4 Flow around a circular cylinder in uniform cross-flow

4.1 Two-dimensional (2D)flow

4.1.1 Simulation setup

A circular cylinder in infinite fluid and uniform incident cross-flow constitutes the basic case and forms the foundation for the succeeding work. The flow is at first simplified to a two dimensional (2D) case. The problem definition sketch is given in figure 10 with the assigned boundary conditions. The simulations are performed at $Re = 100$ with a cylinder diameter of $D = 1$ m, uniform inflow of $U = 1$ m/s and $\nu = 0.01$ m^2/s.

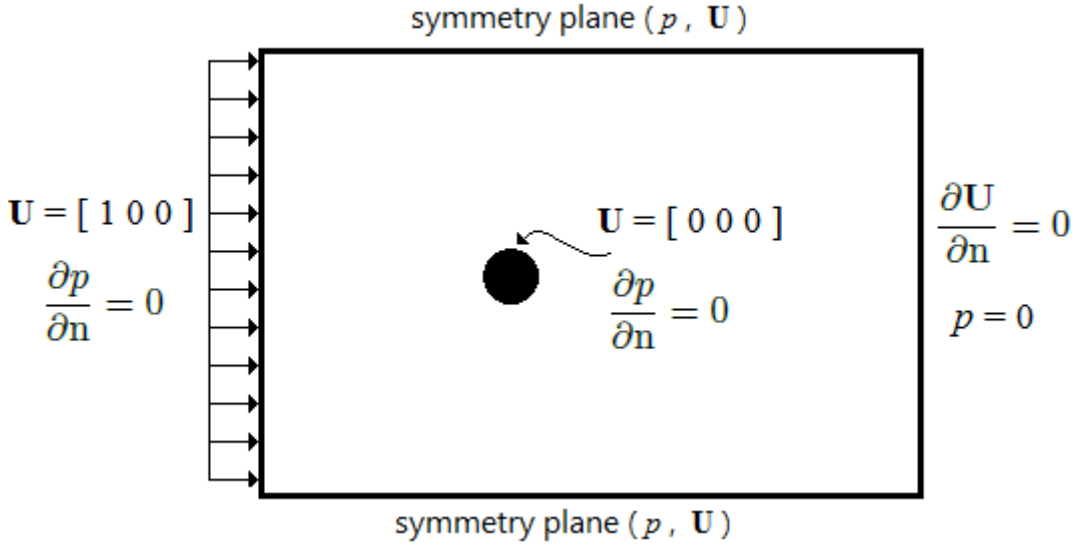

Figure 10: Problem definition for 2D cylinder in uniform cross-flow.

The influence of domain size, element size, element distribution and time step are investigated on two different grids: A and B. The grid is schematically depicted in figure 11 where D is the cylinder diameter. The number of elements are varied along the segments denoted K, L, M, N and O in figure 11. L extends along the complete circumferential of the cylinder cross section. Grid A and B are identical with the exception for the value of L. The length of segment M is $0.5D$ and most effort is put on grid refinement in this region close to the cylinder in order to capture the dynamics in the boundary layer. According to Sumer and Fredsøe [9, p. 3], the boundary layer thickness is $\delta = \mathcal{O}(0.1D)$ in this case:

$$\frac{\delta}{D} = \mathcal{O}\left(\frac{1}{\sqrt{Re}}\right) \tag{4.1}$$

Different domain sizes are obtained by varying the value of a in figure 11: a= {5, 10, 15 } D. The values are given for every mesh in table 4 where Δr denotes the characteristic element length in the radial direction for the elements closest to the cylinder surface and Δs denotes the characteristic element length along the cylinder surface for the elements closest to the cylinder surface. Grid A2b and B2 are depicted in figure 12 and 13, respectively. All simulations start at time $t = 0$ and must overcome an initial transient phase ending at about $t = 120$-140 sec. Hence, the simulations are run to $t = 200$ sec to ensure the solution to overcome the transient phase.

4.1.2 Results overview

The results, in terms of Strouhals number and drag and lift coefficients, are given in table 5. As described in section 3.5, the Strouhals number is obtained from time series of lift coefficient and time series of pressure. In table 5, this is denoted by St (C_L) and St (p), respectively. The frequency of C_L and p may be calculated straight forward as number of cycles divided by elapsed time. If not stated otherwise, this is the applied method to obtain the values of St given in table 5. The Strouhals number may also be calculated from spectral analysis by Fast Fourier Transform (FFT) of the time series, indicated by [a] in the table. Visualizations of the flow are given in Appendix C.

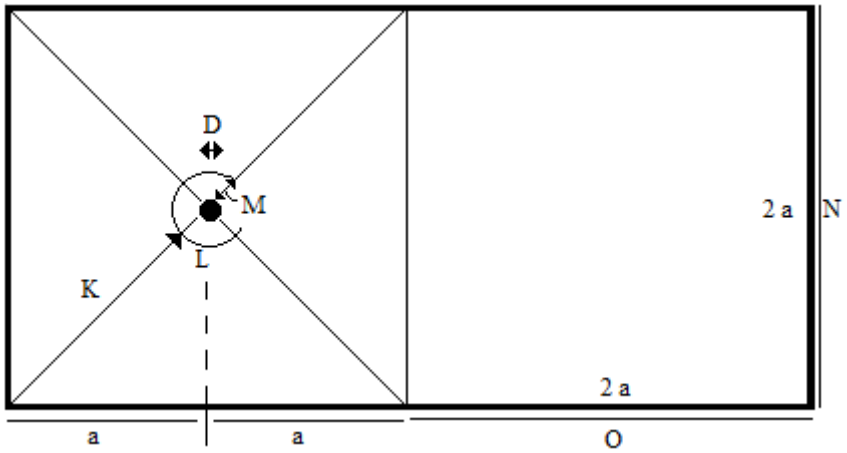

Figure 11: Sketch of grid geometry for a cylinder in uniform cross-flow.

Table 4: Grid properties for a cylinder in uniform cross-flow

Grid	Domain size a	Tot number of elements	K elem	L elem	M elem	N elem	O elem	Δs	Δr
A1	10	13 000	50	200	10	50	20	0.0157	0.0500
A2a	5	26 000	100	200	20	50	40	0.0157	0.0250
A2b	10	26 000	100	200	20	50	40	0.0157	0.0250
A2c	15	26 000	100	200	20	50	40	0.0157	0.0250
A3	10	30 000	100	200	40	50	40	0.0157	0.0125
A4	10	34 000	100	200	60	50	40	0.0157	0.0083
B1	10	26 000	50	400	10	100	20	0.0079	0.0500
B2	10	52 000	100	400	20	100	40	0.0079	0.0250
B3a	5	60 000	100	400	40	100	40	0.0079	0.0125
B3b	10	60 000	100	400	40	100	40	0.0079	0.0125
B3c	15	60 000	100	400	40	100	40	0.0079	0.0125
B4	10	68 000	100	400	60	100	40	0.0079	0.0083

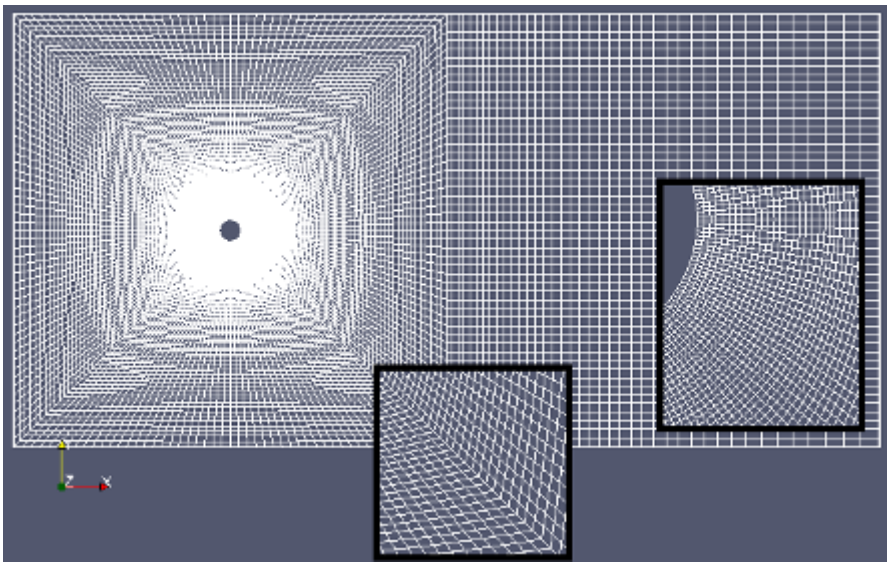

Figure 12: Grid A2b

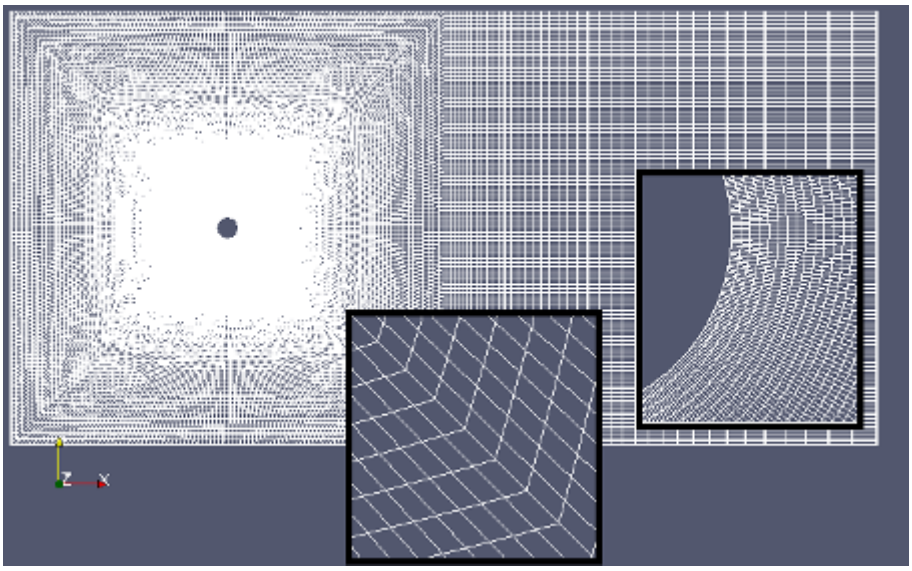

Figure 13: Grid B2

Table 5: Results for varying time step, domain size and element size for a 2D cylinder in uniform cross-flow

Time step Δt sec	$\overline{C_D}$	C_D peak-peak	$\overline{C_L}$	C_L peak-peak	$\sqrt{\overline{C_L'^2}}$	St (C_L)	St (p)
Grid A1							
0.01	1.404	0.03	-0.0076	0.74		0.166	
0.005	1.405	0.07	-0.0130	0.74		0.167	
0.0025	1.405	0.02	-0.0093	0.74		0.167	
0.00125	1.406	0.02	-0.0085	0.74		0.168	
0.0005	1.405	0.02	0.0100	0.74		0.168	
Grid A2a							
0.001	1.492	0.02	-0.0097	0.73	0.253	0.171[a]	0.183[a]
Grid A2b							
0.005	1.377	0.02	-0.0006	0.69		0.166	
0.0025	1.377	0.02	-0.0140	0.69		0.166	
0.00125	1.376	0.02	-0.0140	0.69		0.166	
0.001	1.390	0.02	0.0095	0.69	0.245	0.171[a]	0.168[a]
Grid A2c							
0.001	1.364	0.02	-0.0006	0.68	0.240	0.171[a]	0.168[a]
Grid A3							
0.001	1.385	0.02	0.0026	0.68	0.240	0.171[a]	0.168[a]
Grid A4							
0.001	1.385	0.02	-0.0020	0.67	0.239	0.171[a]	0.168[a]
Grid B1							
0.005	1.409	0.03	-0.0012	0.75		0.168	
0.0025	1.409	0.03	-0.0012	0.75		0.168	
0.00125	1.409	0.02	0.0002	0.75		0.169	
0.0005	1.409	0.02	0.0078	0.75		0.169	
Grid B2							
0.005	1.379	0.02	-0.0003	0.69		0.167	
0.0025	1.380	0.02	-0.0130	0.70		0.167	
0.001	1.394	0.02	-0.0004	0.70	0.246	0.171[a]	0.168[a]
Grid B3a							
0.001	1.491	0.02	-0.0073	0.72	0.254	0.183[a]	0.176[a]
Grid B3b							
0.001	1.389	0.02	-0.0004	0.69	0.242	0.171[a]	0.168[a]
Grid B3c							
0.001	1.363	0.02	-0.0013	0.67	0.236	0.171[a]	0.168[a]
Grid B4							
0.001	1.389	0.02	-0.0054	0.68	0.243	0.171[a]	0.168[a]

[a] denotes analysis by Fast Fourier Transform.

4.1.3 Investigation of time step

The influence of the choice of time step is investigated for grid A1, A2, B1 and B2 on a domain with a=10. The time steps are chosen with due respect to the CFL-condition in section 3.6. The repeating time steps are 0.005 sec, 0.0025 sec, 0.00125 sec and 0.0005 sec.

With reference to table 5, observations for every separate grid indicate independence of the choice of time step on the values of Strouhals number St, averaged drag coefficient $\overline{C_D}$, peak-to-peak of drag coefficient C_D and peak-to-peak of lift coefficient C_L. However, exceptions are $\overline{C_D}$ for $\Delta t = 0.001$ sec on grids A2 and B2 and the peak-to-peak values of drag coefficient C_D for the two largest time steps, 0.01 sec and 0.005 sec, for Grid A1.

Convergence is assessed on the basis of $\overline{C_D}$, $\overline{C_L}$ and St with a convergence criterion of 3%. The differences is 1% in $\overline{C_D}$ related to grids A2 and B2. Hence, these results are within the limits of the convergence criterion. Additionally, the Strouhal number differs based on the method of calculation: Calculations by FFT or number of cycles divided by elapsed time from time series of either lift coefficient or pressure. However, the differences are in the order of 1-3% and hence within the desired convergence criterion. The results obtained within one method of calculation display negligible variations with changing time step and different grids. The results for averaged lift coefficient $\overline{C_L}$ are well within an absolute value of 0.05. However, if applying the more rigorously criterion of 0.01 some simulations with the intermediate time steps on the grids A1, A2 and B2 will not pass this criterion.

This investigation suffers from the use of one domain only. Despite this fact, the choice of time step is concluded to be of less importance as long as the CFL condition is fulfilled. On this basis a time step of 0.001 sec are chosen for the subsequent simulations.

4.1.4 Investigation of domain size

Various domains are investigated for grid A2 and B3 with a time step $\Delta t = 0.001$ sec. The domains are varied while keeping the total number of elements constant. Further, the element distribution is constant within a distance of $0.5D$ from the cylinder. The element distribution is then somewhat changed in remote areas between subsequent domains in order to obtain smooth transition in element size across the domain. The percentage difference in the results between the subsequent domain sizes are given in table 6.

Table 6: Difference in results due to increasing domain size

Grids	$\Delta\ \overline{C_D}$ %	$\Delta\ C_D$ % peak-peak	$\Delta\ C_L$ % peak-peak	$\Delta\ \sqrt{\overline{C_L'^2}}$ %	Δ St (p) %
A2a →A2b	-6.8	0	-5.5	-3.2	-8.1
A2b →A2c	-1.9	0	-1.4	-2.0	0
B3a →B3b	-6.8	0	-4.2	-4.7	-4.5
B3b →B3c	-1.9	0	-2.9	-2.5	0

In the present study, a convergence criterion of 3% is applied for the domain size. By increasing the grid from domain b to domain c, the results for drag and lift coefficient and Strouhals number differ by less then 3%. On this basis, a domain size with a=$10D$ is chosen for the subsequent simulations. However, if applying a more rigorous criterion like

1%, the larger domain should be applied and even larger domains should be investigated for convergence.

This investigation is performed with the small and coarse grid A2 and the larger fine scaled grid B3 and the obtained results in the present analysis are strikingly similar for both grids. However, the investigation suffers from the use of one time step only.

4.1.5 Investigation of element size and distribution

As stated previously, the results indicate independence of the choice of time step as long as the CFL-condition is fulfilled. In order to investigate the influence of element size, a time step 0.001 sec is applied together with a domain where a=10. The results obtained with a time step 0.00125 sec are utilized for grid A1, A2 and B1. Grids A and B have 200 and 400 elements, respectively, along the cylinder circumferential. Grid 1,2 3, and 4 have increasing number of elements in the radial direction. The values of M are 10, 20, 40 and 60, respectively. Thus, from grid 1 to grid 2, and from grid 2 to grid 3, the number of elements increase by a factor of 2 in the radial direction in the near region of the cylinder ($0.5D$).

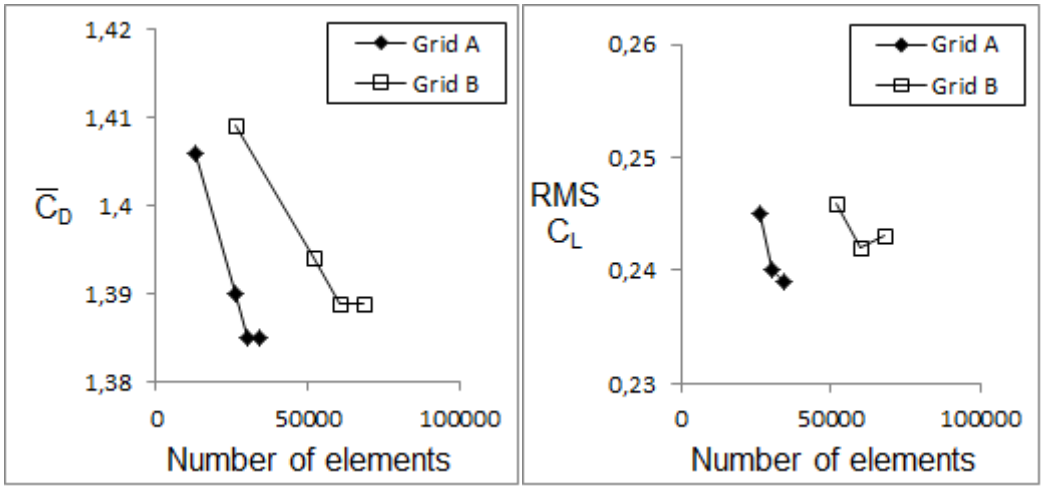

(a) Mean drag coefficient (b) Root-mean-square lift coefficient

Figure 14: Calculated force coefficients for a cylinder in uniform cross-flow on grids with different number of elements

First, the influence of increasing the number of element in radial direction is investigated on grid A and B separately. The subsequent results are compared from A1 through A2 and A3 to A4. Similarly the results from B1 through B2 and B3 to B4 are investigated. The results of the investigation is given in table 7. According to section 3.6, convergence should be based on the mean drag coefficient, the root-mean-square of the lift coefficient and Strouhals number. With reference to table 5, the Strouhals number is evidently identical for the changing grids and a time step of 0.001 sec. Hence, a further investigation of the Strouhal number is omitted in the succeeding discussion of grid convergence.

With reference to table 7 and figure 14, the changes between consecutive element refinement (1→2, 2→3 and 3→4) are strikingly similar for grid A and B.

The value of $\overline{C_D}$ evidently converges for both grid A and B. The convergence is slower for $\sqrt{\overline{C_L'^2}}$. $\overline{C_D}$ does not change from grid A3 to A4, or from B3 to B4, and the accom-

panying change in root-mean-square of the lift coefficient is 0.4% for both. Applying a convergence criterion of 1%, a further grid improvement from A3 to A4, or from B3 to B4, provides negligible improvement of the accuracy in the simulation. For a less rigorous criterion of e.g. 3%, grid A2 and B2 may be considered satisfactory based on a similar consideration.

Table 7: Differences in results due increasing number of elements in the radial direction

Grids	$\Delta\ \overline{C_D}$ %	$\Delta\ C_D$ % peak-peak	$\Delta\ C_L$ % peak-peak	$\Delta\ \sqrt{\overline{C_L'^2}}$ %
A1 →A2	-1.1	0	-6.8	
A2 →A3	-0.4	0	-1.5	-2.0
A3 →A4	0	0	-1.5	-0.4
B1 →B2	-1.1	0	-6.8	
B2 →B3	-0.4	0	-1.4	-1.6
B3 →B4	0	0	-1.5	0.4

Second, the number of elements in radial direction is kept constant, while investigating the influence of increasing the number along the circumference. Hence, the investigation consists of comparing the results from A1 and B1, A2 and B2, A3 and B3, and A4 and B4. The results of this investigation are given in table 8. Again applying a convergence criterion of 1%, the change of $\overline{C_D}$ is well within the criterion for every grid, except for grid 1. The change of $\sqrt{\overline{C_L'^2}}$ is within the criterion for grid 2 and 3, although it fails for grid 4.

Combining the results from the investigations of element size, the radial spacing of grid 3 and circumferential spacing of grid A satisfy the convergence criterion of maximum 1% change. Thus, grid A3 is expected to give satisfactory results.

Table 8: Differences in results due to increasing number of elements in the circumferential direction

Grids	$\Delta\ \overline{C_D}$ %	$\Delta\ C_D$ % peak-peak	$\Delta\ C_L$ % peak-peak	$\Delta\ \sqrt{\overline{C_L'^2}}$ %
A1 →B1	-1.1	0	6.8	
A2 →B2	0.3	0	1.5	0.4
A3 →B3	0.3	0	1.5	0.8
A4 →B4	0.3	0	1.5	1.77

It is assumed that the aspect ratio Λ, i.e. the ratio between the length and height, of the elements is of some importance in the sense that the elements should not be to compressed or pancake shaped. The aspect ratio Λ is here evaluated for the elements closest to the cylinder surface in terms of the ratio $\Delta r : \Delta s$. Square elements are expected to yield the best results and hence an aspect ratio of 1 is ideal. The aspect ratio decreases subsequently from grid A1 where $\Lambda \approx 3.2$ to $\Lambda \approx 0.5$ at A4. At grid A3, $\Lambda \approx 0.8$. On grid B the aspect ratio decrease subsequently from $\Lambda \approx 6.3$ at grid B1 to $\Lambda \approx 1.1$ at B4. The aspect ratio at grid B1 is considered to be somewhat large, while the remaining

values are considered to be within reasonable bounds. Additionally, the aspect ratio may be considered in the more distant fluid domain with reference to figures 12 and 13. The aspect ratio is observed to be close to 1 on grid A2 and close to 2 on grid B2.

4.2 Three dimensional (3D) flow

4.2.1 Simulation setup

In the preceding section on 2D flow, the influence of domain size, element size and time step have been investigated in detail. On this basis grid A3 with time step $\Delta t = 0.001$ sec is applied for a three dimensional (3D) simulation. In order to create a three dimensional mesh, the two dimensional mesh is extruded in the direction of the cylinder span. The depth of the mesh is $6D$ along the cylinder span. The boundary conditions are as for the 2D case, with exception for the front and back faces which now are symmetry planes. 60 elements are distributed evenly along the span, with the corresponding span-wise element length $\Delta z = 0.1D$. The aspect ratios Λ for the elements closest to the cylinder surface are then expressed by $\Delta z : \Delta x$ and $\Delta z : \Delta y$. With 60 elements along the span; $\Lambda \approx 6; 8$. These values are somewhat large, still the grid is expected to yield satisfactory results. For comparison, Lei et al. [51] successfully applied grids where $\Lambda = 20$ in simulations at $Re = 1000$.

Recalling from section 1.1.2, the larger three-dimensional flow structures (mode A) have a characteristic length of 3.96D-4.1D along the cylinder span at low Reynolds numbers [8]. Hence, the cylinder span should be longer than $\approx 4D$ in order to successfully reproduce the three-dimensional flow features. However, three-dimensional effects are expected to be negligible for the flow around a circular cylinder in uniform cross-flow at $Re = 100$ as the flow is mainly 2D [8]. For consistency, the same span is applied in all the 3D simulations in the present study. On this basis a span-wise length of $6D$ is chosen.

For comparison, Cao and Wan [16] applied a span of length $4.1D$ with a constant span-wise element length $\Delta z = 0.1D$ for numerical studies at $Re = 100 - 300$, Lei et al [51] applied a constant span-wise element length $\Delta z = 0.1D$ on spans of length $1 - 6D$ at $Re = 1000$ and Heggernes [17] applied a span of maximum $3.288D$ with a span-wise element length $\Delta z \approx 0.06D$ at $Re = 265$. Despite the relatively short cylinder in the simulations by Heggernes, both modes of vortex shedding, mode A and mode B, were present in the calculations. Lei et al concluded that 2D simulations and 3D simulations with span lengths less than $2D$ were insufficient to achieve reliable results. Further, they suggested that spans of length ≥ 4 could match the real span-wise wavelength of the three-dimensional flow features.

4.2.2 Results overview

The results are given in table 9 in terms of Strouhal number and drag and lift coefficients. The results for two-dimensional simulations on grid A3 with an equal time step $\Delta t = 0.001$ are repeated for the purpose of comparison. Visualizations of the flow are given in Appendix C.

Table 9: Cross-sectional results for 2D and 3D simulations of a cylinder in uniform cross-flow

Grids	$\overline{C_D}$	C_D % peak-peak	$\overline{C_L}$	C_L % peak-peak	$\sqrt{\overline{C_L'^2}}$	St(C_L)
A3 (2D)	1.385	0.02	0.0026	0.68	0.240	0.171
A3 (3D)	1.385	0.02	-0.0018	0.68	0.239	0.171

4.3 Discussion

According to the present investigations, time step and domain size satisfy convergence for a criterion of maximum 3% change between two subsequent time steps and domain sizes, respectively. The convergence for element size is satisfied within a criterion of 1%.

The final results in terms of $\overline{C_D}$, root-mean-square C_L and St obtained in the present study may be extracted from table 5: $\overline{C_D} = 1.39$, root-mean-square $C_L = 0.24$ and St=0.168. It is considered more accurate to calculate St based on the pressure as a direct measure of vortex shedding rather than the lift coefficient being an integrated quantity. These results may be compared to the reference values in table 1. The resulting value of mean drag coefficient is within the scatter 1.26-1.43 in the reference values obtained from experiments. However, the deviation is about 5% compared to the value 1.33 in the experimental study by Williamson [15]. The resulting value of root-mean-square lift coefficient is within the scatter 0.227-0.244 in the reference values. However, the deviation is about 6% compared to the empirical correlation value of 0.227 by Norberg [10]. The resulting value of St is within the scatter of the reference values. However, the deviation is about 2% when comparing to the value 0.164 by Norberg [10] and Williamson [15]. To summarize, the results in the present study are within the scatter of the reported values in the literature. The results differ by 2-6% to the standard benchmark values. However, these differences are limited to the second decimal for the force coefficient and the third decimal for the Strouhals number. On this basis, the results of the simulations in the present study are satisfactory.

Only minor differences are observed in 2D and 3D simulations. This is presumably due to the attributed two-dimensional pattern of the flow around a circular cylinder at this Reynolds number.

5 Flow around a circular cylinder near a plane wall

5.1 Two-dimensional (2D) flow

5.1.1 Simulation setup

A plane wall is introduced in the proximity of the cylinder and the flow is simulated with the cylinder positioned at various gaps: $G/D = 0.2;\ 0.5;\ 1.0$. The 2D case constitutes the starting point for the investigation of this case. The simulations are performed at $Re = 100$ with a cylinder diameter of $D = 1$ m, uniform inflow of $U = 1$ m/s and $\nu = 0.01$ m^2/s. The problem definition sketch is given in figure 15 with the assigned boundary conditions.

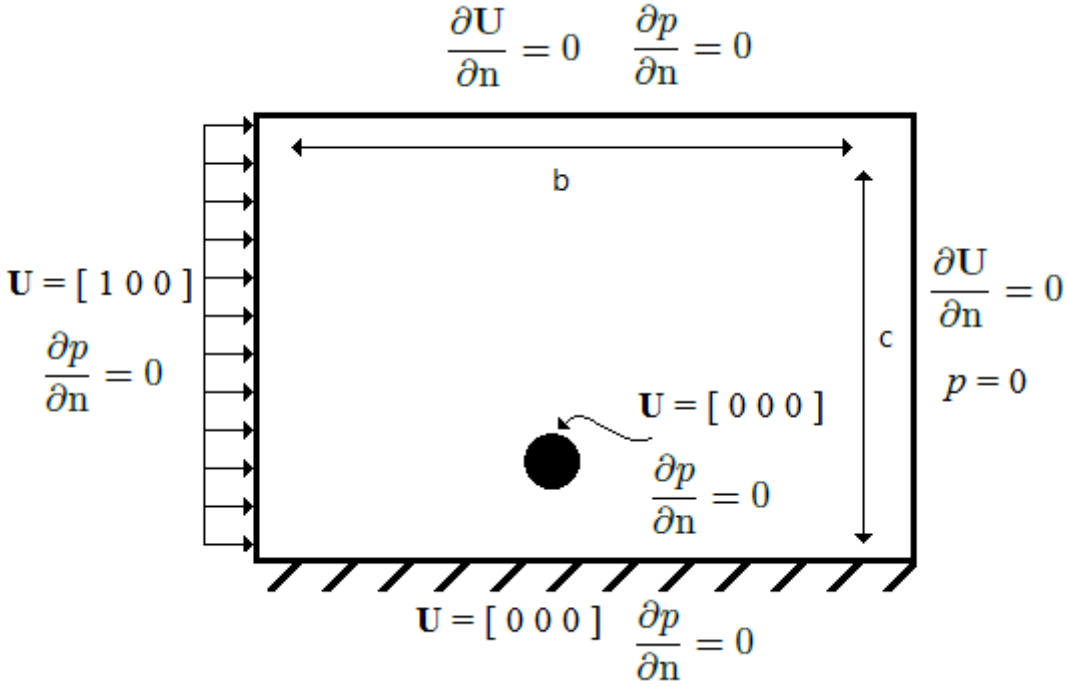

Figure 15: Problem definition for 2D cylinder near a plane wall

The preceding investigation (sec. 4.1.3) indicates independence of choice of time step to the extent the CFL-condition is fulfilled. The investigation of time step is therefore omitted for the present flow configuration. Three different approaches for grid design are pursued to resolve the flow field of the current case: Grid C, D and E. First, the influence of domain size is investigated for $G/D = 0.2$ on grid C. Next, various element sizes and element distributions are investigated for $G/D = 0.2$ on the three different types of grids: C, D and E. Grids of type E are applied for $G/D = 0.5$ and grids of type C and E are applied for $G/D = 1.0$.

Grid D1 is depicted in figure 16, while the two other approaches for grid design, C2 and E1, are depicted in Appendix D.

Table 10 lists the main properties for the grids applied for $G/D = 0.2;\ 0.5;\ 1.0$. Δr denotes the characteristic element length in the radial direction for the elements closest to the cylinder surface, Δs denotes the characteristic element length along the cylinder surface for the elements closest to the cylinder surface, Δx denotes the element length along the wall for the elements far upstream and downstream of the cylinder, Δy denotes

the element length in the wall-normal direction for the element closest to the wall far upstream and downstream of the cylinder. Different domain sizes are obtained by varying the length of b and c in figure 15: b=$\{40, 45, 50\}D$; c=$\{15, 20\}D$. By varying b, only the upstream distance is changed. The downstream end of the domain is fixed at $30D$ from the center of the cylinder. All simulations start at time $t = 0$ and are run long enough for the solution to overcome the initial transient phase. The transient phase is due to the numerics and does not represent the true physics of the flow. The flows at $G/D = 0.2$ and $G/D = 0.5$ are observed to reach a time independent steady state. In order to attain this state, the simulations should run to at least $t = 600$ sec. The flow at $G/D = 1.0$ does not reach a steady state, but the artificial transient phase is overcome at $t \approx 250$ sec. The simulations are then run an additional 150 sec to $t = 400$ sec.

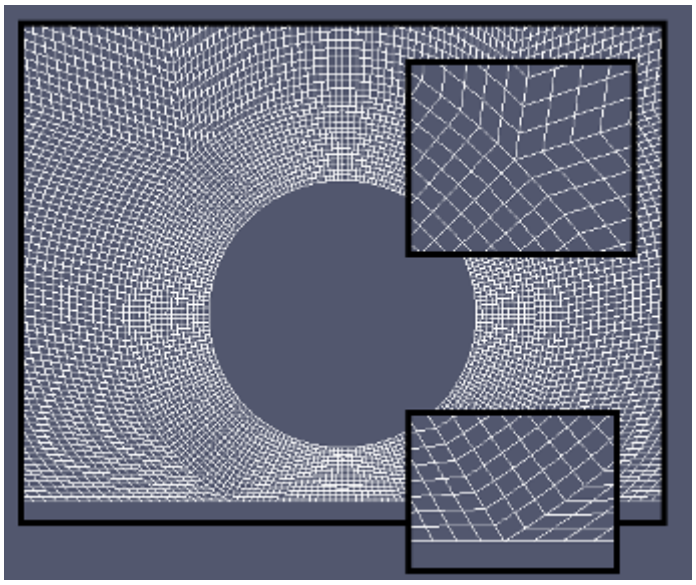

Figure 16: Close-up view of grid D1

Table 10: Grid properties for a cylinder near a plane wall at various gap ratios

Grid	b	c	Tot number of elements	Δr radial	Δs circumfer.	Δx along plate	Δy perp. plate
$G/D = 0.2$							
C1	40	15.7	55 000	0.011	0.016	0.200	0.028
C2	45	15.7	58 750	0.011	0.016	0.200	0.028
C3	50	15.7	62 500	0.011	0.016	0.200	0.028
D1	45	20.7	96 242	0.020	0.016	0.100	0.047
D2	45	20.7	100 542	0.011	0.011	0.100	0.047
E1	45	20.7	114 625	0.016	0.009	0.075	0.027
$G/D = 0.5$							
E2	45	21	36 800	0.033	0.045	0.169	0.176
E3	45	21	49 493	0.016	0.016	0.071	0.052
E4	45	21	53 777	0.010	0.016	0.050	0.052
$G/D = 1.0$							
C5	45	21.5	66 945	0.040	0.030	0.085	0.050
E5	45	21.5	53 017	0.018	0.016	0.070	0.030

5.1.2 Assessing the boundary layer at the wall

A uniform horizontal velocity is prescribed at the upstream inlet. The no-slip condition is imposed on the wall. Hence, a boundary layer forms at the wall. The boundary layer thickness is expected to increase with the distance along the wall. It is also of interest to investigate the boundary layer thickness at the cylinder's position with the cylinder removed. On this basis a 2D simulation is performed on a grid of 290 $\times$150 elements with element clustering near the wall and uniform element distribution, $\Delta x = 0.15$, in the streamwise direction. The minimum element height is $\Delta y = 0.015$ (perpendicular to the wall). The inlet is placed $15D$ upstream of the cylinder location and the boundary conditions are as stated above in figure 15.

Figure 17 presents the velocity profiles in terms of horizontal velocity u/U_0 and vertical distance from the wall y/D at different positions x/D along the wall. $x = 0$ denotes the cylinder's position.

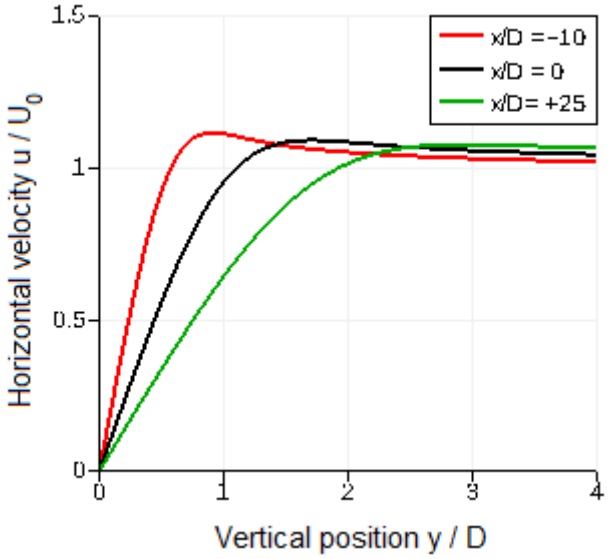

Figure 17: Velocity profiles in the boundary layer along the wall - with the cylinder removed

At $x/D = -10$ (red line), a peak is observed in the velocity profile and the boundary layer is evidently not fully developed. This peak is still evident at the cylinder's location $x/D = 0$ (black line). Far downstream at $x/D = +25$ (green line) the boundary layer exhibits the look of a fully developed profile. From the simulation, the boundary layer thickness is found to be approximately $\delta/D = 1.7$ at the cylinder's position. It should be emphasized that the boundary layer is not fully developed at the position of the cylinder. For comparison, the boundary layer thickness at the cylinder's position is $\delta/D = 1.94$ when obtained from the exact flat plate solution of Blasius [40, pp. 221-233]:

$$\delta_{99\%} = \frac{5.0x}{\sqrt{Re_x}} \tag{5.1}$$

where $\delta_{99\%}$ denotes the boundary layer thickness in terms of the vertical distance from the wall where $u/U_0 = 0.99$. In the expression by Blasius, the distance x is measured from the upstream end of the plate.

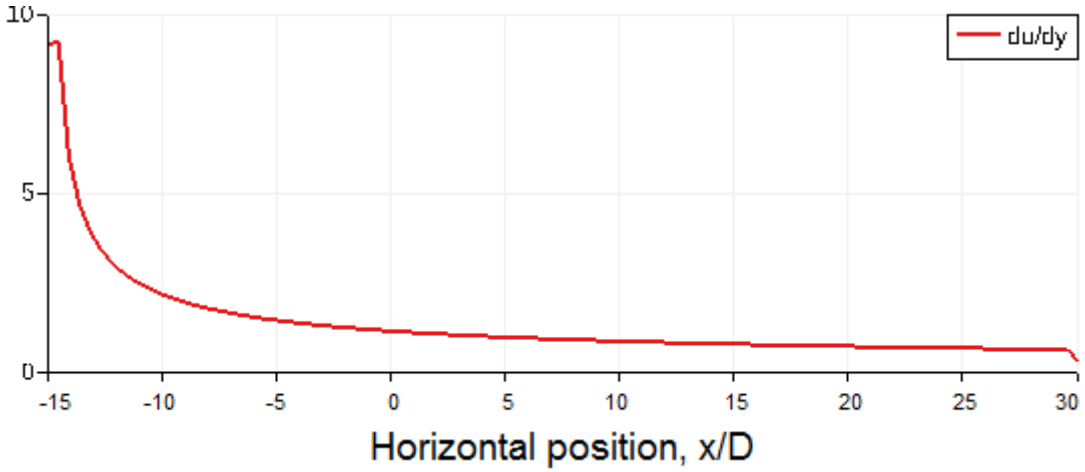

Figure 18: Velocity gradient du/dy along the wall - with the cylinder removed

5.1.3 Results overview

The obtained results in terms of lift and drag coefficient and Strouhals number, are given in table 11.

Table 11: Results for a cylinder near a plane wall at various gap ratios

Grid	Δt [sec]	$\overline{C_D}$	$\overline{C_L}$	$\sqrt{\overline{C_L'^2}}$	St (C_L)	St (p)
$G/D = 0.2$						
C1	0.001	0.896	0.468		-	-
C2	0.001	0.726	0.377		-	-
C3	0.001	0.583	0.303		-	-
D1	0.001	0.727	0.375		-	-
D2	0.001	0.726	0.376		-	-
E1	0.0005	0.728	0.376		-	-
$G/D = 0.5$						
E2	0.001	0.954	0.050		-	-
E3	0.001	0.965	0.052		-	-
E4	0.001	0.961	0.055		-	-
$G/D = 1.0$						
C5	0.001	1.342	0.0099	0.129	0.169^a	0.169^a
E5	0.001	1.336	-0.0001	0.122	0.171^a	0.168^a

[a] denotes analysis by FFT.

5.1.4 Investigation of domain size

A high local pressure is observed at the intersection of the inlet and the wall in figure 19. This is assumed to be due to the prescribed velocity of 1 m/s over the entire inlet and the no-slip condition at the wall. Hence, an accompanying large velocity gradient is observed in this region, figure 18. The large velocity gradient propagates along the wall. However, the velocity gradient is heavily reduced $10D$ downstream of the inlet. On this basis, the inlet is positioned $15D$ upstream of the cylinder.

For the subsequent grids C1, C2 and C3, the cylinder is positioned successively further downstream of the inlet. As the boundary layer develops along the wall, this migration of the cylinder causes a deeper submersion of the cylinder in the boundary layer. On this basis the differences in the results between grid C1, C2 and C3 are believed to be mainly due to the development of the boundary layer along the wall with accompanying lower local velocities near the cylinder which cause decreasing drag and lift coefficients.

The location of the lateral boundary of the domain is discussed with reference to the grids at $G/D = 0.2$ where the inlet is positioned $15D$ upstream of the cylinder (b=45): C2, D1 D2, and E1. By increasing the lateral width from c=15.7 to c=20.7 the differences in $\overline{C_D}$ and $\overline{C_L}$ are at most 0.28% and 0.53 %, respectively. This is within a convergence criterion of 1%. On this basis, a lateral domain with c=15.7 is accepted. However, in the present study the largest domain (c=20.7) is applied.

Lei et al. [1] performed numerical simulations of the flow around a circular cylinder near a plane boundary at $Re = 80 - 1000$. The inlet was located $16D$ upstream of the cylinder center and the outlet at $20D$ downstream of the cylinder. No differences were found when increasing the domain downstream of the cylinder by locating the outlet $40D$ downstream. The top lateral boundary was located $10D$ away from the cylinder center in their simulations, noting that the position of the lateral boundaries had no significance when they were positioned at least a distance $8D$ from the cylinder center. With reference to the domain of Lei et al, the domain in the present study is considered to be sufficient.

As a conclusive remark, the inlet and outlet are considered to be located sufficiently far upstream and downstream of the cylinder, respectively. The lateral width of the domain of minimum $20.7D$ is quite conservative and according to the present investigation the width is larger than necessary.

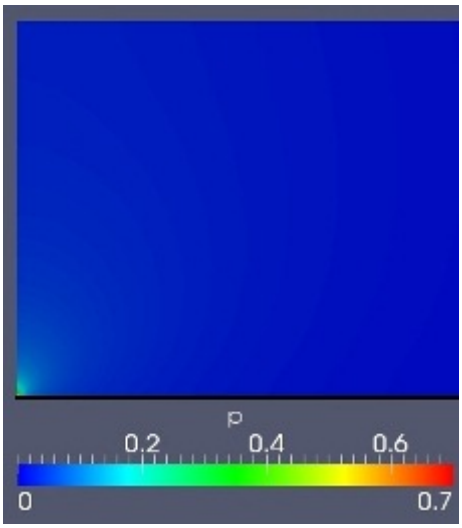

Figure 19: Local pressure peak at the intersection between wall and inlet (steady state)

5.1.5 Investigation of element size and distribution

By inspection of the results in table 11 for a cylinder at $G/D = 0.2$ positioned $15D$ downstream of the inlet, the spread in the results are at most 0.27% and 0.53% for $\overline{C_D}$ and $\overline{C_L}$, respectively.

Between the most coarse (E1) and the finest (E4) grid at $G/D = 0.5$, the results differ by 0.7% and 10% for $\overline{C_D}$ and $\overline{C_L}$, respectively. As the flow reach a steady state, root-mean-square C_L' is not an available alternative for the investigation of convergence. However, the change in $\overline{C_L}$ is limited to 0.005.

The results for $G/D = 1.0$ differ by 0.4%, 5.4% and 1.2% for $\overline{C_D}$, root-mean-square C_L' and $\mathrm{St}(C_L)$, respectively. $\overline{C_D}$ and St fulfill a convergence criterion of 1% and 3%, respectively. However, the convergence criterion is not met for root-mean-square C_L' in the simulations of the flow at this gap. This is a drawback to the validation of the present results.

Applying a convergence criterion of 1%, all the investigated grids are found to give satisfactory results with exception for $\overline{C_L}$ at $G/D = 0.5$ and root-mean-square C_L' at $G/D = 1.0$. However, at $G/D = 0.5$ the difference is at most 0.005. On this basis, the final results at $G/D = 0.2$ and $G/D = 0.5$ are considered to be sufficiently validated. Additional simulations at $G/D = 1.0$ are desirable in order to assess convergence.

The pressure contours should exhibit a smooth look, and not any abrupt breaks. In the simulations at $G/D = 0.5$, the contour lines of the pressure reveal a region of local spurious pressure in the downstream part of the gap region. This is indicated in figure 20. This shortcoming in the simulation is evident for all the different approaches of grid design applied in the present study at this gap ratio. No remedy is found to counteract this drawback. However, the pressure defect is very local in space; in a region near the intersecting grid lines in the figure. As the pressure defect is limited it is not expected to severely contaminate the solution. However, no reliable conclusion can be drawn with reference to the influence of this error in the pressure distribution.

The influence of varying the total number of elements is illustrated for $\overline{C_D}$ and $\overline{C_L}$ at $G/D = 0.2; 0.5; 1.0$ in figures 21 and 22.

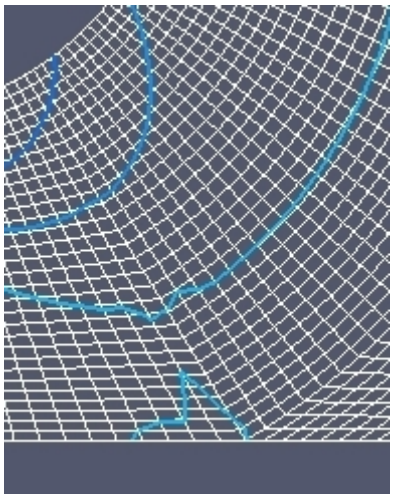

Figure 20: Pressure defect at $G/D = 0.5$

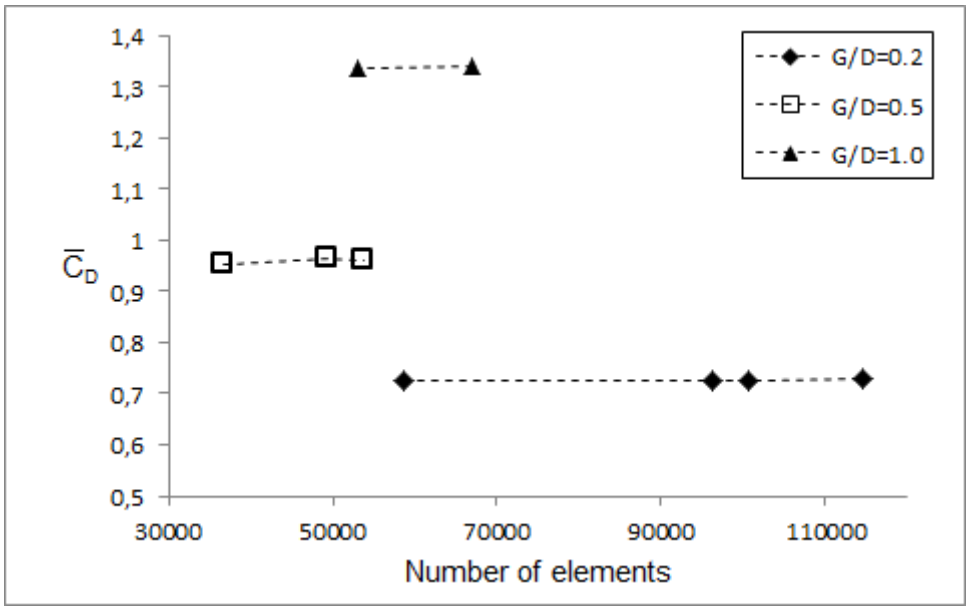

Figure 21: Drag coefficient for different gap ratios on 2D grids with different number of elements

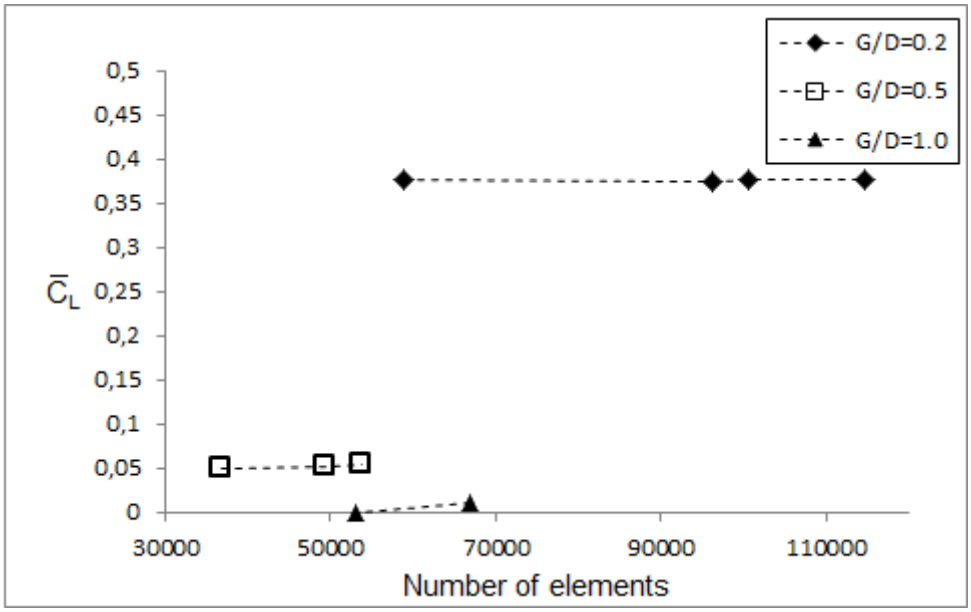

Figure 22: Lift coefficient for different gap ratios on 2D grids with different number of elements

5.2 Three-dimensional (3D) flow

5.2.1 Simulation setup

A 3D simulation is performed for a cylinder located at $G/D = 0.5$ utilizing the 2D grid E3. The 2D grid is extruded a distance $6D$ in the direction along the span in order to create a three dimensional grid. The grid has 60 elements evenly distributed along the span with a span-wise element length $\Delta z = 0.1D$. This is similar to the 3D simulation of the flow around a circular cylinder in uniform cross-flow. The boundary conditions are

equal to the 2D case, with exception for the front and back (2D) faces which now are symmetry planes. The applied time step is $\Delta t = 0.001$ sec.

5.2.2 Results overview

Unfortunately this 3D simulation is only allowed to run to time $t = 129$ sec due to the limited time span of this work and the late execution of this simulation. Accordingly, the simulation does not overcome the initial transient phase to obtain the expected steady state. The results are given in table 12 in terms of Strouhal number and drag and lift coefficients. The results for the corresponding two-dimensional simulation with an equal time step $\Delta t = 0.001$ are repeated here for the purpose of comparison. The sectional C_D and C_L for 2D and 3D show remarkably good agreement, depicted by coinciding time series in Appendix E. Although the simulation does not attain the final state, it can still be concluded that there are insignificant differences between 2D and 3D simulations for the flow at this gap ratio.

Table 12: Cross-sectional results for 2D and 3D simulations of a cylinder near a plane wall at $G/D = 0.5$

Grid	t [sec]	$\overline{C_D}$	$\overline{C_L}$	$\sqrt{\overline{C_L'^2}}$	St (C_L)
E3 (2D)	t=600	0.965	0.052	-	-
E3 (2D)	t=129	0.978	0.055	-	-
E3 (3D)	t=129	0.978	0.056	-	-

5.3 Results and discussion

At both $G/D = 0.2$ and $G/D = 0.5$ the flow obtain a steady state where vortex shedding is suppressed. As the cylinder is moved further away from the wall, vortex shedding is observed at $G/D = 1.0$. Time series of the drag and lift coefficient at $G/D = 0.2$ and $G/D = 1.0$ are given in figures 23 and 24, respectively.

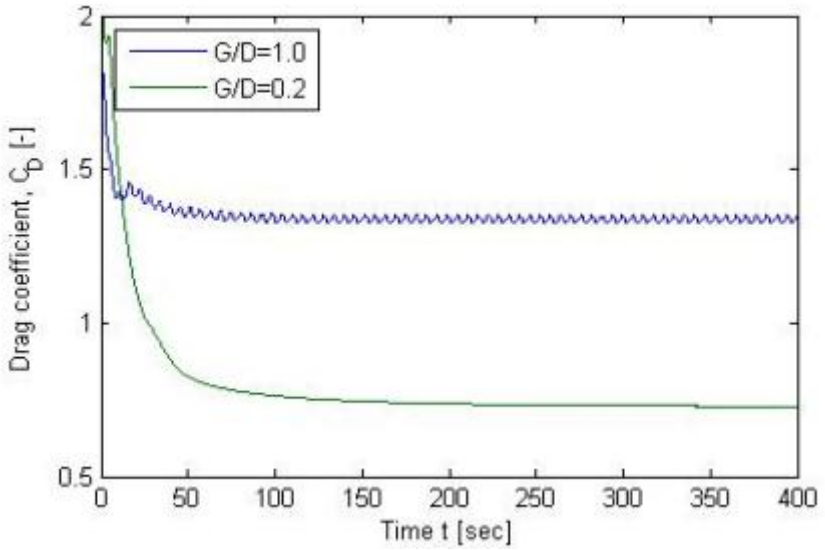

Figure 23: Time series of drag coeffecient at $G/D = 0.2$ and $G/D = 1.0$

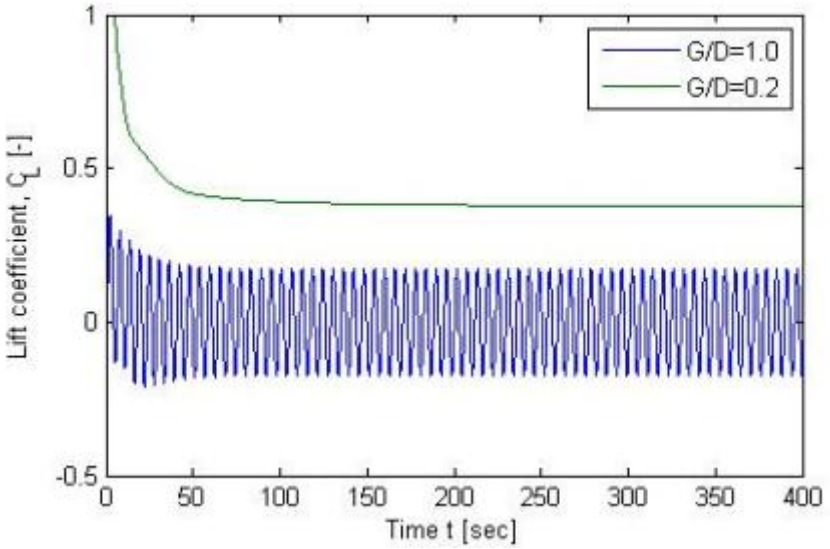

Figure 24: Time series of lift coeffecient at $G/D = 0.2$ and $G/D = 1.0$

5.3.1 Pressure distribution

The pressure distribution at $G/D = 0.2$ is illustrated in figure 25. A distinct persistent negative pressure is observed at the free-stream side of the cylinder and a less pronounced negative pressure is observed at the wall-side of the cylinder. From the figure, the location of the front stagnation point is estimated to be approximately at the cylinder's center line. Consequently, a lift in the direction away from the wall is experienced: $\overline{C_L} = 0.376$.

The pressure distribution at $G/D = 0.5$ is illustrated in figure 26. The front stagnation point is now quite evident and moved slightly away from the wall towards the free-stream side. This is expected to direct the lift towards the wall. However, the negative pressure at the free-stream side is still more distinct than the negative pressure at the wall-side of the cylinder. The result is a weak lift in the direction away from the wall: $\overline{C_L} = 0.05$

The pressure distribution at $G/D = 1.0$ is illustrated in figures 27 - 28 by time series over one period of vortex shedding. As vortex shedding occurs at this gap ratio, oscillatory pressure is observed in the vicinity of the cylinder. The mean lift is approximately zero at this gap ratio. However, from figures 27 and 28, the pressure is still more distinct at the free-stream side, and it persist for a longer time in the wake. A row of alternating high and low pressure regions originating at the free-stream side of the cylinder is clearly visible far downstream of the cylinder. A similar row is not visible at the wall-side of the wake, in particular the positive regions are less visible.

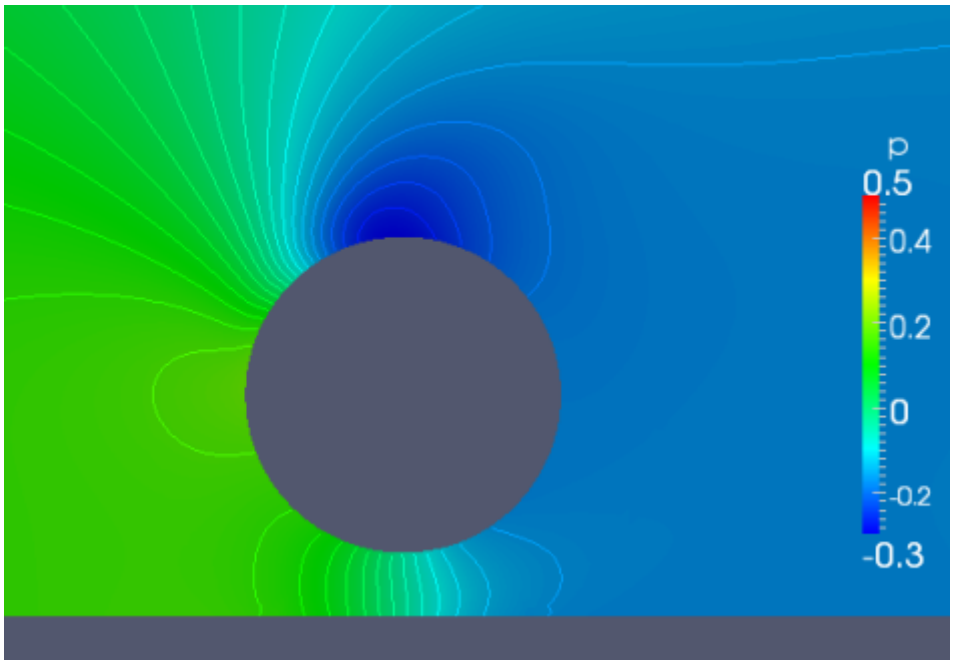

Figure 25: Pressure distribution at $G/D = 0.2$, $t = 600$ sec (steady state)

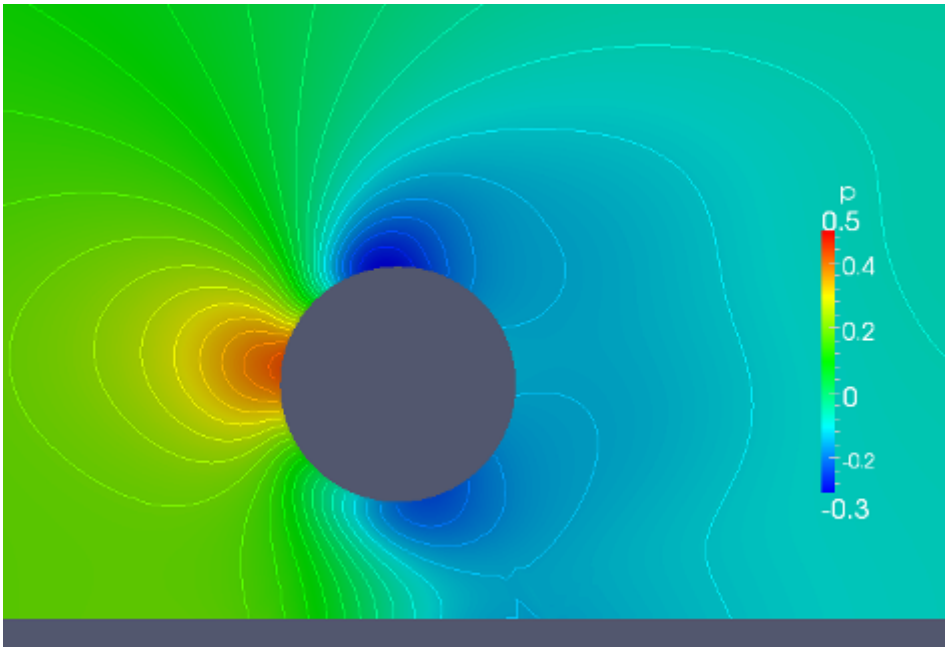

Figure 26: Pressure distribution at $G/D = 0.5$, $t = 600$ sec (steady state)

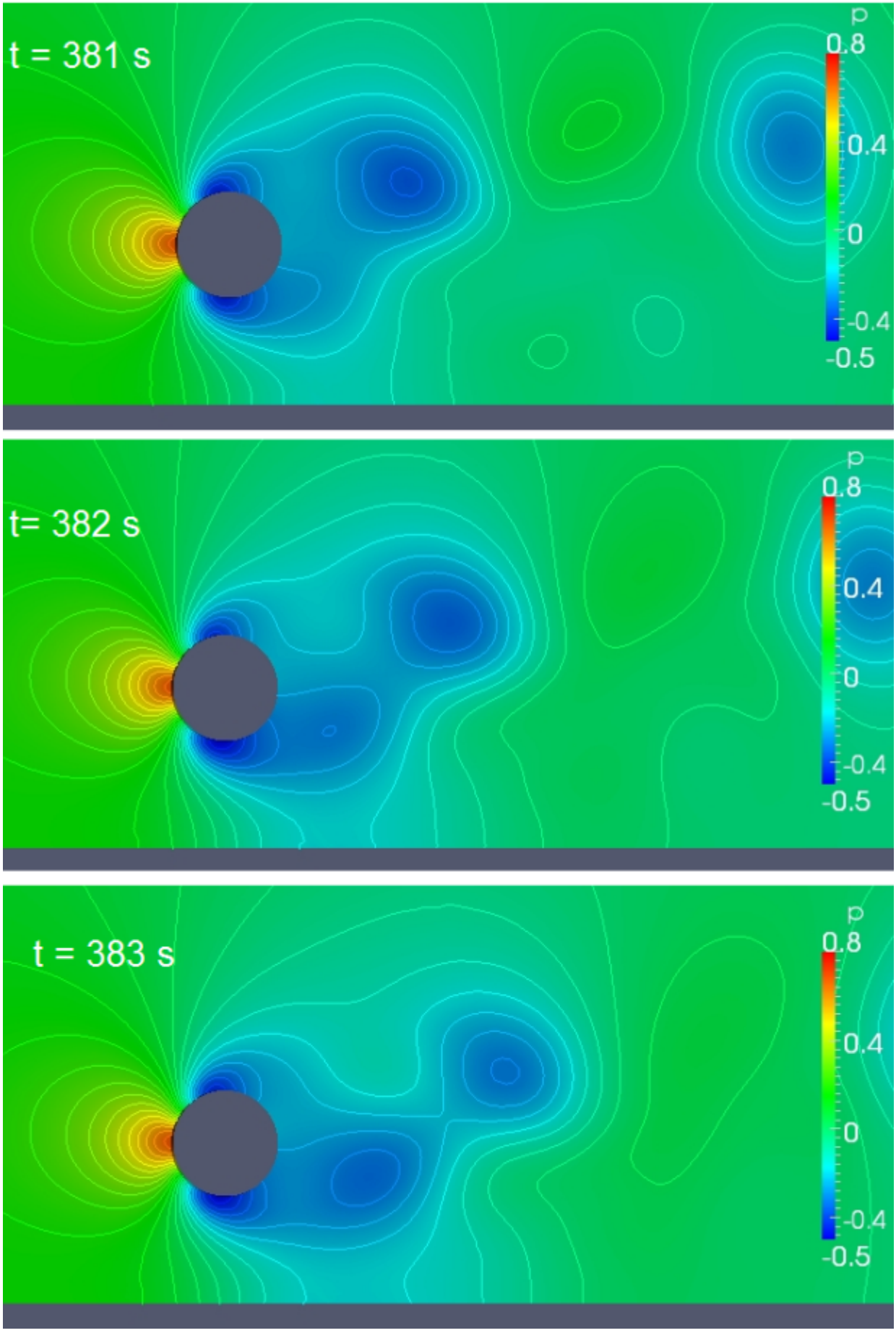

Figure 27: Pressure distribution at $G/D = 1.0$ (Part 1 of 2)

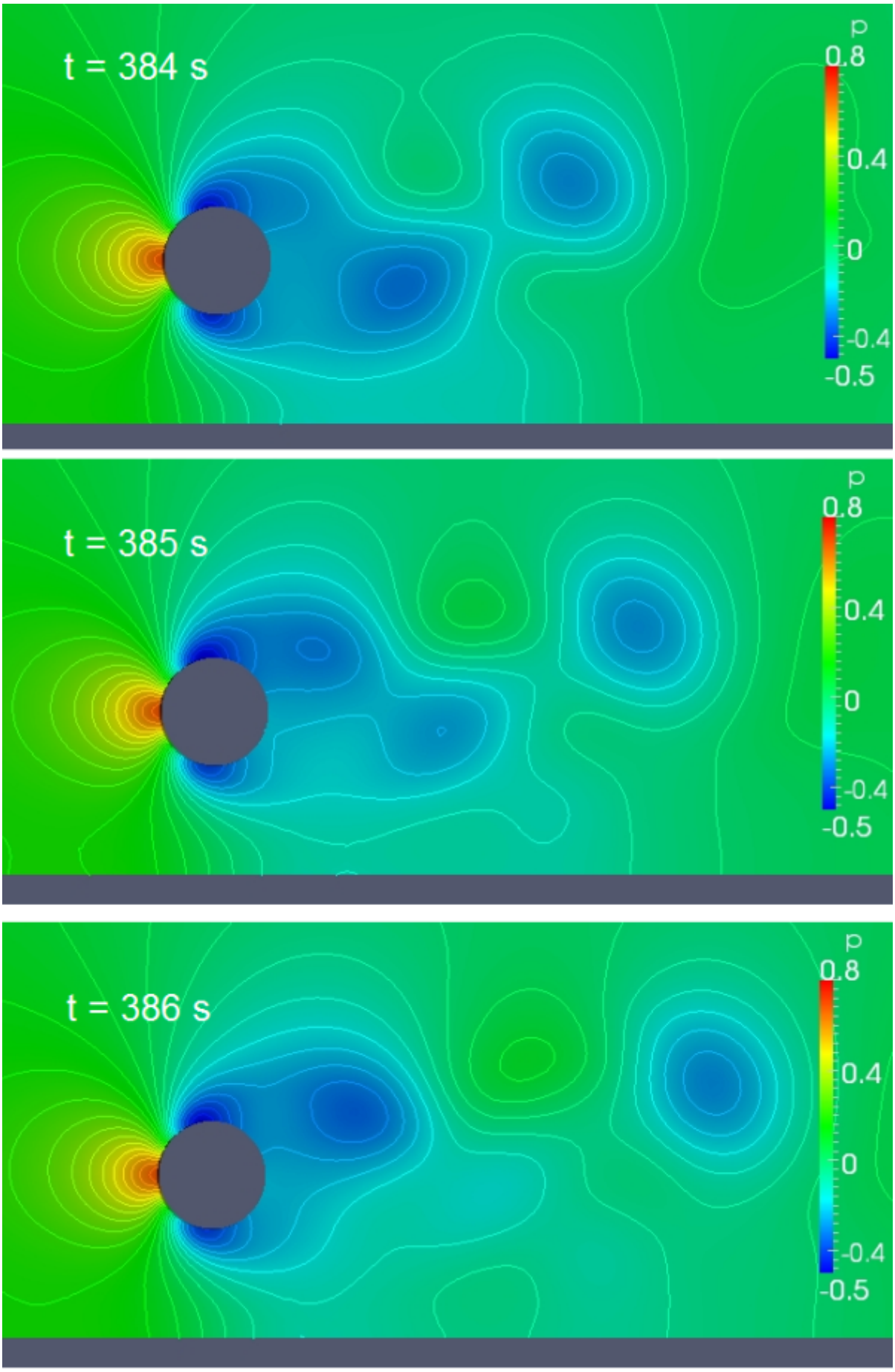

Figure 28: Pressure distribution at $G/D = 1.0$ (Part 2 of 2)

5.3.2 Velocity field

At the smallest gap, $G/D = 0.2$, a weak gap flow is observed in figure 29. Keeping in mind the relative thick boundary layer at the cylinder's position, there are then associated low velocities near the wall in the approaching flow and the weak gap flow is then expected. The cylinder forms an obstacle to the approaching flow and most of the fluid seems to be directed over the top of the cylinder. A recirculation region forms downstream of the cylinder as seen in figure 30. As seen from figure 29, this recirculating flow interacts with the gap flow and the resulting flow in the near wake is directed in the stream normal direction with respect to the free-stream. A reverse flow is observed along the cylinder surface near the free-stream side.

As the gap is increased to $G/D = 0.5$, the gap flow increases both in terms of velocity and mass flow rate and forms a free jet as seen in figure 31. As seen in figure 32, the downstream recirculation region is still present, though it has migrated downstream, possibly due to the stronger gap flow. The near wake of the cylinder is directed away from the wall, possibly due to the interaction between the gap flow and the downstream recirculation region. The near wake is now noticeable more complex.

At the largest gap, $G/D = 1.0$, a violent gap flow and a jet is evident in figures 33 and 34. The downstream recirculation region has now disappeared and regular vortex shedding occurs. It is now of interest to investigate the interaction between the vortex shedding and the wall boundary layer. This may be assessed in terms of comparing visualizations of the velocity field in figures 33 and 34 to plots in Appendix F of the stream normal gradient of the horizontal velocity component evaluated at the wall: $\frac{du}{dy}(y = 0)$. Negative gradients reveal regions of separating and possibly recirculating flow. At this stage it might be appropriate recalling the importance of the velocity gradient with reference to scour application. At all gaps a persistent dominating positive velocity gradient at the wall occurs in the gap immediately below the cylinder. The maximum values are 5, 7 and 5 at $G/D = 0.2$, $G/D = 0.5$ and $G/D = 1.0$, respectively. The increase in du/dy from $G/D = 0.2$ to $G/D = 0.5$ is assumed to be due to the increasing velocities in the gap flow: The velocities increase by a factor of 4, while the gap only increase by a factor of 2.5. As the gap is further increased to $G/D = 1.0$, the effect of the gap apparently has a slightly lower influence on the velocity gradient.

The plots in Appendix F are taken at intervals of 1 sec and correspond to one period of vortex shedding from t=381 sec to 387 sec. The corresponding visualizations of the velocity field in the near wake are taken at the same time instances figures 33 - 34. With reference to Appendix F, the plots to the left are along the entire wall: $x = 0$ at horizontal axis denotes the upstream boundary (the inlet), the cylinder is located at $x = 15$ and the downstream boundary (the outlet) is located at $x = 45$. The plots to the right are enlarged views of the indicated region in the near wake around $x = 20$. With reference to figures 33 - 34, the red lines along the wall indicate regions of negative velocity gradients.

At $G/D = 1.0$, the plot of the velocity gradient exhibits a wavy behavior downstream of the cylinder with the occurrence of positive and negative gradients. In the following is given a short description of the velocities in the wake, wall jet and near backflow region along the wall over one period of vortex shedding from time t=381 sec to t=387 sec. The maximum velocity gradient in the backflow region is well below an absolute value of 1 at all times and hence of minor importance compared to the distinct positive velocity gradient below the cylinder.

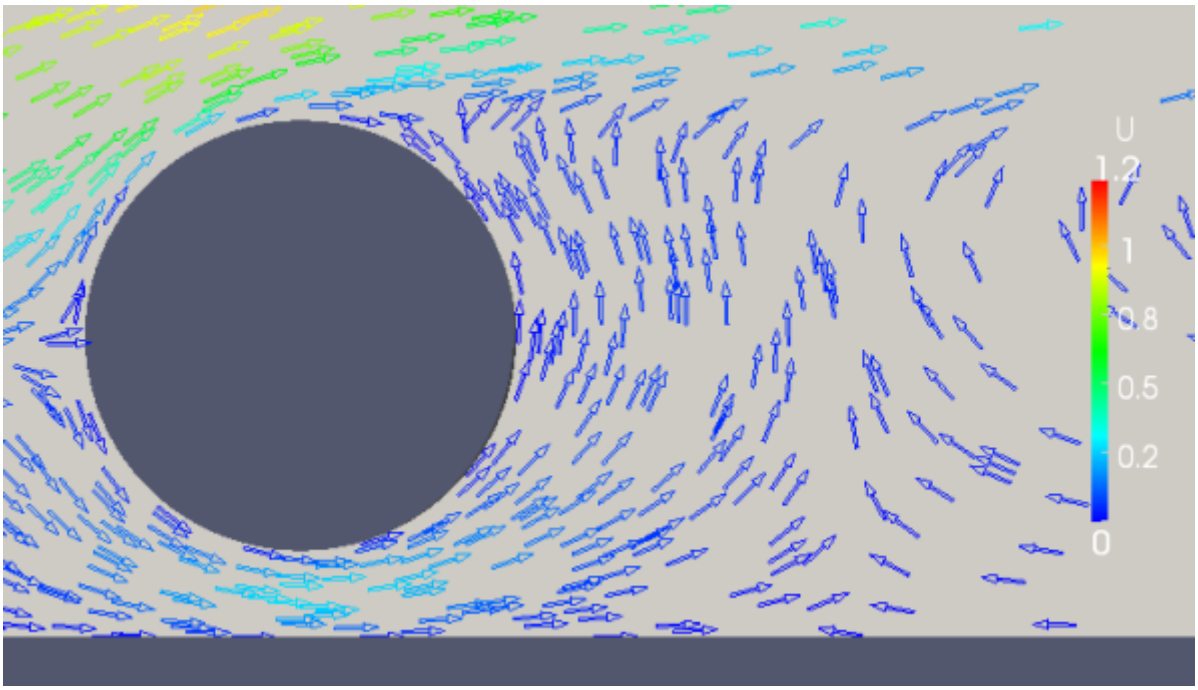

Figure 29: Velocity vectors in the near wake of the cylinder at $G/D = 0.2$, $t = 600$ sec (steady state)

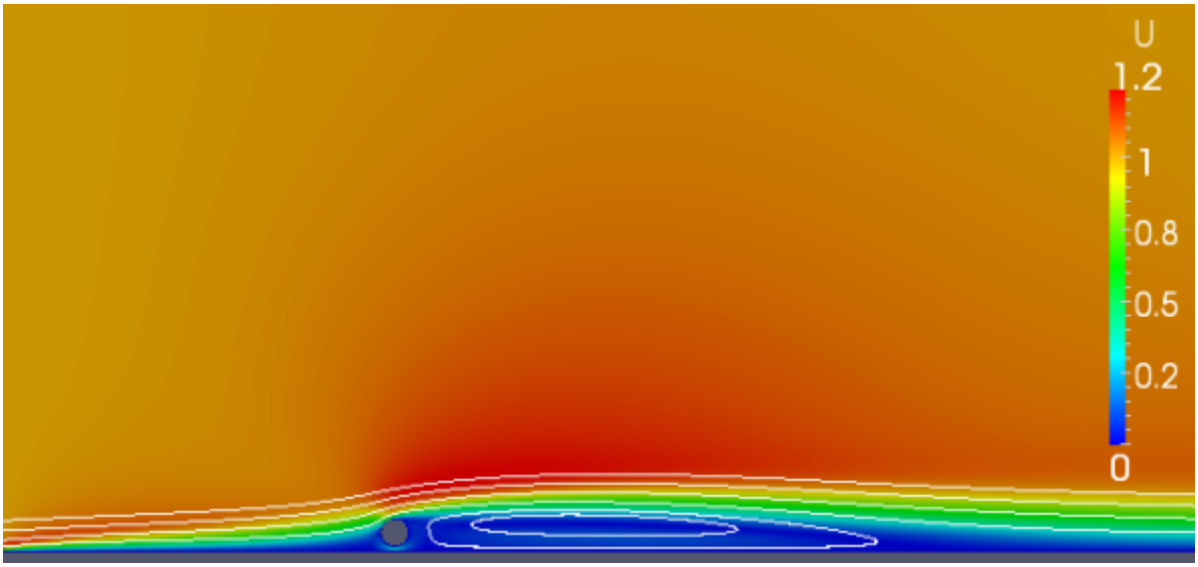

Figure 30: Magnitude of the velocity (scalar) and indicative streamlines at $G/D = 0.2$, $t = 600$ sec (steady state)

At t=381 sec, a negative velocity gradient is evident at the wall in the range $19 < x < 21.5$ and a backflow is visible near the wall. The near wake of the cylinder is slightly deflected away from the wall. The cylinder wake then extends further downstream, deflecting the wall jet towards the wall. In turn, the deflected wall jet moves along the wall and counteract the backflow near the wall. The backflow region is now narrowed and moved downstream to $21 < x < 22.5$ (t=382 sec). At t=383 sec, the cylinder wake is again compressed, allowing the wall jet to direct outwards. Two narrow backflow regions are now evident around $x = 18$ and $x = 22$, respectively.

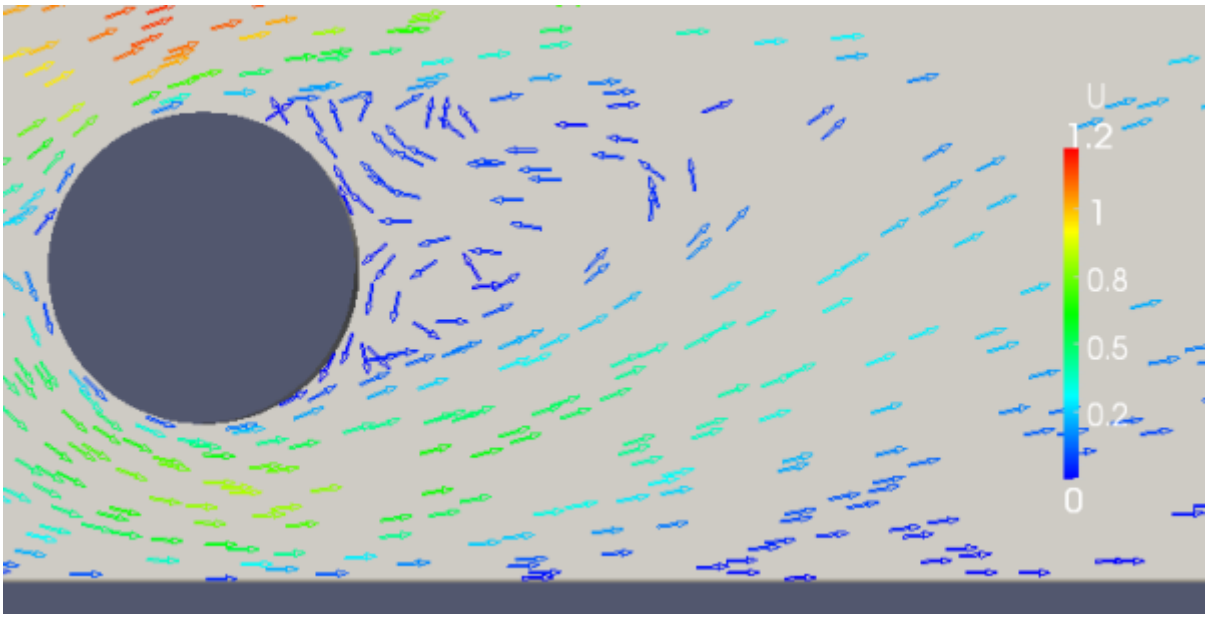

Figure 31: Velocity vectors in the near wake of the cylinder at $G/D = 0.5$, $t = 600$ sec (steady state)

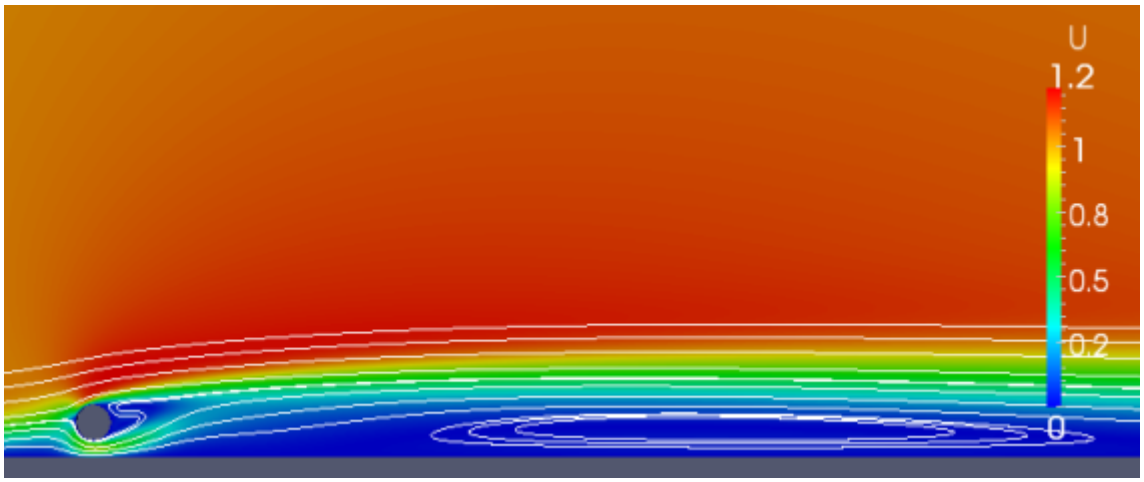

Figure 32: Magnitude of the velocity (scalar) and indicative stream lines at $G/D = 0.5$, $t = 600$ sec (steady state)

Then again the cylinder wake extends further downstream and entraps some of the wall jet. The backflow region around $x = 38$ increases and moves slightly downstream, while the backflow region at $x = 23$ is reduced. The cylinder wake extends even further downstream and the wall jet is further drawn outwards. The near backflow region is now located at $18 < x < 20$. At t=386, the cylinder wake contracts and moves towards the wall, deflecting the wall jet and in turn forcing the backflow downstream to the region $18.5 < x < 21$. At t=387, the cylinder wake extends further downstream and the backflow is forced downstream to $19 < x < 21.5$ which is similar to the initial condition at t=381 sec.

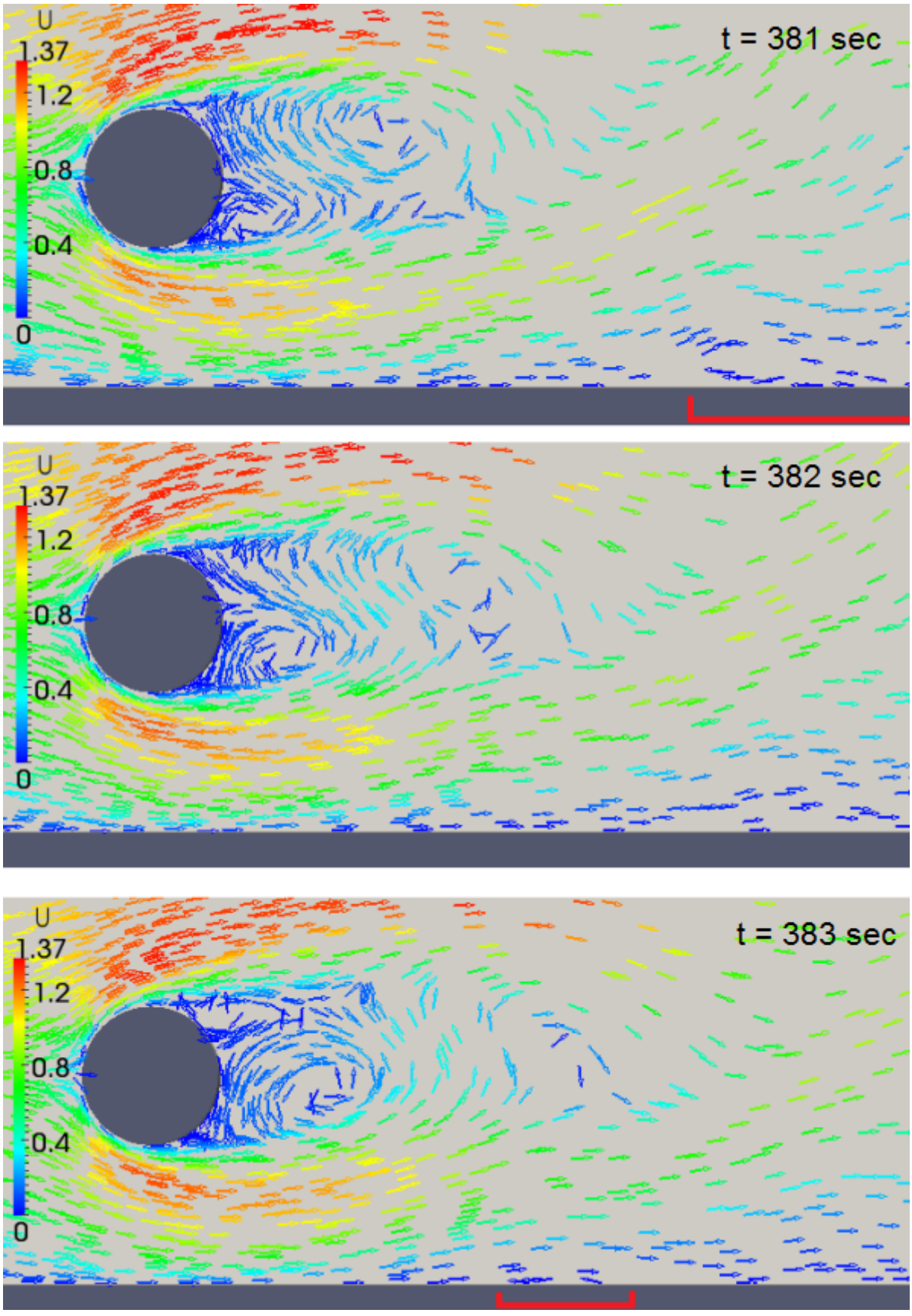

Figure 33: Velocity vectors in the near wake of the cylinder at $G/D = 1.0$ (Part 1 of 2)

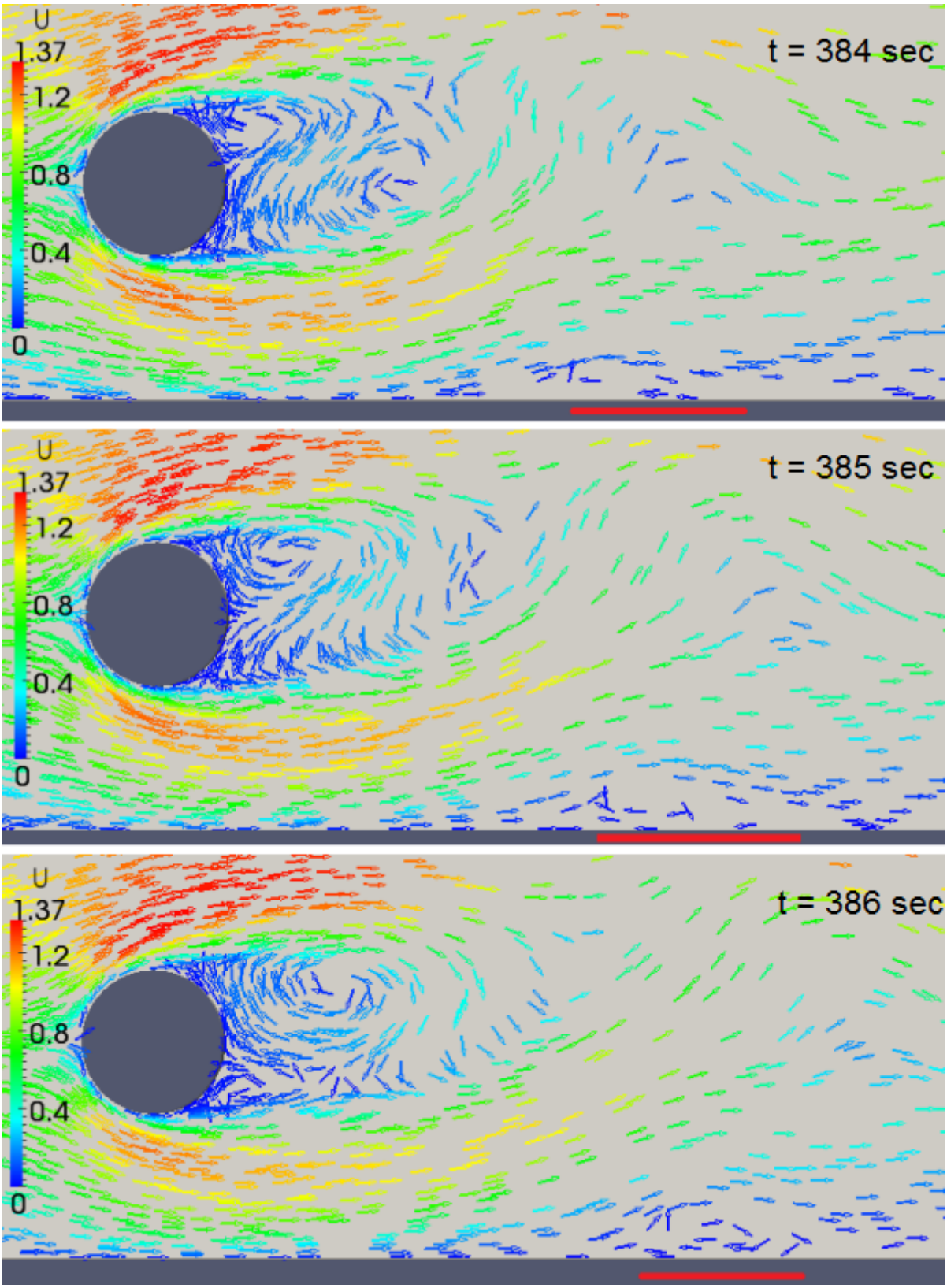

Figure 34: Velocity vectors in the near wake of the cylinder at $G/D = 1.0$ (Part 2 of 2)

5.3.3 Vorticity

The magnitude (without respect to sign) of the vorticity at $G/D = 0.2$ is visualized by a contour plot in figure 35. The largest values of vorticity are concentrated around the upstream part of the free-stream side of the cylinder and in the gap region on both the cylinder and the wall. The free-stream side vorticity is stretched downstream due to the free-stream while the vorticity in the gap region spreads equally upstream and downstream.

A similar contour plot for $G/D = 0.5$ is given in figure 36. At this gap, the vorticity distribution is more symmetric over the horizontal center line of the cylinder. The wall-side vorticity on the cylinder is increased and the region of concentrated vorticity is moved upstream. The vorticity in the gap region is now more stretched downstream, although not to the same extend as on the free-stream side. This is presumably due to the increasing gap flow.

Vortex shedding occurs at $G/D = 1.0$ and this is also evident in terms of visualization of time series of vorticity contours of ω_z in figures 37-38. In these figures contour lines are given in the range $\omega_z = -3.5$ - $+3.5$ to emphasize the vortical dynamics in the wake. Although not shown in the figure, the magnitude of vorticity is still at the same level in the upstream regions at the cylinder surface as at $G/D = 0.2$ and $G/D = 0.5$. Positive vorticity (indicated by green in the figures) originates at the free-stream side of the cylinder and at the wall. Negative vorticity (indicated by red) originates at the wall-side of the cylinder. These three distinct regions of vorticity are evident in figure 37-38. The two sheets of vorticity originating at the cylinder interact and curls up in an alternating manner to form eddies in the wake. The vorticity originating at the wall is observed to interact with the wall-side vorticity from the cylinder. The extent and stretching of these two regions of vorticity are coinciding in time.

The dynamics over the course of one period of vortex shedding is described in the following. At $t = 381$ sec the wall vorticity is stretched into two fingers C1 and C2, C2 being attracted to the wall-side vorticity (A) originating at the cylinder. Both regions of vorticity originating at the cylinder are growing in the near wake of the cylinder. The positive vortex A curls up and interacts with the region of negative vorticity at the free-stream side. This cause the vortex B to be cut off from the region at the free-stream side at $t = 382$ sec. At this time instant all three regions of vorticity have grown further and now the free-stream region bends towards the wall and trigger the shedding of a positive vortex A1. This weak vortex is short lived and at $t = 383$ sec it is only visible as part of a stretched vortex sheet. The wall vorticity C1 is stretched further and at $t = 383$ a small vortex D is shed. The shed vortex B is persistent and convected downstream as time elapses. All three regions of vorticity continues to grow until $t = 386$ sec which is similar to the condition to $t = 381$ sec and which is succeeded by the shedding of a new vortex from the free-stream side. At $t = 384$ a new finger C3 starts to form in the wall region of vorticity. Region C2 curls up alongside region A2. From $t = 384$ sec to $t = 386$ sec, the wall vorticity moves in two directions: the most downstream part C2 following the positive finger A2 and the most upstream part C3 curls up attracted by the region of positive vorticity A3. At $t = 386$ sec region A2 has disappeared and region C2 forms a narrow intestine.

The suppression of vortex shedding at $G/D \leq 0.5$ is higher than the results of $G/D = 0.2 - 0.4$ for $Re = 1{\cdot}10^3 - 1{\cdot}10^5$ reported in the literature. However, the results are in accordance with the results of Lei et al [1] who found vortex shedding to be suppressed for $G/D < 0.9$ at $Re = 100$. According to Lei et al, the strength of vorticity in the three

regions decreases and the thickness of the regions of vorticity increases with decreasing Re. The consequence is suppression of vortex shedding at larger gap ratios for lower Re.

The results are supportive to the suggestion [1, 26, 22] of cancellation of opposite signed vorticity in the near-wall region, illustrated at $G/D = 1.0$. The visualizations of velocity vectors (figures 29, 31, 33 and 34) in the near wake of the cylinder in the present study are in favor of the suggestion by Grass et al. [22]: Vortex shedding suppression is caused by the interaction between the lee-side recirculation region and the gap flow, which inhibits large-scale vortex roll-up.

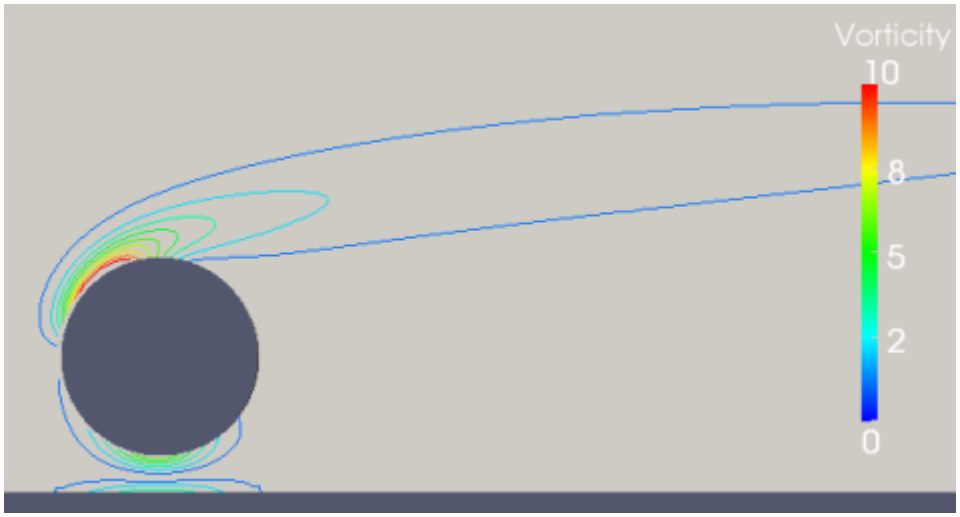

Figure 35: Vorticity contours at $G/D = 0.2$, $t = 600$ sec (steady state)

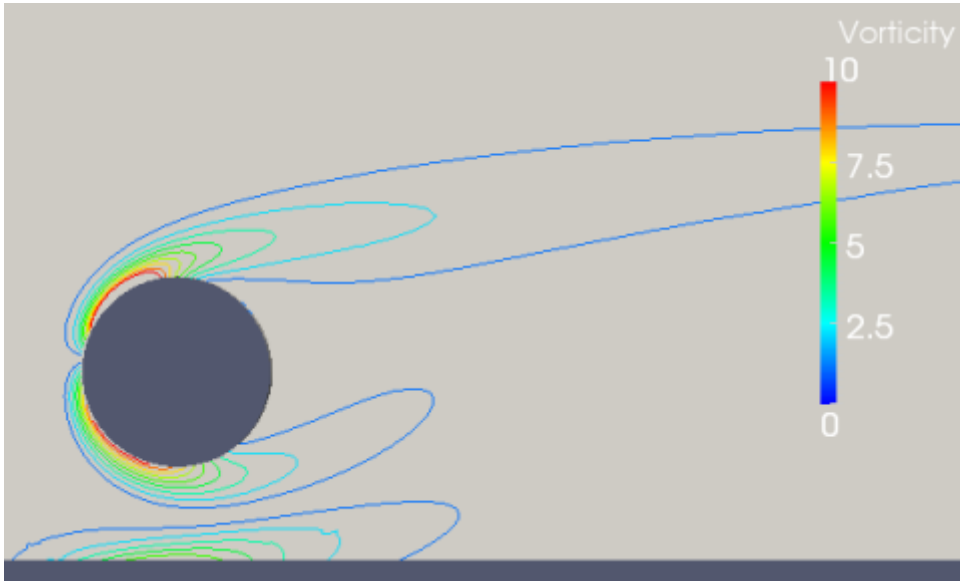

Figure 36: Vorticity contours at $G/D = 0.5$, $t = 600$ sec (steady state)

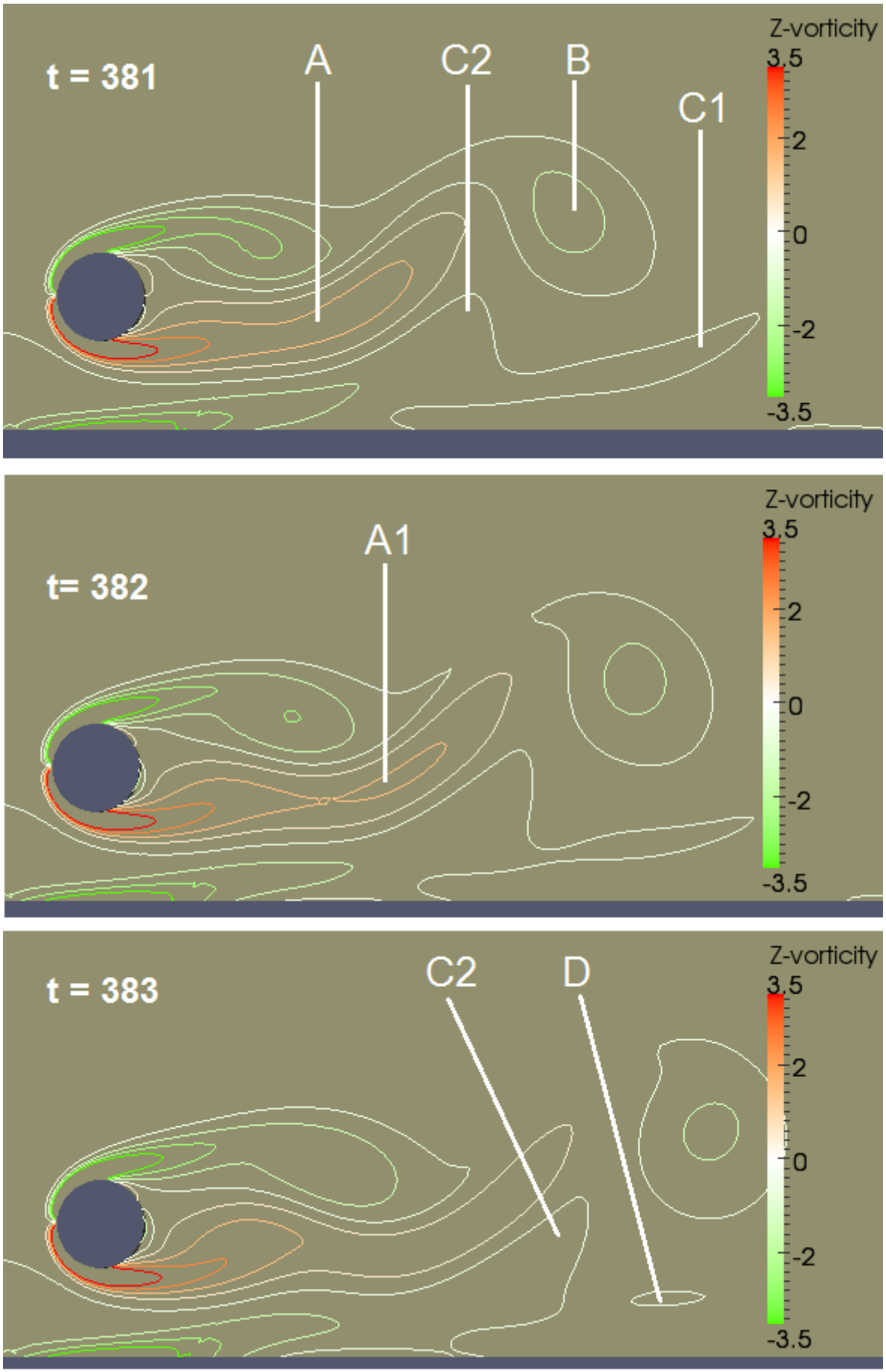

Figure 37: Vorticity contours (ω_z) at $G/D = 1.0$ (Part 1 of 2)

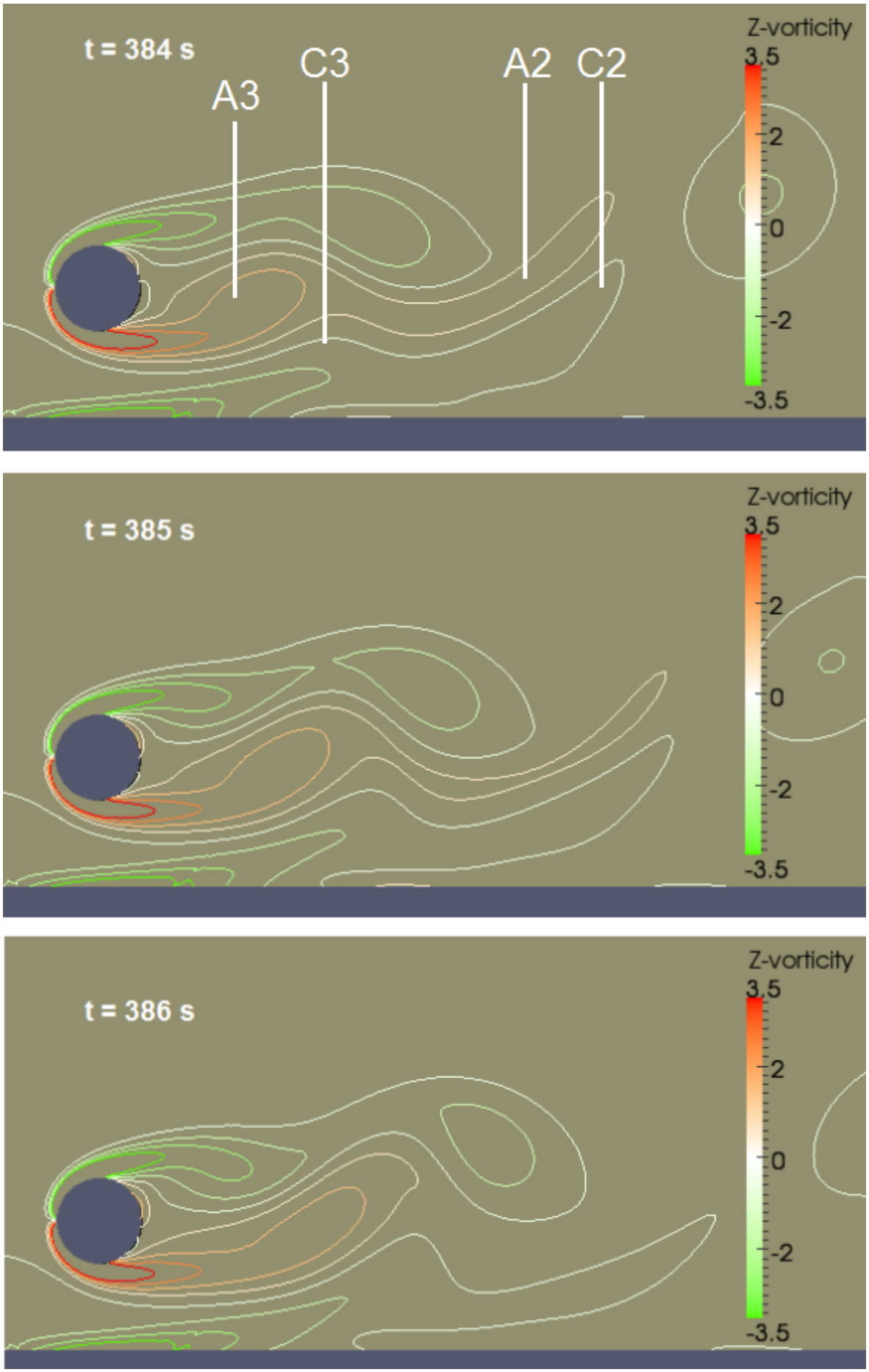

Figure 38: Vorticity contours (ω_z) at $G/D = 1.0$ (Part 2 of 2)

5.3.4 Hydrodynamic quantities for engineering purposes

The variations of Strouhals number and lift and drag coefficient may be expressed with reference to the non-dimensional gap ratio G/D or alternatively G/δ. The latter value may be obtained by the following relation:

$$G/\delta = G/D \cdot D/\delta \tag{5.2}$$

The obtained results, table 13, for the hydrodynamic quantities $\overline{C_D}$, $\overline{C_L}$ root-mean-square C'_L and St are now extracted from table 11 and compared with the results of Lei et al. [1] obtained by 2D numerical simulations at $Re = 100$ with $\delta/D = 1.20$. In the present study, $\delta/D \approx 1.7$. The comparisons are presented in figures 39, 40, 41 and 42. The results from the present study obtained for a cylinder in uniform cross-flow are included at $G/D = \infty$. The exact numbers from the study of Lei et al are acquired by personal communication with Lei [52].

Table 13: Hydrodynamic quantities for a cylinder near a plane wall at various gap ratios (present study)

G/D	G/δ	$\overline{C_D}$	$\overline{C_L}$	$\sqrt{\overline{C'^2_L}}$	St (p)
0.2	0.12	0.73	0.38	-	-
0.5	0.29	0.96	0.05	-	-
1.0	0.59	1.34	0	0.12	0.168
∞	∞	1.39	0	0.24	0.168

As the cylinder is moved sequentially away from the wall, the cylinder gradually encounters larger velocities. Hence, the stagnation pressure and $\overline{C_D}$ are expected to increase with increasing gap ratio. This is confirmed by the observations in the present study. At $G/D = 1.0$, although the cylinder is still inside the boundary layer, $\overline{C_D}$ attains a value close to that of the unconfined cylinder in uniform cross-flow. The monotonic increase and almost linear relation for $G/D \leq 1.0$ is in accordance with the results of Lei et al. However, the increase is more rapid in the present study than in the results of Lei et al. Hence, the values of $\overline{C_D}$ for a given value of G/D are larger in the present study, most pronounced for $G/D = 1.0$. The same trend is observed with respect to G/δ and the deviations are actually amplified on this scale.

The value of $\overline{C_D}$ for the cylinder in unrestricted fluid and uniform cross-flow is lower than the results by Lei et al at $G/D = 2.5$ and $G/D = 3.0$. However, the value from the present study is higher than the reference value of Williamson [15]. Additional gaps $G/D > 1.0$ should be investigated in order to assess if there exists a peak in the drag curve or if the larger values of drag are associated with systematic errors.

$\overline{C_L}$ increases with decreasing G/D and the lift is approximately zero at $G/D = 1.0$. The lift dependence on gap ratio is explained in the preceding section 5.3.1 on pressure field. Negative lift is not observed at any gap in the present study. The results for $G/D = 0.2$ and $G/D = 0.5$ are in good agreement with the results of Lei et al. However, $\overline{C_L}$ at a given value of G/D in the present study is slightly higher than the results of Lei. et al. With reference to G/δ, the results are perhaps in even better agreement with the results of Lei et al as the values are scattered around the curve of Lei et al.

Additional gaps $0.5 < G/D < 1.0$ and $G/D > 1.0$ should be investigated in order to assess the exact shape of the lift curve in this region and specifically to investigate the

occurrence of a negative mean lift. If negative values occurs along the $\overline{C_L}$ curve, the plot with reference to G/δ indicated that these values occurs for $G/D > 1.0$.

The root-mean-square (RMS) C'_L decreases with decreasing gap and the results are in qualitatively good agreement with the results of Lei et al. However, the value at $G/D = 1.0$ is significantly larger than the corresponding value of Lei et al. This discrepancy is even more evident with reference to G/δ. No subsequent increase in RMS C'_L is observed at very small gaps in the present study. Smaller gaps $G/D < 0.2$ should be investigated in order to clarify the development in the immediate proximity of the wall. The value for the unconfined cylinder in uniform cross-flow is in excellent agreement with the results of Lei et al at $G/D = 2.5$ and $G/D = 3.0$.

Vortex shedding at $G/D = 1.0$ and vortex shedding suppression at $G/D = 0.5$ and $G/D = 0.2$ are in accordance with the results of Lei et al. where the smallest gap of vortex shedding was $G/D = 0.9$. In both studies, St exhibits small variation with different gap ratios. As $G/D = 1.0$ is the only gap with vortex shedding in the present study, the basis is sparse for comparison of St to Lei et al. The value of St at $G/D = 1.0$ in the present study is equal to the value for the unconfined cylinder in uniform cross-flow. The latter value is significantly lower than the value at $G/D = 3.0$ of Lei et al, although the value of St for the unconfined cylinder in the present study is larger than the reference values by Norberg [10] and Williamson [15]. With reference to G/δ, vortex shedding takes place at a value below that of Lei et al. Lei et al. observed a small peak at $G/D = 2.5$ and a subsequent monotonic reduction of St for decreasing gap until vortex shedding suppression for $G/D < 0.9$.

Due to the different boundary layers in the two studies, differences are expected when comparing with reference to G/D. Better agreement might be expected when comparing with respect to G/δ. However, contrary to these considerations, the agreement is more convincing with reference to G/D. Nonetheless, previous studies at higher Re have found G/D to be a more dominant parameter than G/δ.

Based on the preceding description, G/D is suggested to be a more appropriate scale than G/δ in order to assess the variations in $\overline{C_D}$, $\overline{C_L}$, root-mean-square C'_L and St. The results are qualitatively in good agreement with the results of Lei et al, with respect to G/D. However, the resulting values in the present study are generally somewhat larger than those by Lei et al.

The discrepancies are most evident at $G/D = 1.0$. The boundary layers in both studies have an almost linear variation over most of the boundary layer thickness. By rough measurements of the velocity profiles, the slope is found to be approximately 1 in both studies [1, fig. 2]. However, the shapes of the velocity profiles in the undisturbed boundary layers differ. A fully developed boundary layer is applied in the study of Lei et al. and the velocity profile has a smooth curved transition starting near $y/D = 0.9$ and reaching the uniform free-stream velocity at $y/D \approx \delta/D = 1.2$. In the present study the boundary layer develops along the wall and a peak (or nose) is evident in the velocity profile. The peak is located at $y/D \approx \delta/D = 1.7$ with a peak velocity of approximately 1.1 m/s. Outwards from the peak, the velocity profile decreases slightly. The linear region of the velocity profile is located inside $y/D < 1.0$. Hence, when taking this into consideration the free-stream velocity experienced by the cylinder is close to 1.1 m/s and the corresponding Reynolds number increases to about $Re = 110$ in the present study. Strong dependence on Re was found for root-mean-square C'_L and St in the study by Lei et al with $Re = 80$; 100; 200: The Strouhal number and root-mean-square C'_L increased with increasing Re, and for increasing Re, the critical gap for vortex shedding

decreased and correspondingly the RMS C'_L-curve was shifted to lower values of G/D. This apparent increase in Re could explain the discrepancies in St and the offset of RMS C'_L at $G/D = 1.0$ in the present study. The larger free-stream velocity also contributes to explain the larger drag experienced at $G/D = 1.0$. However, the absence of a negative lift at $G/D = 1.0$ is difficult to explain in other ways then by the flow's similarity to the unconfined condition.

Vortex shedding suppression may be related to the steepness factor κ of the velocity profile in the boundary layer. The velocity profile is approximately linear with $du/dy = 1$ at $y \lesssim 1.0$. With reference to figures 5 and 17, $U_0 = 0.7$ at $G/D = 0.2$ and $U_0 = 1.0$ at $G/D = 0.5$. Then the shear parameter κ may be obtained from equation (1.6): $\kappa = 1.42$ at $G/D = 0.2$ and $\kappa = 1$ at $G/D = 0.5$. According to Zdravkovich, the limit for vortex shedding suppression is $\kappa > 0.14$ [7, p. 467]. Hence, the vortex shedding suppression observed at $G/D = 0.2$ and $G/D = 0.5$ in the present study is in accordance with the limit reported by Zdravkovich. At $G/D = 1.0$, the cylinder is no longer exposed to a linear shear flow and this approach is not valid to assess vortex shedding. However, vortex shedding occurs in the absence of a linear shear as expected.

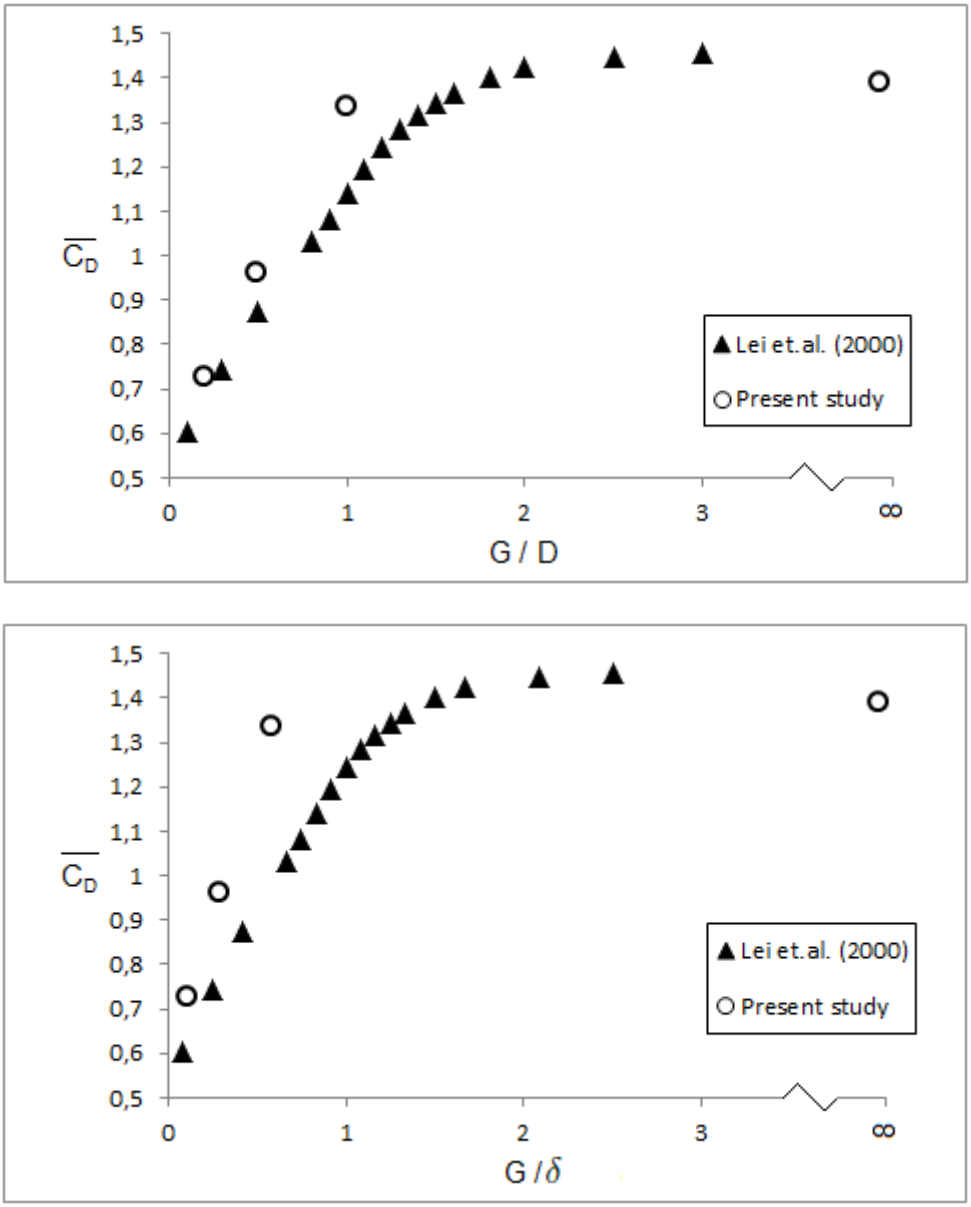

Figure 39: Mean drag coefficient for different gap ratios

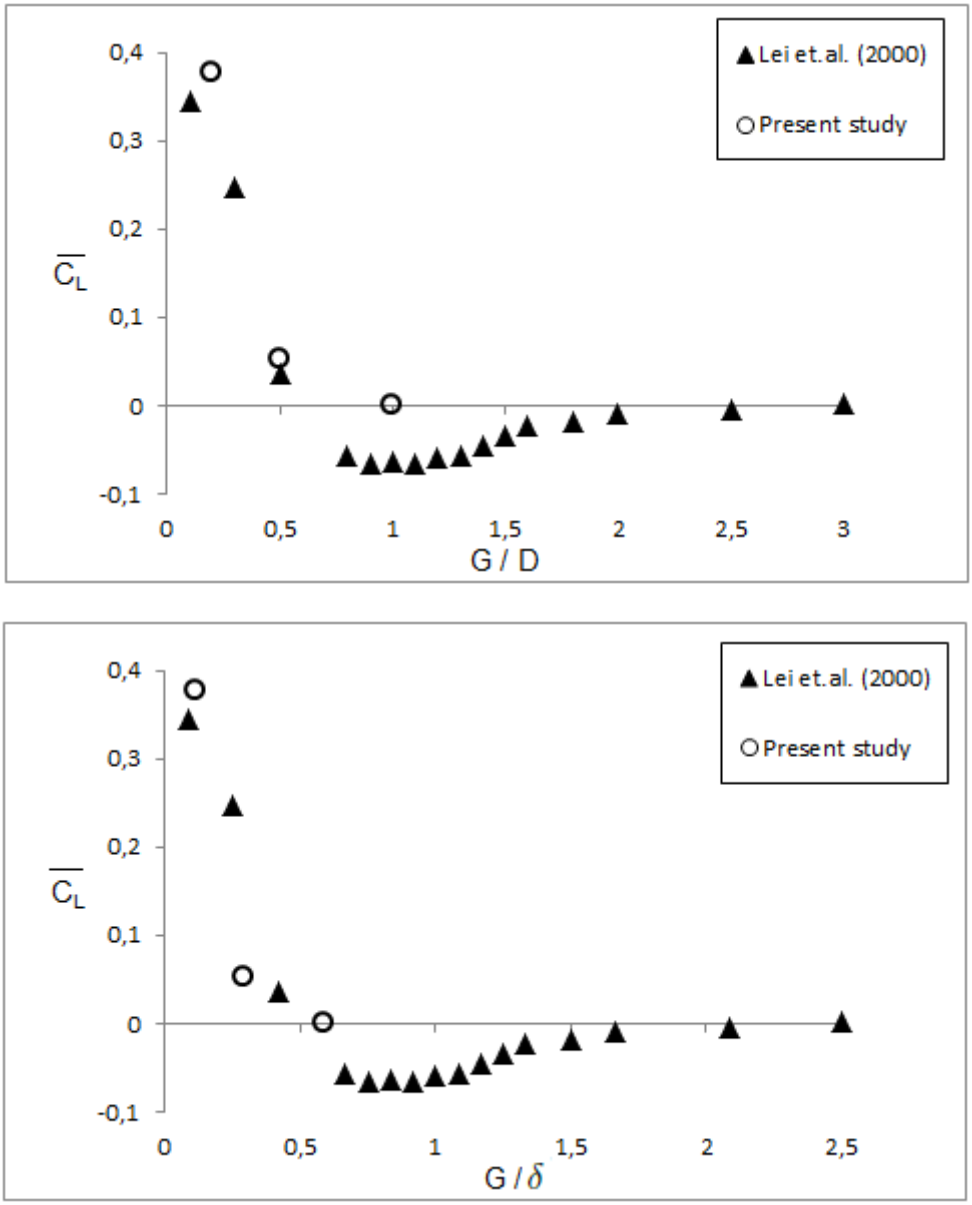

Figure 40: Mean lift coefficient for different gap ratios

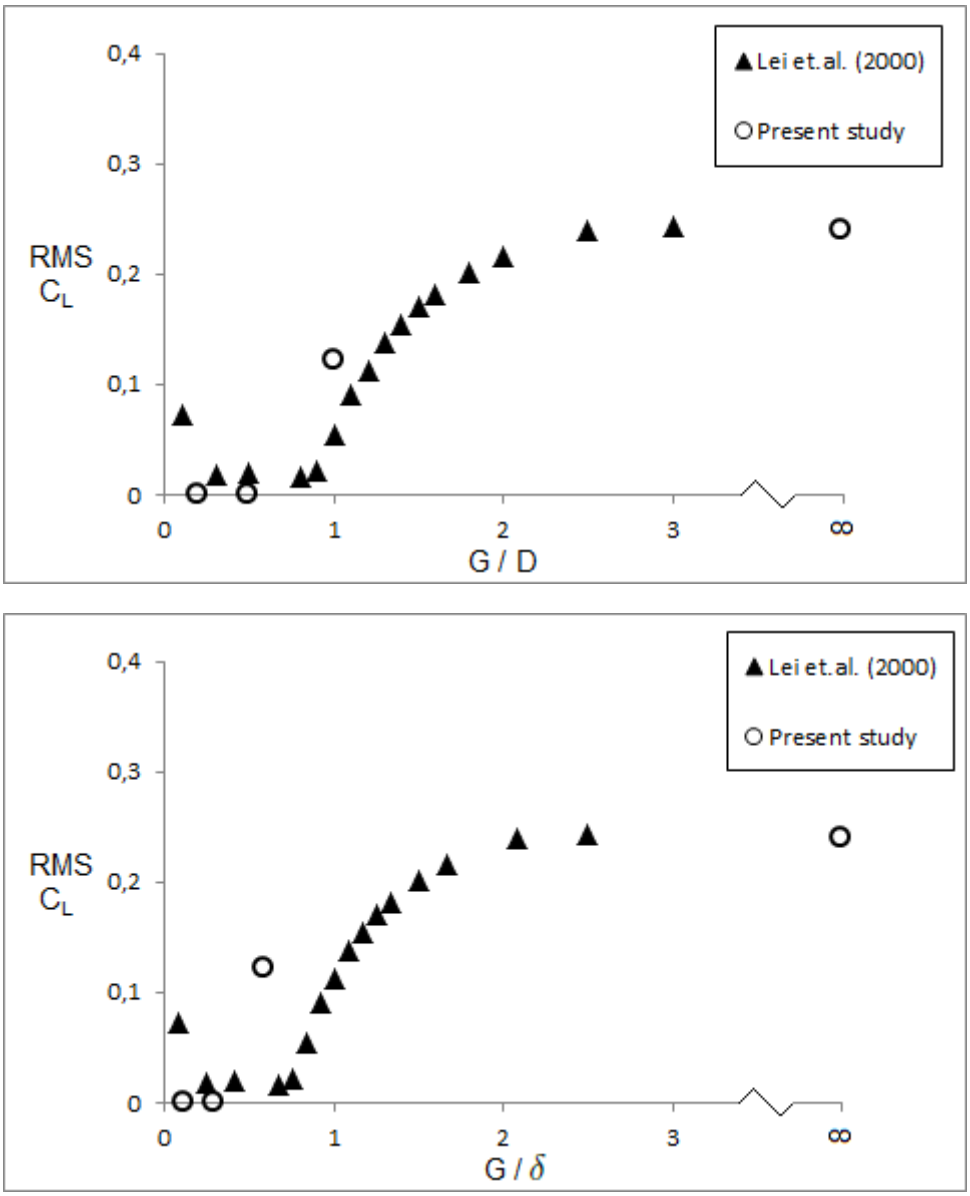

Figure 41: Root-mean-square lift coefficient for different gap ratios

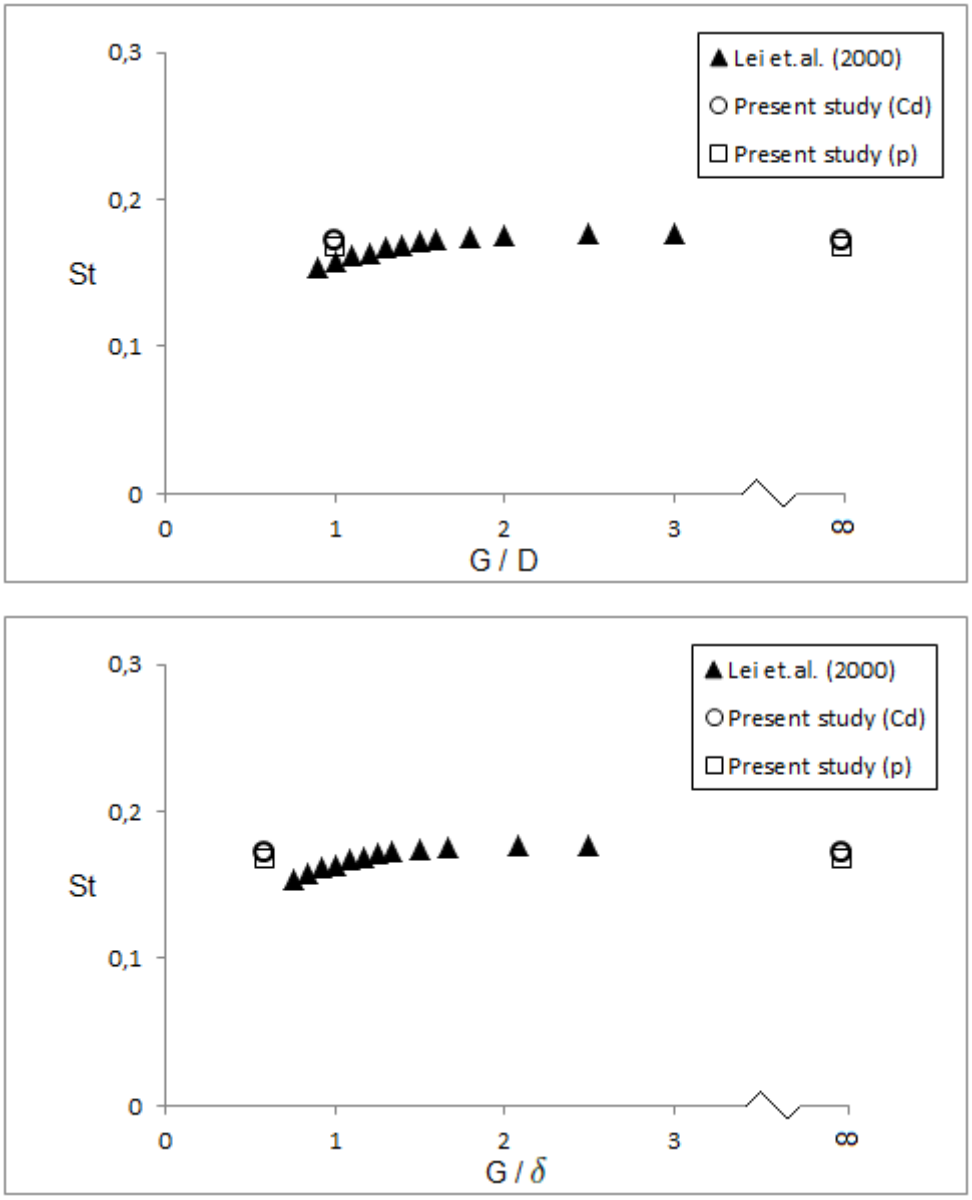

Figure 42: Strouhals number for different gap ratios

6 Flow around a circular cylinder above a fully developed scour profile

6.1 Simulation setup

The geometry of the boundary is now altered by introducing a depression below the pipeline. The geometry attempts to imitate the scour hole forming under a marine pipeline in the process of lee-wake erosion and is inspired by the scour profile in figure 7. The figure is taken from an experimental study performed at $Re = \mathcal{O}(10^4)$ where maximum scour depth $S/D \approx 1$. However, in order to ensure vortex shedding (which is the nature of this process), the depth is increased to $S/D = 2$ in the present study. In order to obtain similar slopes, the upstream and downstream extent of the scour trench is twice of that in the figure in terms of x/D. The scour profile is 'frozen' in the present study and no attempt is made to include sediment transport or to model the scour development.

2D simulations are performed at a $Re = 100$ with a cylinder diameter of $D = 1$ m, uniform inflow of $U = 1$ m/s and $\nu = 0.01$ m^2/s. The geometry of the flow configuration is sketched in figure 43 with the assigned boundary conditions. The bottom of the cylinder is in line with the horizontal parts of the wall. The parameters determining the geometry is given in table 14 and the grid parameters are given in table 15. The simulations are run from $t = 0$ to $t = 600$ sec. The 3D simulation is performed with 60 elements evenly distributed along a cylinder span of $6D$, so that $\Delta z = 0.1D$.

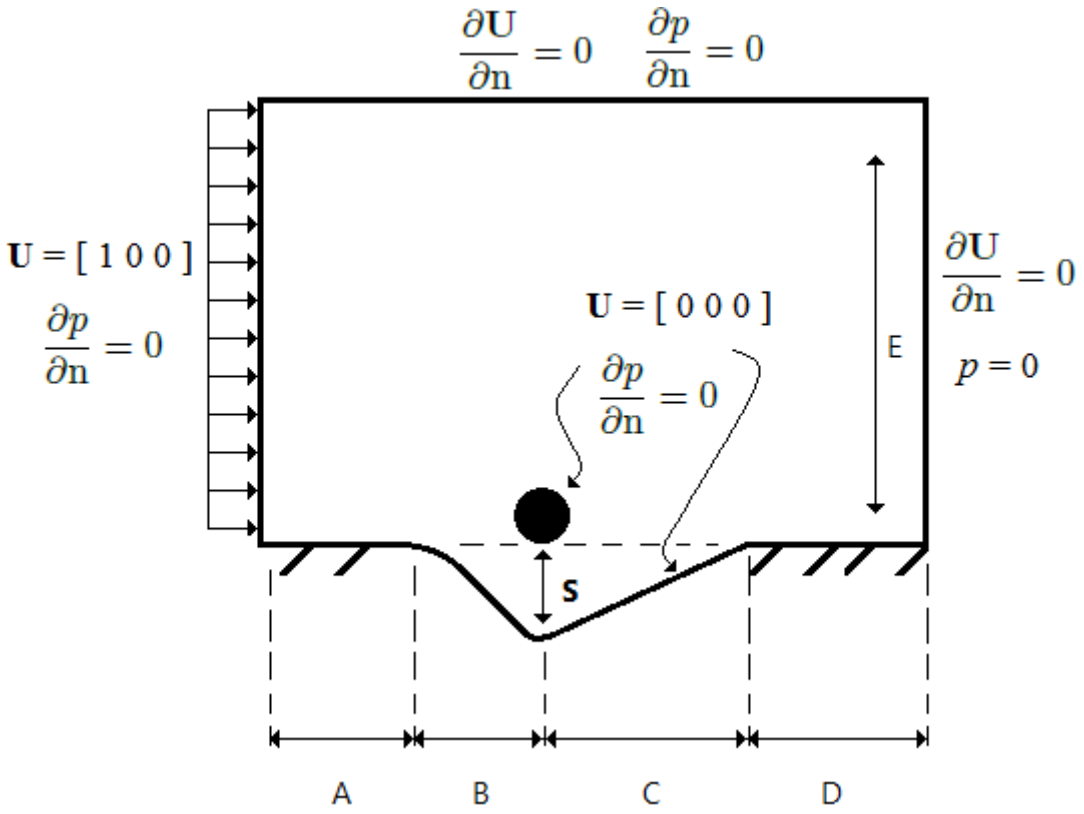

Figure 43: Problem definition for a cylinder over a scour profile

Table 14: Parameters for the geometry of a cylinder over a scour profile

A	B	C	D	E	S
9	6	12	18	20.5	2

Table 15: Grid properties for a cylinder over a scour profile

Grid	Tot number of elements	Δr radial	Δs circumfer.	Δx along plate	Δy perp. plate
Scour1 (2D)	56 325	0.055	0.013	0.090	0.050
Scour2 (2D)	86 000	0.035	0.011	0.090	0.035

6.2 Results and discussion

The results in terms of lift and drag coefficient and Strouhals number is given in table 16.

Table 16: Results for a cylinder over a scour profile

Grid	time step $\triangle$t sec	$\overline{C_D}$	$\overline{C_L}$	$\sqrt{\overline{C_L'^2}}$	St (C_L)	St (p)
Scour1 (2D)	0.001	0.787	-0.2177	0.215	0.116	0.114
Scour2 (2D)	0.001	0.791	-0.2156	0.220	0.113	0.114

The present flow configuration is characterized by periodic vortex shedding from the cylinder. The resulting values of the engineering quantities are: $\overline{C_D} = 0.79$, $\overline{C_L} = -0.22$, root-mean-square $C_L' = 0.22$ and Strouhals number St=0.114. In this case the gap ratio is $G/D = 0$ with reference to the horizontal part of the wall and the scour depth $S/D = 2.0$ below the cylinder. The results may be compared to those obtained for a cylinder located at different gap ratios above a plane wall. The value of drag in the scour case is between the values at $G/D = 0.2$; $\overline{C_D} = 0.727$ and at $G/D = 0.5$; $\overline{C_D} = 0.96$. The negative lift is unique in the present study, and by far greater than the negative lift reported by Lei et al [1] for a cylinder near a plane wall; $\overline{C_L} = \mathcal{O}(0.05)$, in the range $0.8 < G/D < 2.5$. The vortex shedding frequency in terms of St is reduced by 32% compared to the unconfined cylinder. Visualizations of the results from grid Scour2 are presented in the following.

6.2.1 Investigating grid and element properties

The influence of domain size and time step is carefully investigated in preceding sections. Hence, the applied domain and time step are assumed to be satisfactory in the present case.

Between the subsequent grids, the differences in the hydrodynamic quantities are: $\triangle$ $\overline{C_D}$ = 0.5%, $\triangle$ $\overline{C_L}$ = 1.0%, $\triangle$ $\sqrt{\overline{C_L'^2}}$ = 2.3% and no variation in St (p). Hence, the simulations fulfull the convergence criterion of maximum 3% change between subsequent grids.

Although the simulations fulfill convergence, a pressure defect is observed near the wall downstream of the cylinder. This is indicated on grid Scour2 in figure 44 where the cylinder is visible in the top right corner. The pressure defect is evident by the abrupt changes along the pressure contour. This pressure defect is located at the intersecting

grid line where the elements have different orientations across this line. Additionally, there is another intersecting grid line to the right of the pressure defect. Suggestions are that these intersecting grid lines and accompanying different element orientations are the cause of this spurious pressure. Two different approaches are applied in the present case. However, no remedy is found to avoid the pressure defect. The pressure defect is very local and although it contaminates the solution, it is considered to be of minor importance.

A similar, yet more pronounced, defect is observed in the vorticity contour lines in Appendix G.4. It is suggested to have the same origin as the pressure defect.

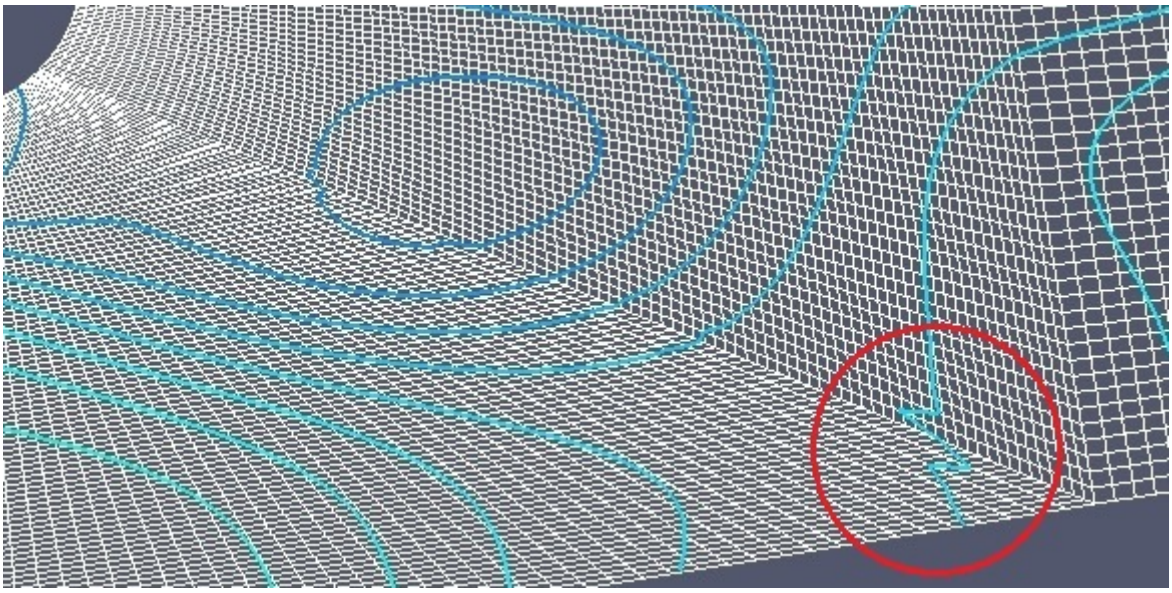

Figure 44: Pressure defect on the grid for a cylinder above a scour profile

6.2.2 Pressure distribution

The pressure distribution over one period of vortex shedding is depicted in Appendix G.1. The main characteristics of the pressure distribution over the cylinder surface persist over the entire period: the stagnation point is displaced towards the free-stream side, the region of low pressure at the free-stream side is moved downstream and the region of low pressure at the wall-side is moved upstream. Hence, the entire pressure distribution is rotated a small angle clockwise compared to the pressure distribution for an unconfined cylinder in uniform cross-flow. The altered pressure distribution and the displacement of the stagnation point contribute to a negative lift on the cylinder. Additionally, the drag is reduced due to the redistribution of total force to the lift component.

The pressure visualizations indicate two sided vortex shedding. Downstream of the cylinder a row of alternately high and low pressure regions originating from the free-stream side of the cylinder is visible. The alternating pressure regions originating from the wall-side of the cylinder are less distinct. This behavior in particular is similar to the cylinder positioned at $G/D = 1.0$ above a plane wall in the preceding section. A local pressure peak is observed at all times in the through of the scour trench. The visualizations of the pressure indicate alternating vortex shedding from both sides of the cylinder. However, the eddies originating at the free-stream side seems to be stronger.

With reference to Jensen et al. [35], the results for the cylinder located above an equilibrium scour profile in the present study at $Re = 100$ exhibits some similar features

as the flow at $Re = 10^4$. In particular, the stagnation point at the cylinder is moved away from the wall and distint negative mean lift are observed in both studies. Additionally, the drag is reduced as compared to the cylinder located at a similar gap above a plane boundary.

6.2.3 Velocity field

Visualizations of the velocity field with reference to magnitude of velocity (scalar) is presented in figures 45 and 46 by time series over one period of vortex shedding. The near wake of the cylinder exhibits a periodic wavy shape and the figures indicate one sided periodic vortex shedding. Persistent high velocity is observed in a small region in the close proximity of the cylinder's underside at all times. A dominant gap flow of 0.6-0.8 m/s is observed below the cylinder. A distinct region of low velocity is located near the wall upstream of and below the cylinder. Vector plots (Appendix G.2) of the velocities are utilized to further investigate this region, revealing a region of separating flow at the upstream shoulder accompanied by a region of recirculating flow. This is an expected behavior as the sudden declining wall acts similar to a classic backward facing step. Periodicity in the velocity field is evident along the inclined wall downstream of the cylinder. This region clearly interacts with the cylinder wake: sheets of low velocity are shed from the wake ($t = 581; 582.5$ sec), convected downstream ($t = 584$ sec) and entrapped in the wall region ($t = 585.5; 587; 588.5$ sec).

The dynamics of the wake is further investigated utilizing vector plots (Appendix G.3) of the velocities in this region. At the instant $t = 581$ sec two vortices are present in the near wake: one large vortex at the wall-side and one smaller at the free-stream side. Onwards from $t = 581$ sec the wake expands downstream as the vortex near the free-stream side unfolds. At $t = 588.5$ a vortex is shed from the free-stream side.

6.2.4 Vorticity

Vorticity contours are presented in Appendix G.4 over one period of vortex shedding. At $t = 581$ sec, the previous vortex shed at the freeestream side is still evident downstream. Two regions of vorticity are originating at the cylinder and three narrow regions are evident at the wall in the scour trench. As time elapses, a new vortex is shed from the free-stream side of the cylinder. Simultaneously the wall-side region of vorticity is stretched, but no vortex shedding is evident in this region. The figures also indicate some interaction between the shed vortex and the vorticity along the wall: As the shed vortex is convected downstream the regions of vorticity at the wall migrates downstream, although at a slower pace. The illustrations of periodic vorticity suggest only one sided vortex shedding, originating at the free-stream side of the cylinder.

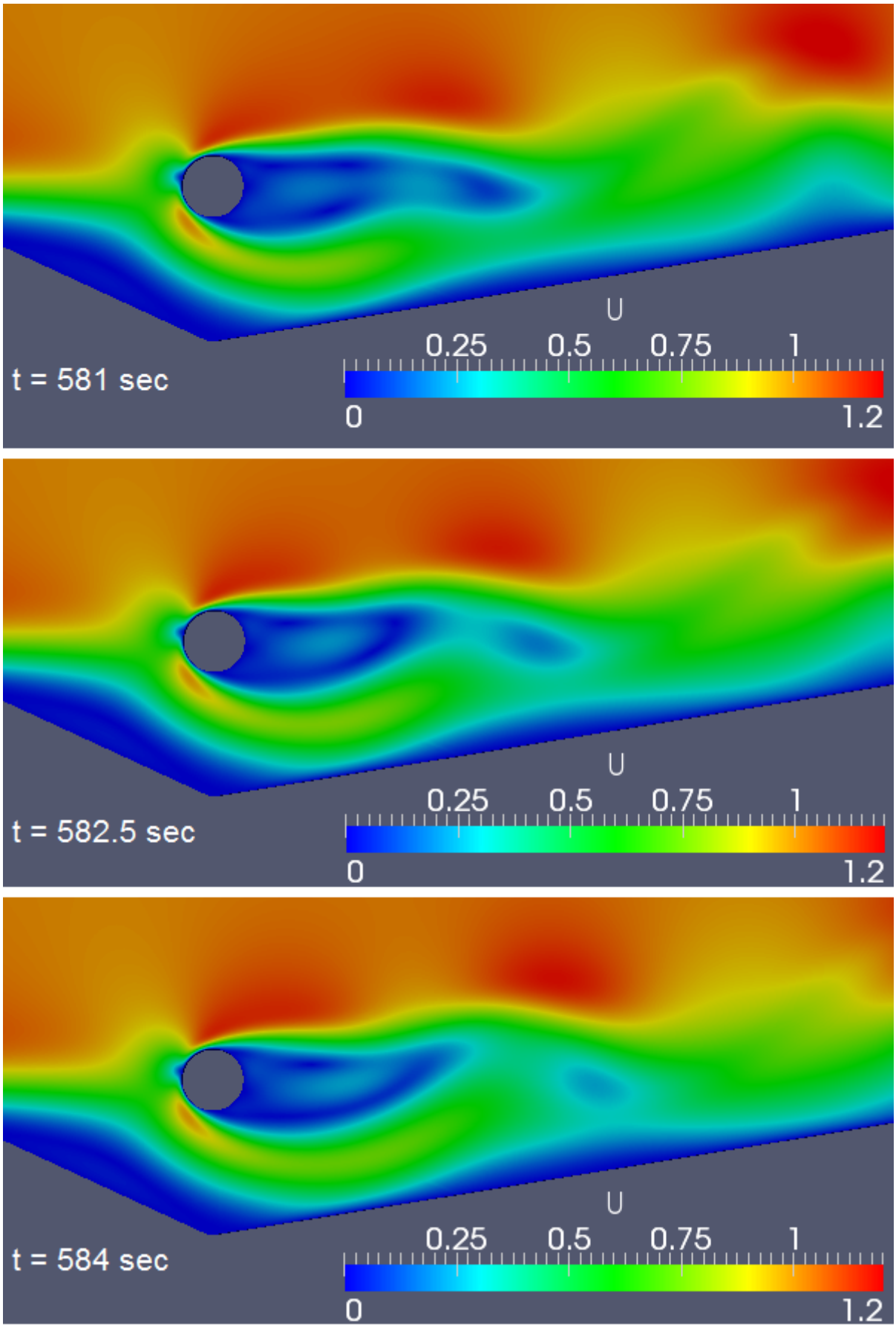

Figure 45: Magnitude of velocity (scalar) near a cylinder over a scour profile (Part 1 of 2)

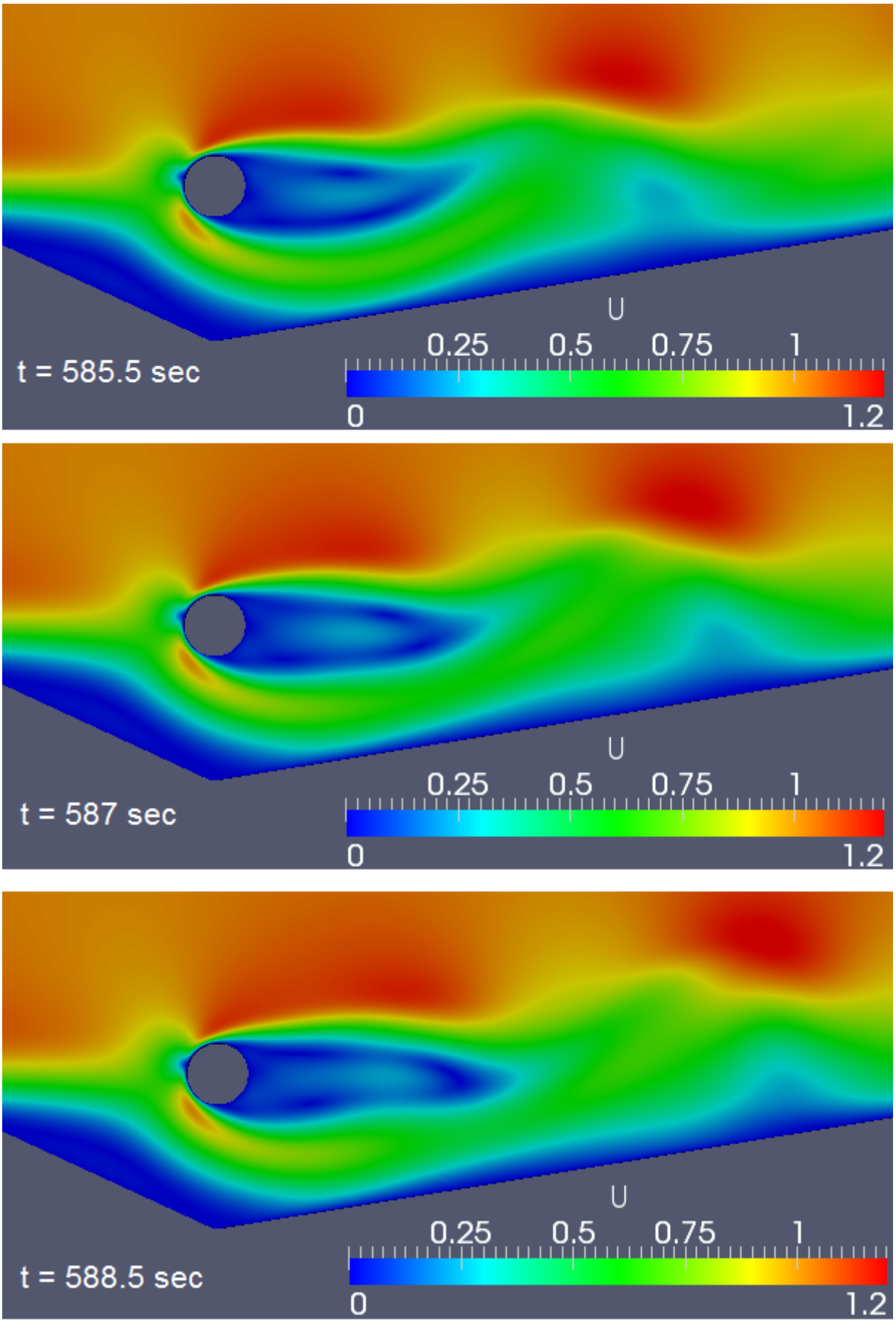

Figure 46: Magnitude of velocity (scalar) near a cylinder over a scour profile (Part 2 of 2)

7 Concluding remarks

7.1 Conclusion

Numerical simulations are performed with the software OpenFOAM for the purpose of investigating the viscous flow around a circular cylinder near a plane wall at $Re = 100$. Three different gap ratios: $G/D = 0.2; 0.5; 1.0$ are applied. Additional simulations are performed for a cylinder located above a fully developed scour profile.

Vortex shedding is suppressed for $G/D = 0.2$ and $G/D = 0.5$. This is in accordance with the results reported by Lei et al [1] and with Zdravkovich reporting the suppression of vortex shedding in steep linear shear flows which in the present study is found in the boundary layer developing at the wall.

The results are supportive to the suggestion by Grass et al. [22] that suppression of vortex shedding is caused by the interaction between the lee-side recirculating flow and the gap flow, which inhibits large-scale vortex roll-up. Additionally, the results at $G/D = 1.0$ are in accordance with suggestions in the literature [1, 26, 22], indicating cancellation of opposite signed vorticity in the near-wall region.

The main results are: $\overline{C_D}$ decreases with decreasing gap, $\overline{C_L}$ increases with decreasing gap and a distinct mean lift, $\overline{C_L}$, is observed in the direction away from the wall at $G/D = 0.5$ and $G/D = 0.2$. No change in St is observed as long as vortex shedding occurs. The results are supportive to Lei et al [1] suggesting root-mean-square C'_L as an indicator for vortex shedding suppression. Generally, the obtained values at $G/D = 0.2$ and $G/D = 0.5$ display good agreement with the results of Lei et al [1]. However, the results at $G/D = 1.0$ differs somewhat from their results.

The introduction of a fully developed scour profile below the cylinder significantly alters the flow and periodic vortex shedding occurs. Time series of the pressure indicate two-sided vortex shedding, while time series of velocity and vorticity indicate one-sided vortex shedding originating at the free-stream side of the cylinder. These seemingly contradictory results suggest that further investigations should be performed. The main results are $\overline{C_D} = 0.79$, a substantial mean lift, $\overline{C_L} = -0.22$, in the direction towards the wall and St $= 0.114$ which is 32% lower than for the unconfined cylinder. Similarity is observed between the present results and experimental data at $Re = 1000$. The results from these simulations are the main contributions of the present study.

The resulting values for 2D simulations of an unconfined cylinder in uniform cross-flow are $\overline{C_D} = 1.39$, root-mean-square $C_L = 0.24$ and St $= 0.168$. These results are within the scatter of the reported values in the literature. However, they differ by 2-6% from the standard benchmark values.

The influences on the 2D simulations are investigated in terms of convergence studies of $\overline{C_D}$, $\overline{C_L}$, $\sqrt{\overline{C'^2_L}}$ and St for the key numerical parameters: domain size, grid geometry, element size, element spacing and time step.

The influence of time step is thoroughly investigated for the unconfined cylinder and the results indicate independence of time step as long as the CFL-condition is fulfilled. However, this investigation suffers from the use of only one domain size.

The influence of domain size is investigated for the unconfined cylinder and the cylinder at distance $G/D = 0.2$ from a plane wall. The applied domains are satisfactory with reference to these investigations. However, a drawback to this investigation is the use of only one time step.

The element size and element spacing is investigated for the unconfined cylinder, for the cylinder at every gap ratio near the plane wall and for the cylinder over a scour profile. The investigations are satisfactory, except for the value of $\sqrt{\overline{C_L'^2}}$ at $G/D = 1.0$. Hence, additional simulations are desirable at this gap ratio. Additionally, a local defect is observed in the pressure for the cylinder at $G/D = 0.5$ and for the cylinder above the scour profile, these defects are attributed to a shortcoming in the grid design. Further investigations should be performed to assess the influence of these defects and to remedy this behavior.

Further, 3D simulations are performed for the unconfined cylinder and the cylinder at a distance $G/D = 0.5$ from a plane wall. Insignificant differences in the results were found between 2D and 3D simulations. This is presumably due to the two-dimensional behavior of the flow at this Reynolds number.

7.2 Recommendations for further work

This study investigates 2D simulations of an unconfined cylinder and a cylinder at different gap ratios to a plane wall. Further, 3D simulations of a cylinder near a plane wall are demonstrated as well as 2D simulations of a cylinder over a fully developed scour profile.

Additional 2D and 3D simulations should be performed in order to verify the results of Lei et al. [1] and the present results; particularly at $G/D = 1.0$. Specifically it is of interest to investigate the occurrence of a negative mean lift and the critical gap ratio for vortex shedding suppression as reported by Lei et al. Additionally, it is of interest to further investigate the shape of the mean drag curve and the possible existence of a peak at larger gap ratios $G/D > 1.0$ and the development of the root-mean-square lift coefficient at very small gaps $G/D < 0.2$.

The grid should be further improved for a cylinder above a scour profile to avoid any defects in the pressure distribution. Additional simulations, both 2D and 3D, should be performed at different stages in the scour process and with the cylinder at different positions relative to the scour profile. Further, the model should be improved by taking into account the calculation of sediment transport and the development of scour.

References

[1] C. Lei, L. Cheng, S. W. Armfield, and K. Kavanagh, "Vortex shedding suppression for flow over a circular cylinder near a plane boundary," *Ocean Engineering*, vol. 27, pp. 1109–1127, 2000.

[2] M. C. Ong, *Applications of a Standard High Reynolds Number $k - \epsilon$ Model and a Stochastic Scour Prediction Model for Marine Structures*. PhD thesis, Norwegian University of Science and Technology, 2009.

[3] M. Jakobsen, L. Egelund, and H. Hovdan, *Nedbrytning av rørledninger over tid, Prosjekt no: 36661.001 (in Norwegian)*. The Norwegian Ministry of Petroleum and Energy, 1998.

[4] *Facts, The Norwegian Petroleum Sector 2010*. Norwegian Ministry of Petroleum and Energy and the Norwegian Petroleum Directorate, 2010.

[5] B. M. Sumer and J. Fredsøe, *The Mechanics of Scour in the Marine Environment*. World Scientific Publishing Co. Pte. Ltd., 2002.

[6] *Statistisk årbok 2010 (in Norwegian)*. Statistics Norway (SSB), 2010.

[7] M. M. Zdravkovich, *Flow Around Circular Cylinders, Vol 1: Fundamentals*. Oxford University Press Inc, 1997.

[8] C. H. K. Williamson, "Three-dimensional wake transition," *Journal of Fluid Mechanics*, vol. 328, pp. 345–407, 1996.

[9] B. M. Sumer and J. Fredsøe, *Hydrodynamics Around Cylindrical Structures*. World Scientific Publishing Co. Pte. Ltd., 1997.

[10] C. Norberg, "Fluctuating lift on a circular cylinder: review and new measurements," *Journal of Fluids and Structures*, vol. 17, pp. 57–96, 2003.

[11] O. M. Faltinsen, *Sea Loads on Ships and Offshore Structures*. Cambridge University Press, 1990.

[12] D. J. Tritton, "Experiments on the flow past a circular cylinder at low reynolds number," *Journal of Fluid Mechanics*, vol. 6, pp. 547–567, 1959.

[13] M. A. Cruchaga, N. M. Nigro, M. A. Storti, and D. J. Celentino, "Computing past cylinder flows," *Mecnica Computacional*, vol. XXI, pp. 462–475, 2002.

[14] R. D. Henderson, "Details of the drag curve near the onset of vortex shedding," *Physics of Fluids*, vol. 7, pp. 2102–2104, 1995.

[15] C. H. K. Williamson, "Oblique and parallel modes of vortex shedding in the wake of a circular cylinder at low reynolds number," *Journal of Fluid Mechanics*, vol. 206, pp. 579–627, 1989.

[16] H. Cao and D. Wan, "Application of openfoam to simulate three-dimensional flows past a single and two tandem circular cylinders," *Proceedings of the Twentieth (2010) International Offshore and Polar Engineering Conference - ISOPE*, pp. 702–709, 2010.

[17] K. K. Heggernes, *Numerical simulation of three-dimensional viscous flow around marine structures*. PhD thesis, Norwegian University of Science and Technology, 2005.

[18] S. Sarkar and S. S., "Vortex dynamics of a cylinder wake in proximity to a wall," *Journal of Fluids and Structures*, vol. 26, pp. 19–40, 2010.

[19] M. M. Zdravkovich, *Flow Around Circular Cylinders, Vol 2: Applications*. Oxford University Press Inc, 2003.

[20] S. Taneda, "Experimental investigation of vortex streets," *Journal of the Physical Society of Japan*, vol. 20, pp. 1714–1721, 1965.

[21] P. W. Bearman and M. M. Zdravkovich, "Flow around a circular cylinder near a plane boundary," *Journal of Fluid Mechanics*, vol. 89, pp. 33–47, 1978.

[22] A. J. Grass, P. W. J. Raven, R. J. Stuart, and J. A. Bray, "The influence of boundary layer velocity gradients and bed proximity on vortex shedding from free spanning pipelines," *Journal of Energy Resources Technology*, vol. 106, pp. 70–78, 1984.

[23] G. Buresti and A. Lanciotti, "Mean and fluctuating forces on a circular cylinder in cross-flow near a plane surface," *Journal of Wind Engineering and Industrial Aerodynamics*, vol. 41, pp. 639–650, 1992.

[24] C. Lei, L. Cheng, and K. Kavanagh, "Re-examination of the effect of a plane boundary on force and vortex shedding of a circular cylinder," *Journal of Wind Engineering and Industrial Aerodynamics*, vol. 80, pp. 263–286, 1999.

[25] X. K. Wang and S. K. Tan, "Near-wake flow characteristics of a circular cylinder close to a wall," *Journal of Fluids and Structures*, vol. 24, pp. 605–627, 2008.

[26] S. Taniguchi and K. Miyakoshi, "Fluctuating fluid forces acting on a circular cylinder and interference with a plane wall," *Experiments in Fluids*, vol. 9, pp. 197–204, 1990.

[27] M. M. Zdravkovich, "Forces on a circular cylinder near a plane wall," *Applied Ocean Research*, vol. 7, pp. 197–201, 1985.

[28] W.-J. Lin, C. Lin, S.-C. Hsieh, and S. Dey, "Flow characteristics around a circular cylinder placed horizontally above a plane boundary," *Journal of Engineering Mechanics*, vol. 135, pp. 697–715, 2009.

[29] S. J. Price, D. Sumner, J. G. Smith, K. Leong, and M. P. Paidoussis, "Flow visualization around a circular cylinder near to a plane wall," *Journal of Fluids and Structures*, vol. 16, pp. 175–191, 2002.

[30] P. Nielsen, *Coastal Bottom Boundary Layers and Sediment Transport*. World Scientific Publishing Co. Pte. Ltd., 1992.

[31] O. H. Slaatelid, D. Myrhaug, and K. F. Lambrakos, "North sea steady boundary layer measurments," *Journal of Waterway, Port, Coastal and Ocean Engineering*, vol. 116, pp. 614–633, 1990.

[32] W. Schumann, *Norsk steinhåndbok (in Norwegian)*. H. Aschehoug & Co, 2000.

[33] *Recommended Practice, DNV-RP-F109 On-bottom Stability Design of Submarine Pipelines.* Det norske Veritas (DNV), 2007.

[34] L. Cheng, K. Yeow, Z. Zhang, and B. Teng, "Three-dimensional scour below offshore pipelines in steady currents," *Coastal Engineering*, vol. 56, pp. 577–590, 2009.

[35] B. L. Jensen, B. M. Sumer, H. R. Jensen, and J. Fredsø e, "Flow around and forces on a pipeline near a scoured bed in steady current," *ASME Journal of Offshore Mechanics and Arctic Engineering*, vol. 112, pp. 206–213, 1990.

[36] B. M. Sumer, "Mathematical modelling of scour: A review," *Journal of Hydraulic Research*, vol. 45, pp. 723–735, 2007.

[37] B. Brørs, "Numerical modeling of flow and scour at pipelines," *Journal of Hydraulic Engineering*, vol. 125, pp. 511–523, 1999.

[38] D. Liang, L. Cheng, and F. Li, "Numerical modelling of flow and scour below a pipeline in currents part ii: Scour simulations," *Coastal Engineering*, vol. 52, pp. 43–62, 2005.

[39] A. Yeganeh-Bakhtiary, M. H. Kazeminezhad, A. Etemad-Shahidi, J. H. Baas, and L. Cheng, "Euler-euler two-phase flow simulation of tunnel erosion beneath marine pipelines," *Applied Ocean Research*, vol. 33, pp. 137–146, 2011.

[40] F. M. White, *Viscous Fluid Flow, 3rd ed.* McGraw-Hill, 2006.

[41] R. I. Issa, "Solution of the implicitly discretised fluid flow equations by operator-splitting," *Journal of Computational Physics*, vol. 62, pp. 40–65, 1985.

[42] F. M. White, *Fluid Mechanics, Sixth ed.* McGraw-Hill, 2008.

[43] *OpenFOAM User Guide http://www.openfoam.com/docs/user/.* OpenCFD Ltd.

[44] *OpenFOAM Features http://www.openfoam.com/features/.* OpenCFD Ltd.

[45] H. K. Versteeg and W. Malalasekera, *An introduction to Computational Fluid Dynamics The Finite Volume Method.* Longman Scientific & Technical, 1995.

[46] H. Jasak, *Error Analysis and Estimation for the Finite Volume Method with Applications to Fluid Flows.* PhD thesis, Imperial College of Science, Technology & Medicine, 1996.

[47] H. Rusche, *Computational Fluid Dynamics of Dispersed Two-Phase Flows at High Phase Fractions.* PhD thesis, Imperial College of Science, Technology & Medicine, 2002.

[48] *OpenFOAM C++ Source Guide http://www.openfoam.com/docs/cpp/.* OpenCFD Ltd.

[49] *Matlab R2010a Product Help.* The MathWorks.

[50] J. H. Ferziger and M. Peric, *Computational Methods for Fluid Dynamics 2n ed.* Springer Verlag, 1999.

[51] C. Lei, L. Cheng, and K. Kavangh, "Spanwise length effects on three-dimensional modelling of flow over a circular cylinder," *Computer methods in applied mechanics and engineering*, vol. 190, pp. 2909–2923, 2001.

[52] C. Lei. Personal communication, 2011.

List of Figures

List of Tables

Appendix A

An OpenFOAM `controlDict`-file

```
/*--------------------------------*- C++ -*----------------------------------*\
| =========                 |                                                 |
| \\      /  F ield         | OpenFOAM: The Open Source CFD Toolbox           |
|  \\    /   O peration     | Version:  1.7.1                                 |
|   \\  /    A nd           | Web:      www.OpenFOAM.com                      |
|    \\/     M anipulation  |                                                 |
\*---------------------------------------------------------------------------*/
FoamFile
{
    version     2.0;
    format      ascii;
    class       dictionary;
    location    "system";
    object      controlDict;
}
// * * * * * * * * * * * * * * * * * * * * * * * * * * * * * * * * * * * * * //

application     icoFoam;

startFrom       startTime;

startTime       0;

stopAt          endTime;

endTime         600;

deltaT          0.001;

writeControl    timeStep;

writeInterval   100;

purgeWrite      0;

writeFormat     ascii;

writePrecision  6;

writeCompression compressed;

timeFormat      general;

timePrecision   6;

runTimeModifiable yes;

functions
(probes
   {
       type            probes;
       functionObjectLibs ("libsampling.so");
       enabled         true;
       outputControl   timeStep;
       outputInterval  1;
       probeLocations
       (
               (0.6 0.2 0)
       );

       fields
       (
           p U
       );
   }


forces
{
type forces;
functionObjectLibs ("libforces.so");
patches (cylinder);
```

```
rhoName rhoInf;
rhoInf 1;
CofR (0 0 0);
outputControl timeStep;
outputInterval 10;
}

forceCoeffs
{
type forceCoeffs;
functionObjectLibs ("libforces.so");
patches (cylinder);
rhoName rhoInf;
rhoInf 1;
CofR (0 0 0);
liftDir (0 1 0);
dragDir (1 0 0);
pitchAxis (0 0 0);
magUInf 1;
lRef 1;
Aref 0.1;
outputControl timeStep;
outputInterval 10;
}

 );
// ************************************************************************* //
```

Appendix B

Matlab script for Fast Fourier Transform (FFT)

```
A=importdata('forceCoeffs.txt');      % ('p.txt')
time=A(:,1);
cD=A(:,2);                            % p=A(:,2);
cL=A(:,3);

duration=length(tid);

tmp=0;

for i=1:duration

    if time(i)>=150                   %Start time for analysis
        tmp=tmp+1;
    end


end

lift=zeros(tmp,1);

for j=1:tmp
    lift(j)=cL(j+duration-tmp);       % Change: cL / cD / p
end

%%% Fourier transform: spectral analysis %%%
% Based on example in Matlab Help
fs=100;                           % Dependent on delta t. Pressure: fs=1000
m=length(lift);
n=2^nextpow2(m);
y=fft(lift,n);
f=(0:(n-1))*(fs/n);
power=log(y.*conj(y)/n);
plot(f,power)
xlabel('Frequency (Hz)')
ylabel('Power')
title('{\bf Periodogram}')
```

Appendix C

Visualizations of the flow around a circular cylinder in uniform cross-flow

Appendix C.1: Pressure distribution

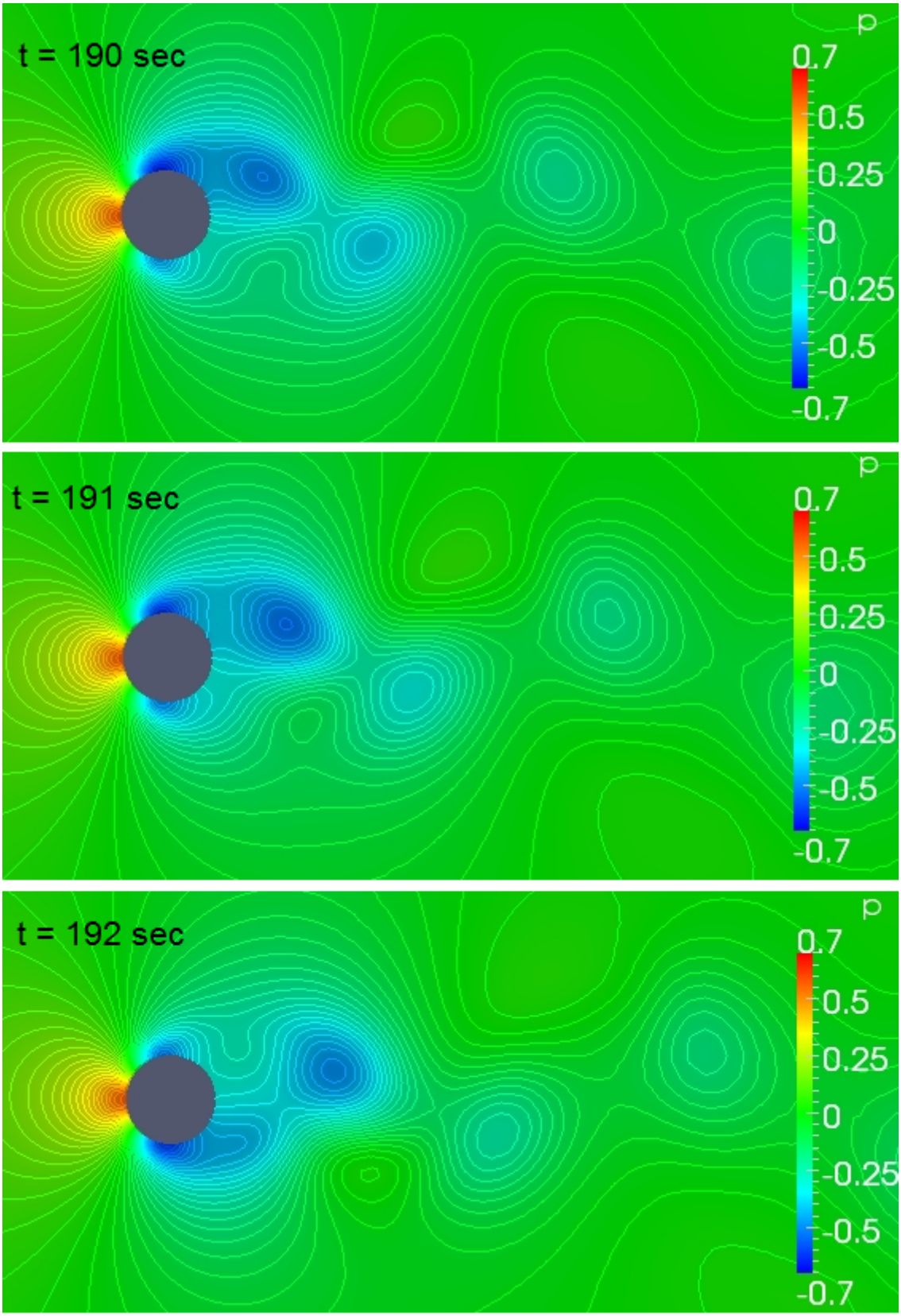

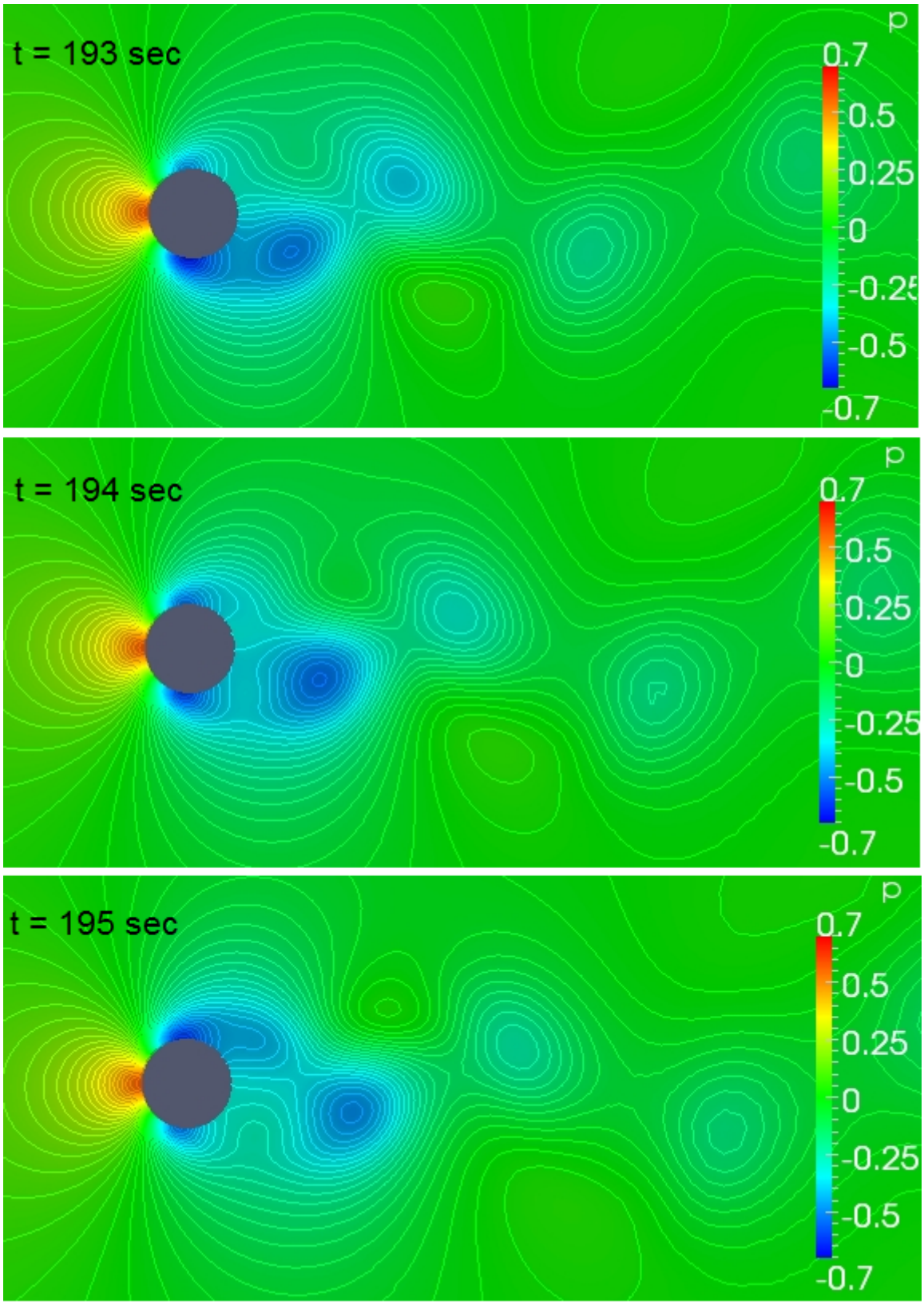
t = 193 sec
p
0.7
0.5
0.25
0
-0.25
-0.5
-0.7
t = 194 sec
p
0.7
0.5
0.25
0
-0.25
-0.5
-0.7
t = 195 sec
p
0.7
0.5
0.25
0
-0.25
-0.5
-0.7

Appendix C.2: Velocity field

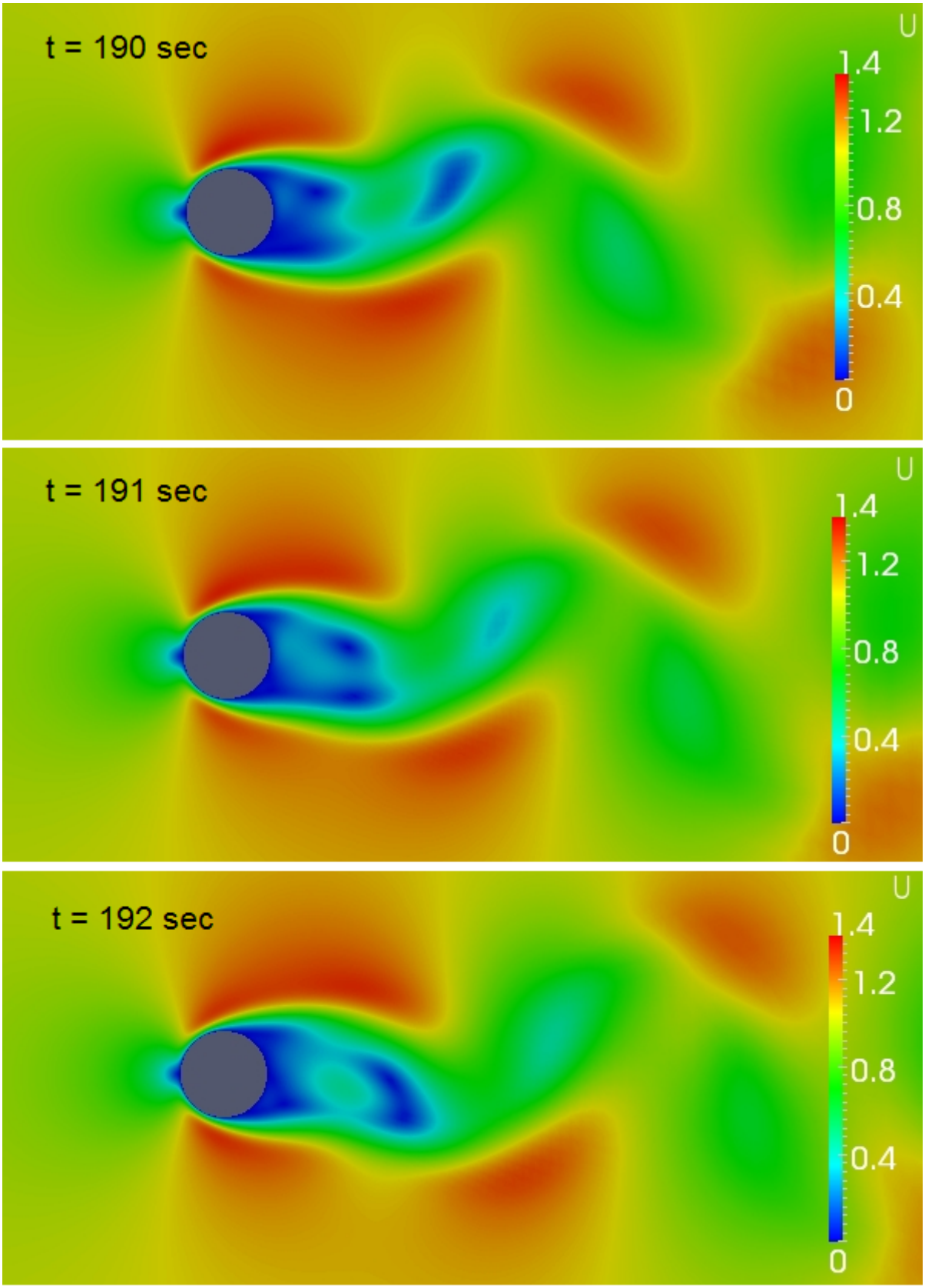

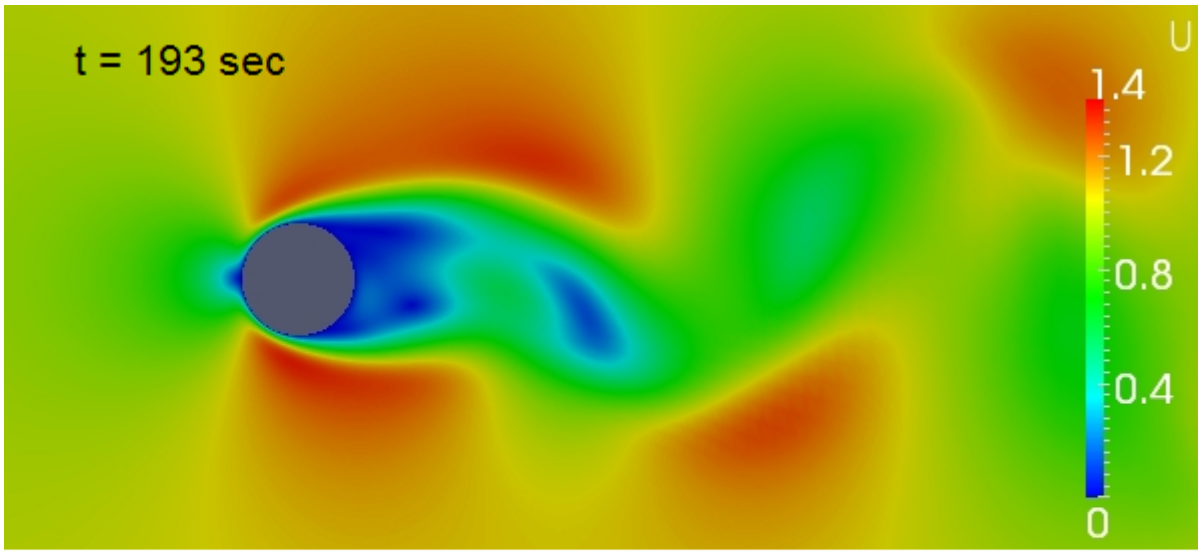
t = 193 sec
U
1.4
1.2
0.8
0.4
0

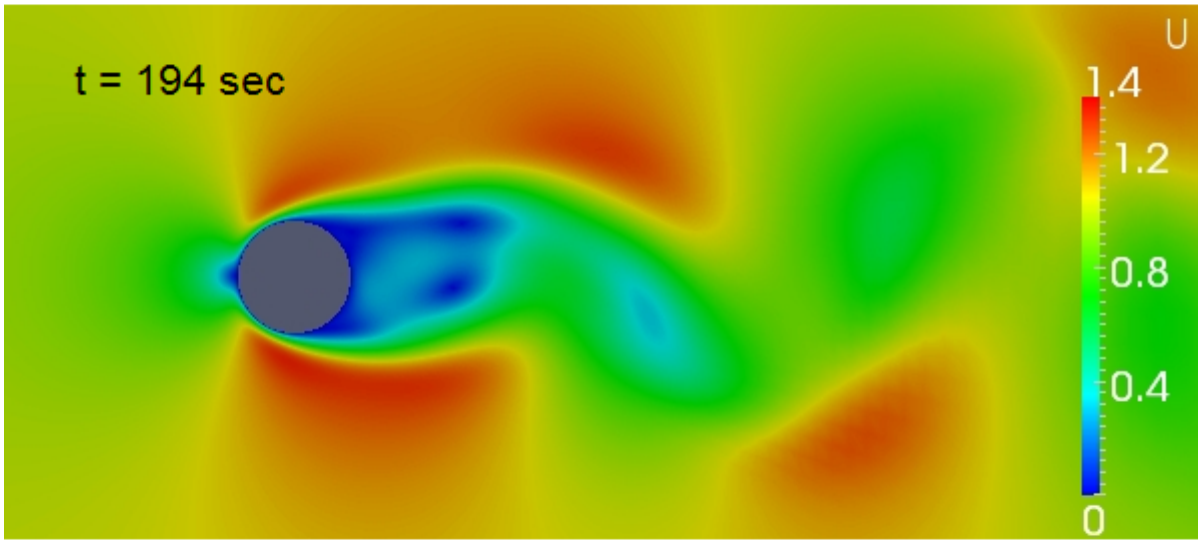
t = 194 sec
U
1.4
1.2
0.8
0.4
0

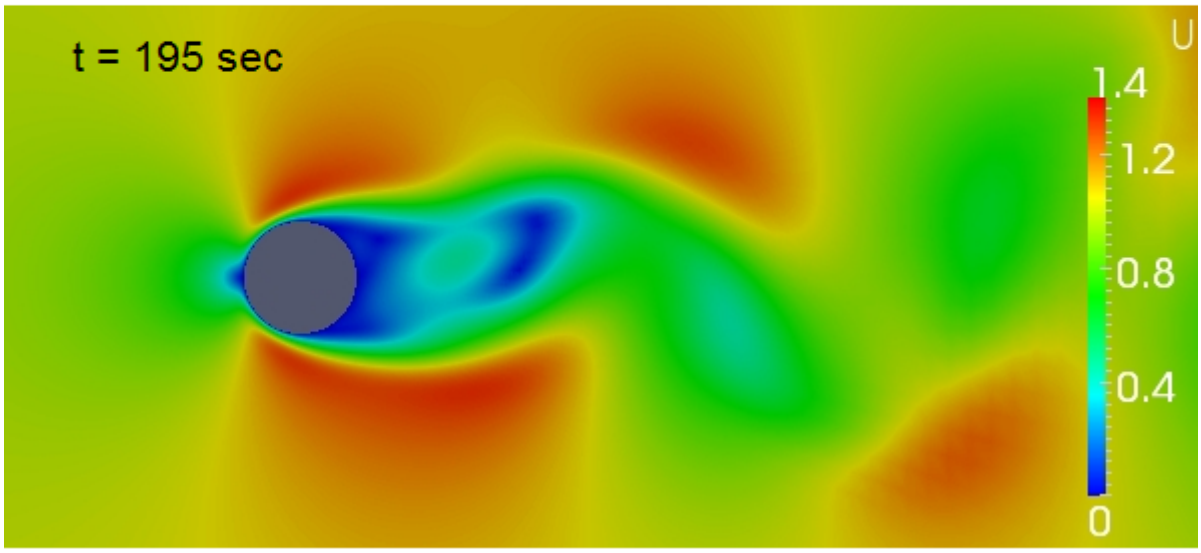
t = 195 sec
U
1.4
1.2
0.8
0.4
0

Appendix C.3: Vorticity contours ω_z

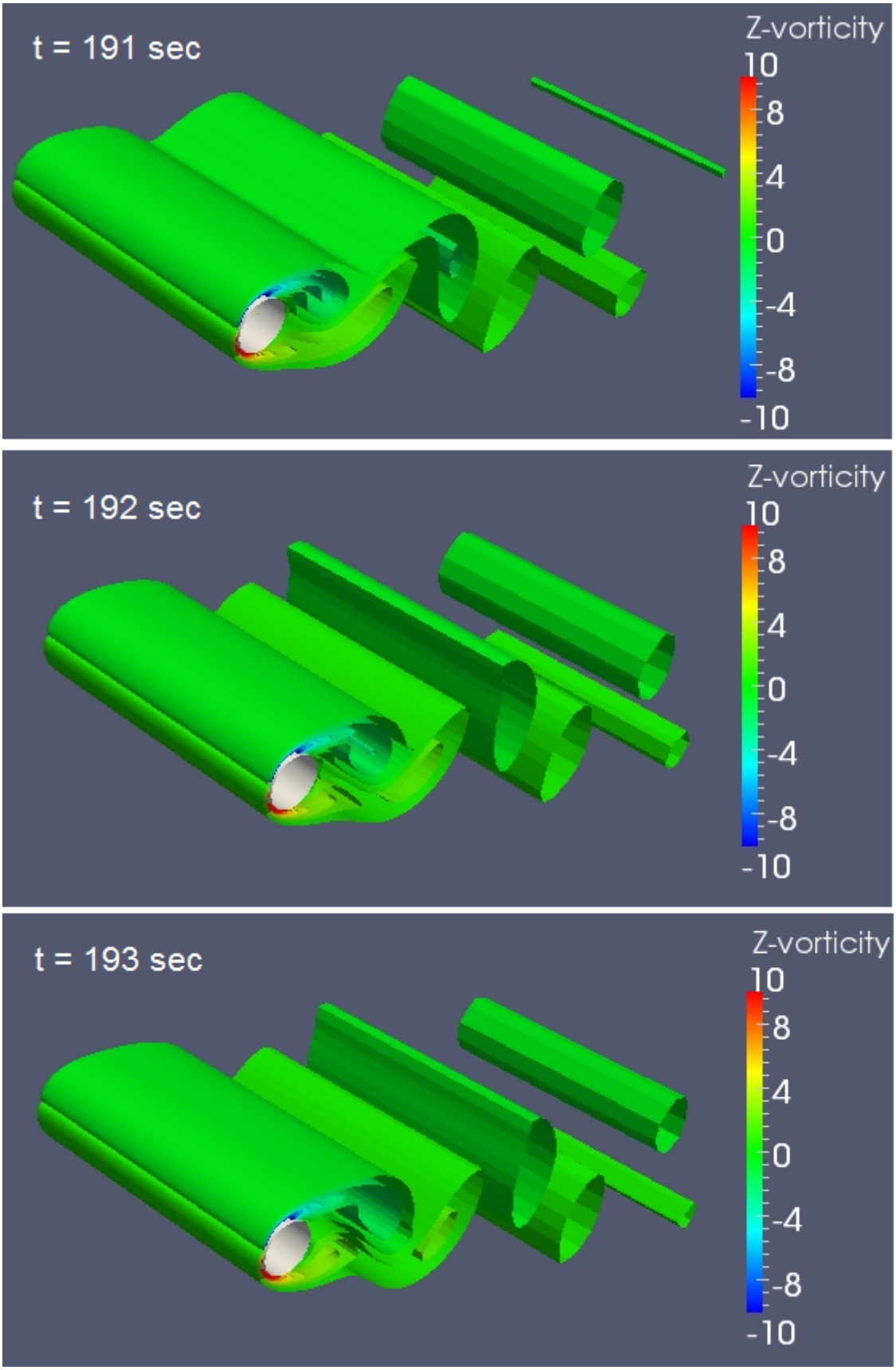

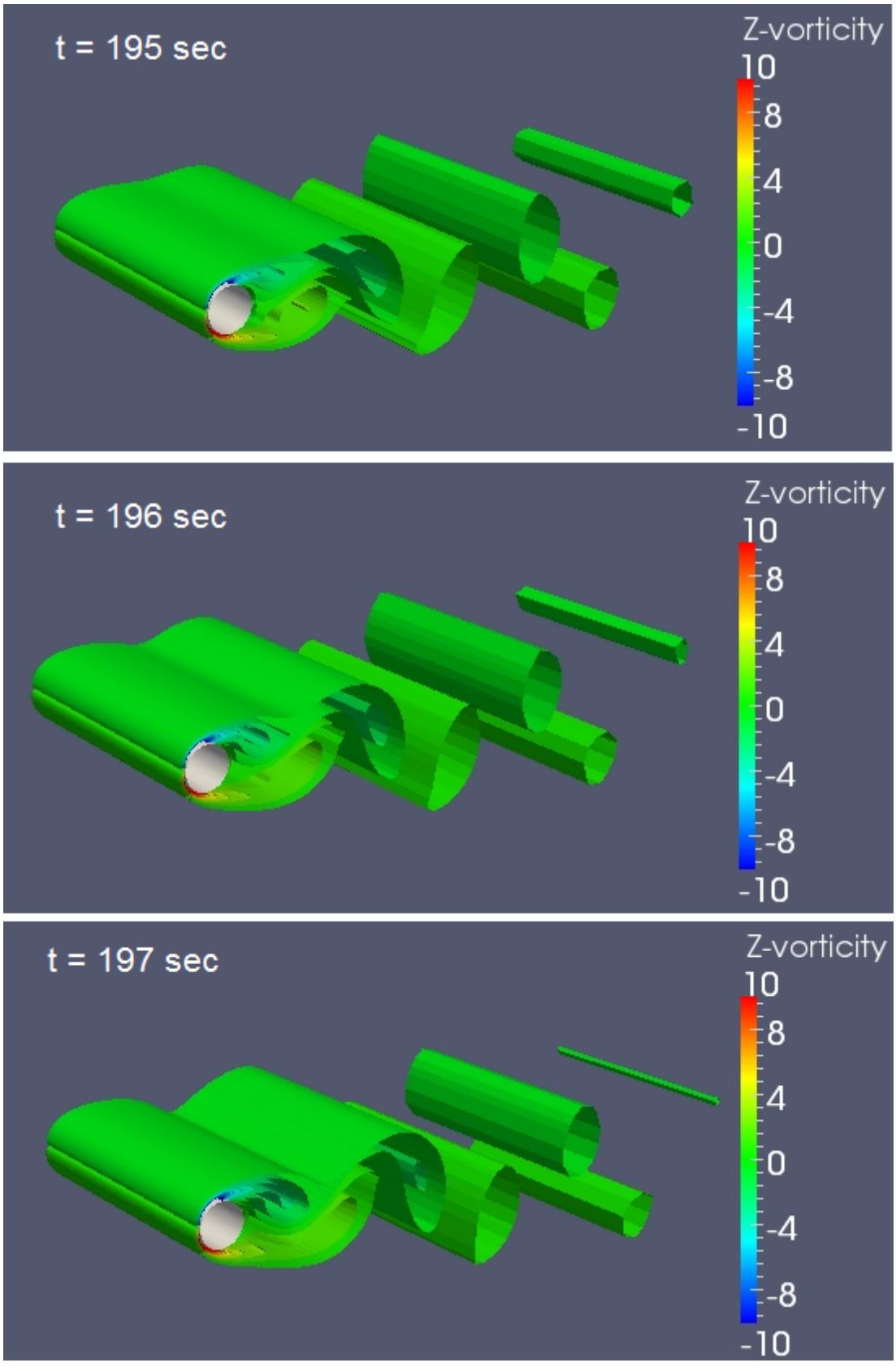
t = 195 sec
Z-vorticity
10
8
4
0
-4
-8
-10
t = 196 sec
Z-vorticity
10
8
4
0
-4
-8
-10
t = 197 sec
Z-vorticity
10
8
4
0
-4
-8
-10

Appendix D: Illustration of grids for a circular cylinder at $G/D = 0.2$

Grid C2 (top) and E1 (bottom)

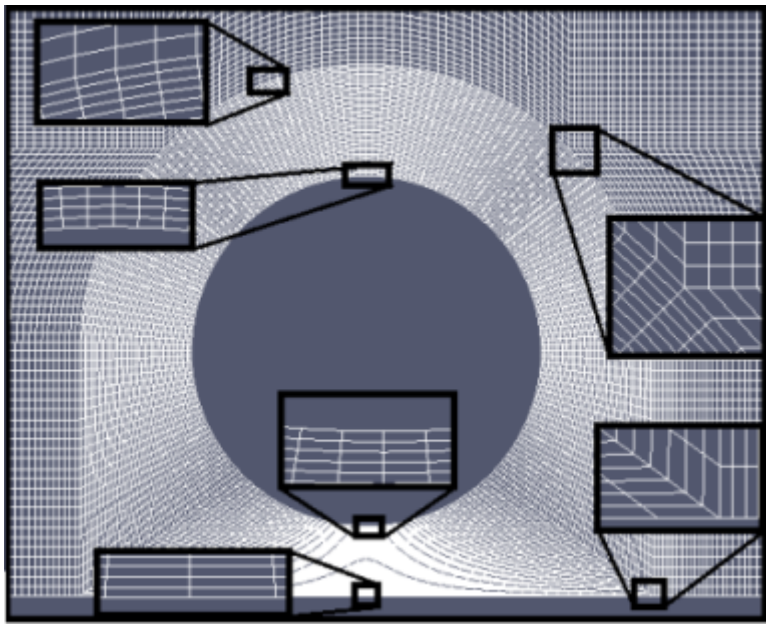

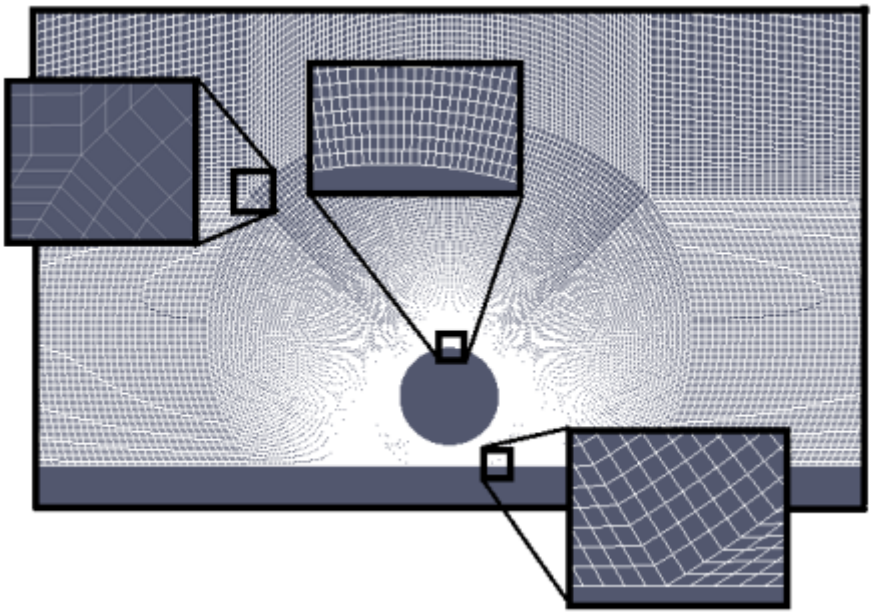

Appendix E: Time series of cross-sectional drag and lift coefficients for a circular cylinder at $G/D = 0.5$

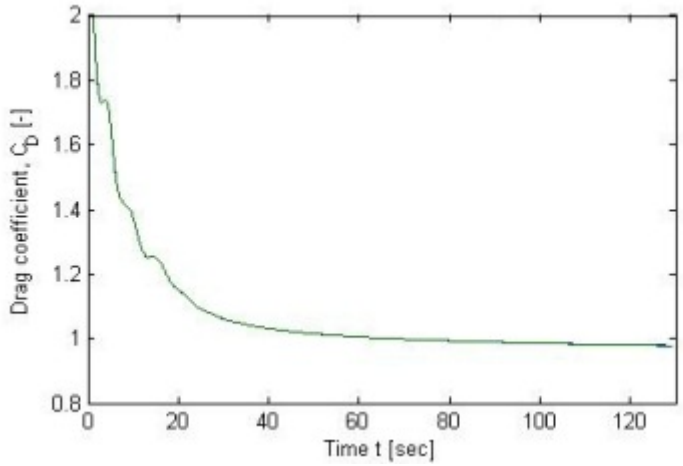

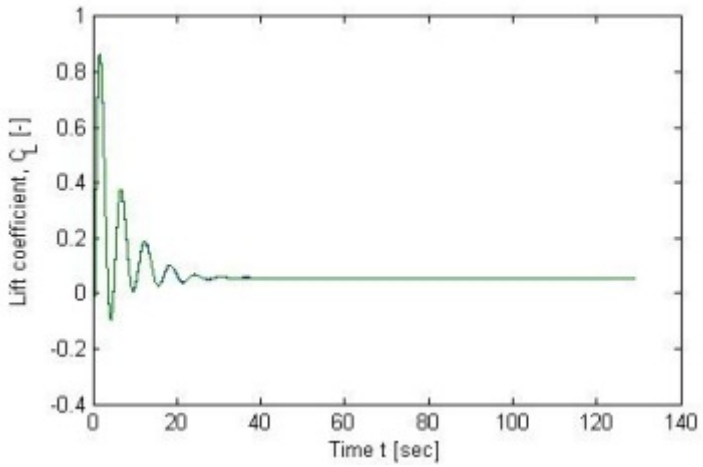

Appendix F: Stream-normal gradient of the horizontal velocity component at the wall with a circular cylinder at $G/D = 1.0$

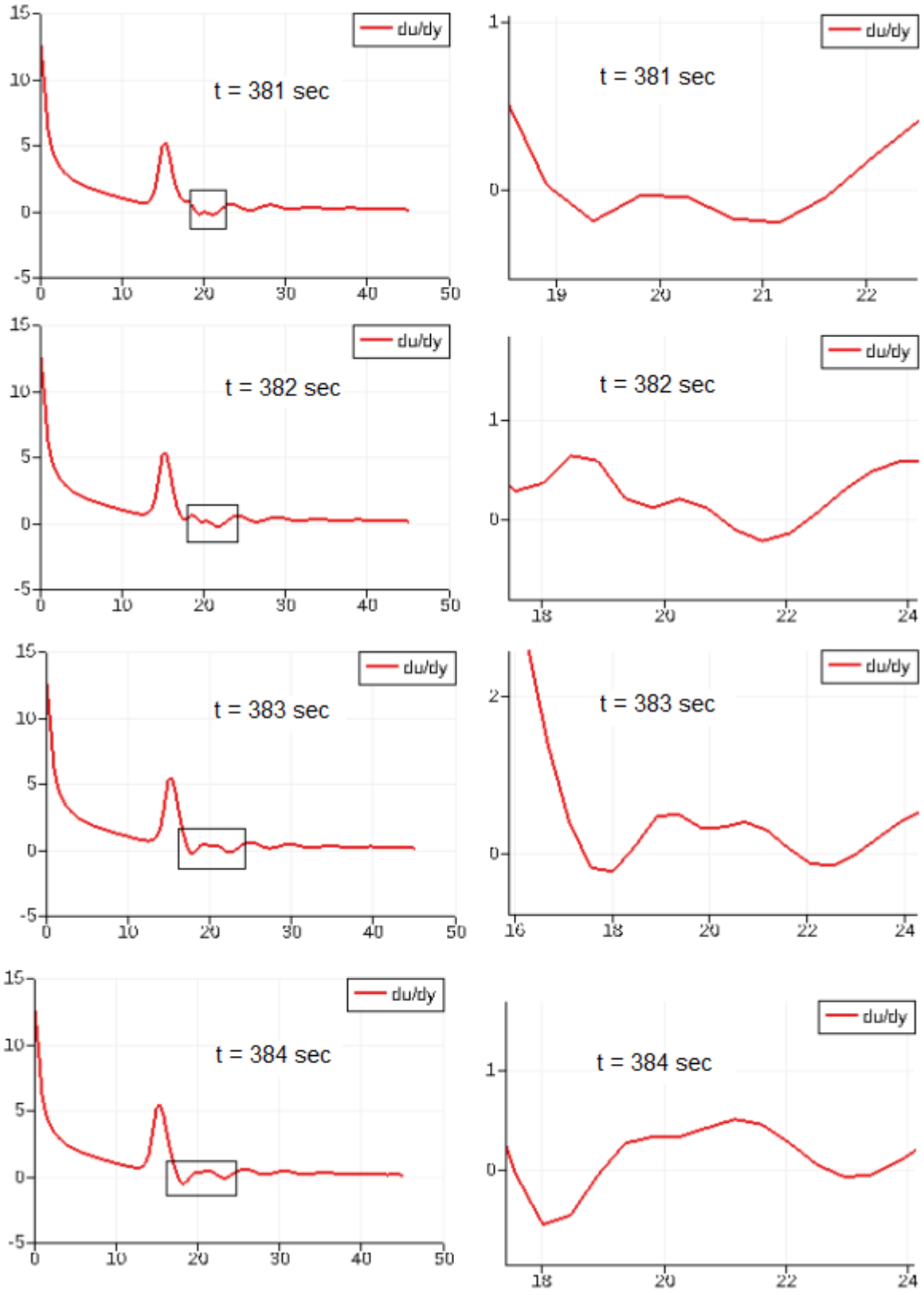

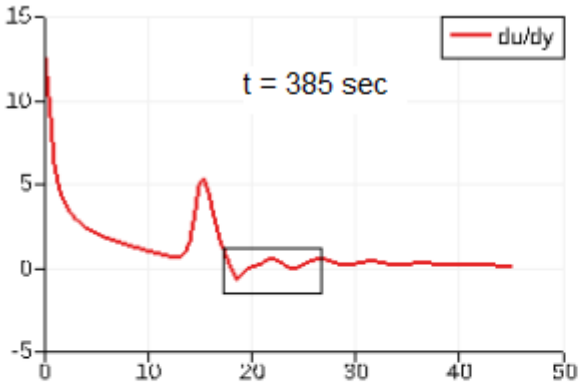
du/dy
t = 385 sec
15
10
5
0
-5
0
10
20
30
40
50

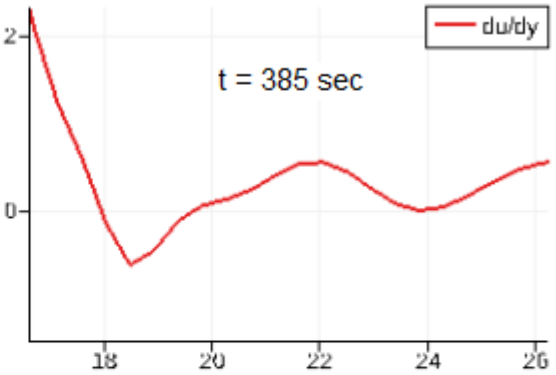
du/dy
t = 385 sec
2
0
18
20
22
24
26

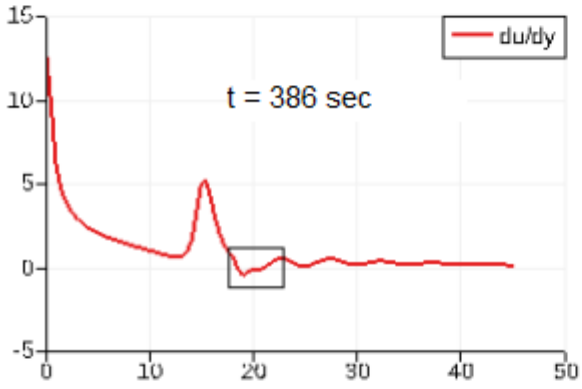
du/dy
t = 386 sec
15
10
5
0
-5
0
10
20
30
40
50

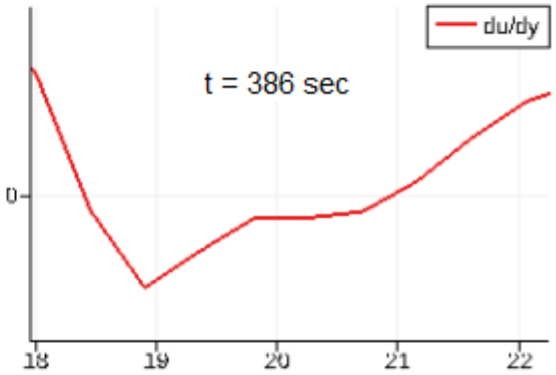
du/dy
t = 386 sec
0
18
19
20
21
22

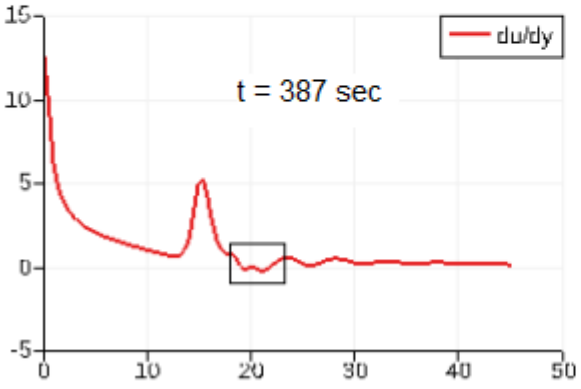
du/dy
t = 387 sec
15
10
5
0
-5
0
10
20
30
40
50

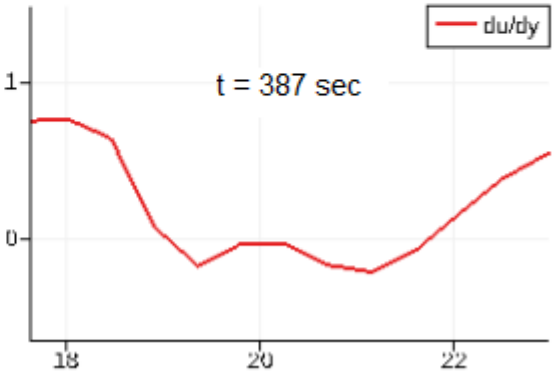
du/dy
t = 387 sec
1
0
18
20
22

Appendix G

Visualizations of the flow around a circular cylinder above a fully developed scour profile

Appendix G.1: Pressure distribution

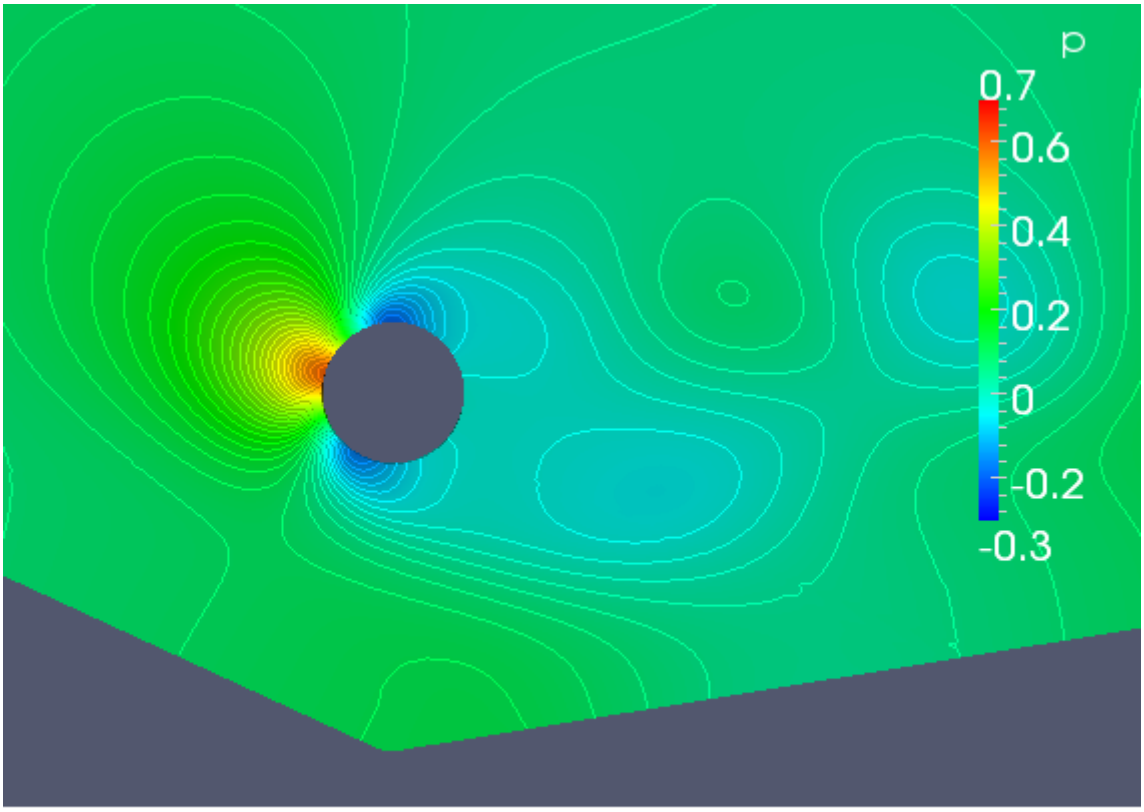

t = 581 sec

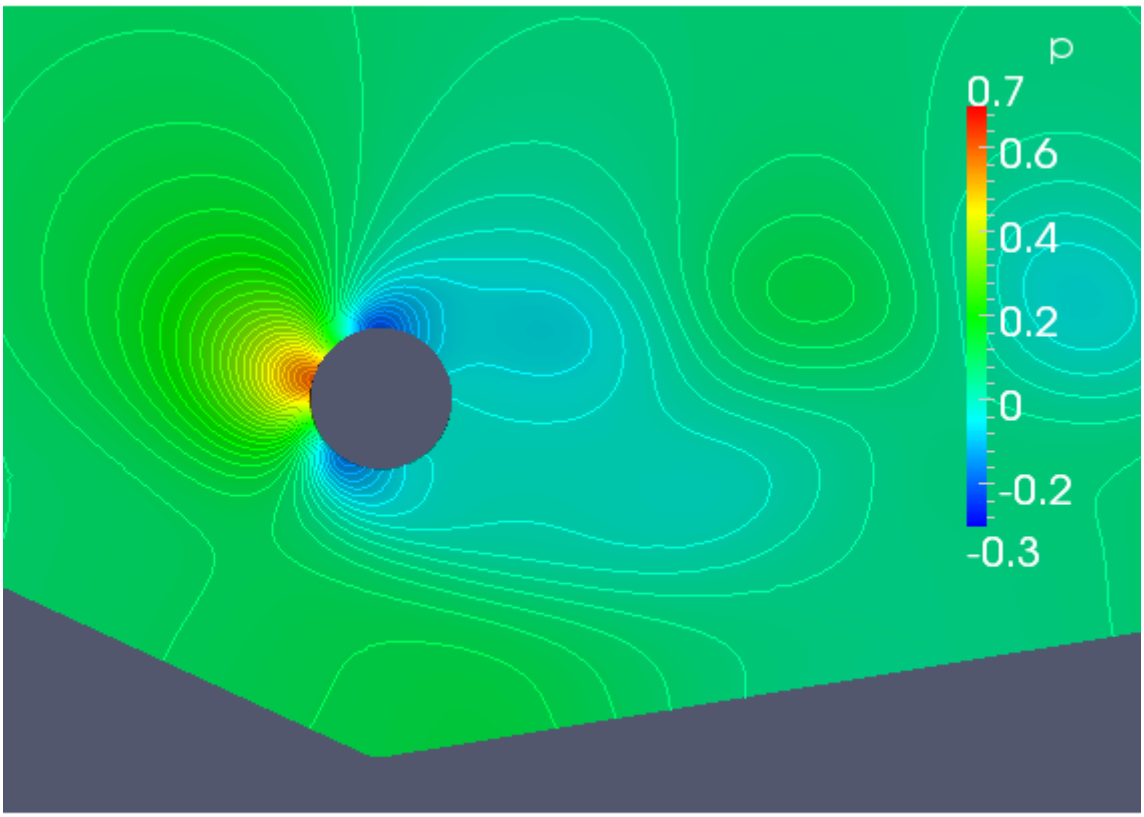

t = 582.5 sec

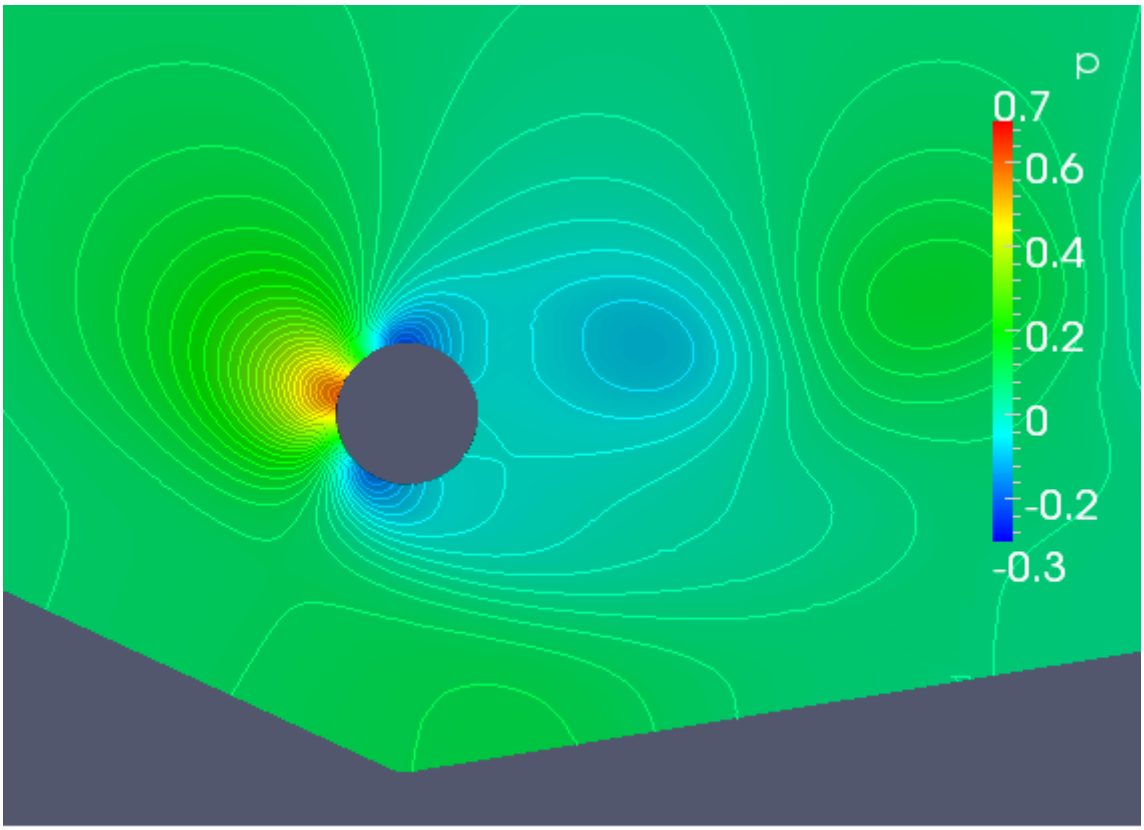

t = 584 sec

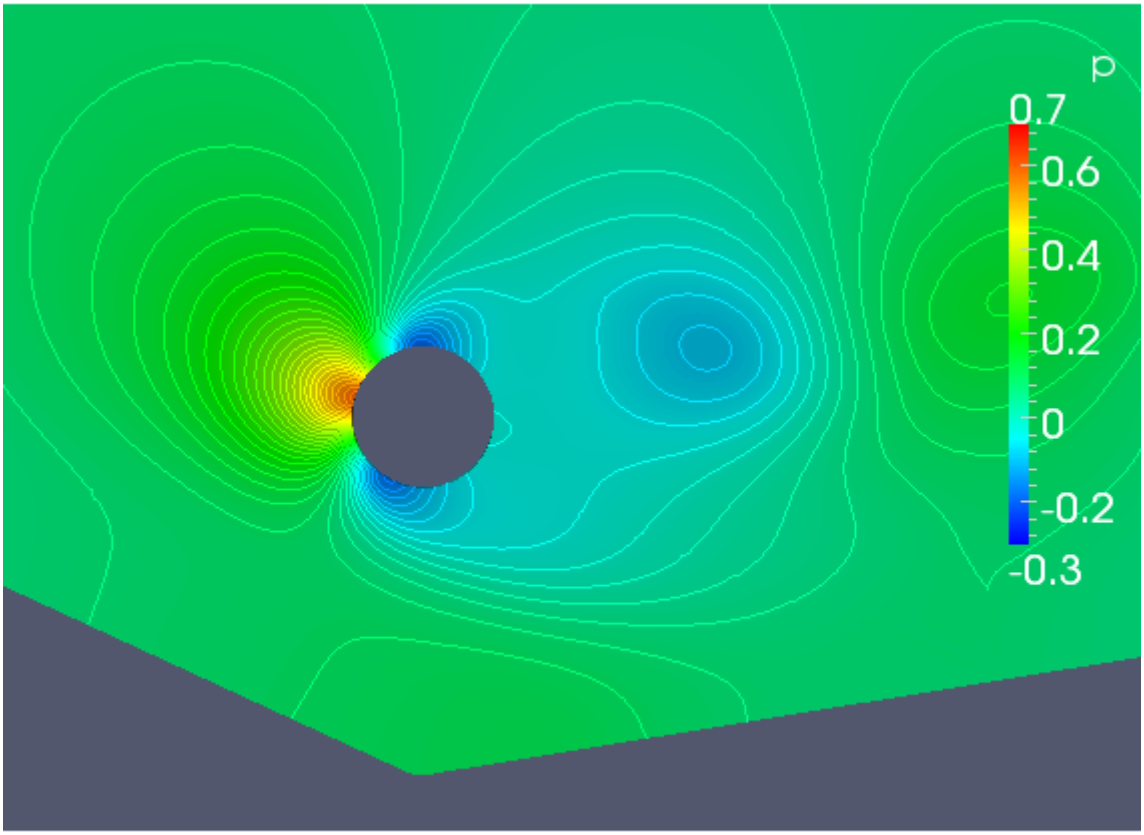

t = 585.5 sec

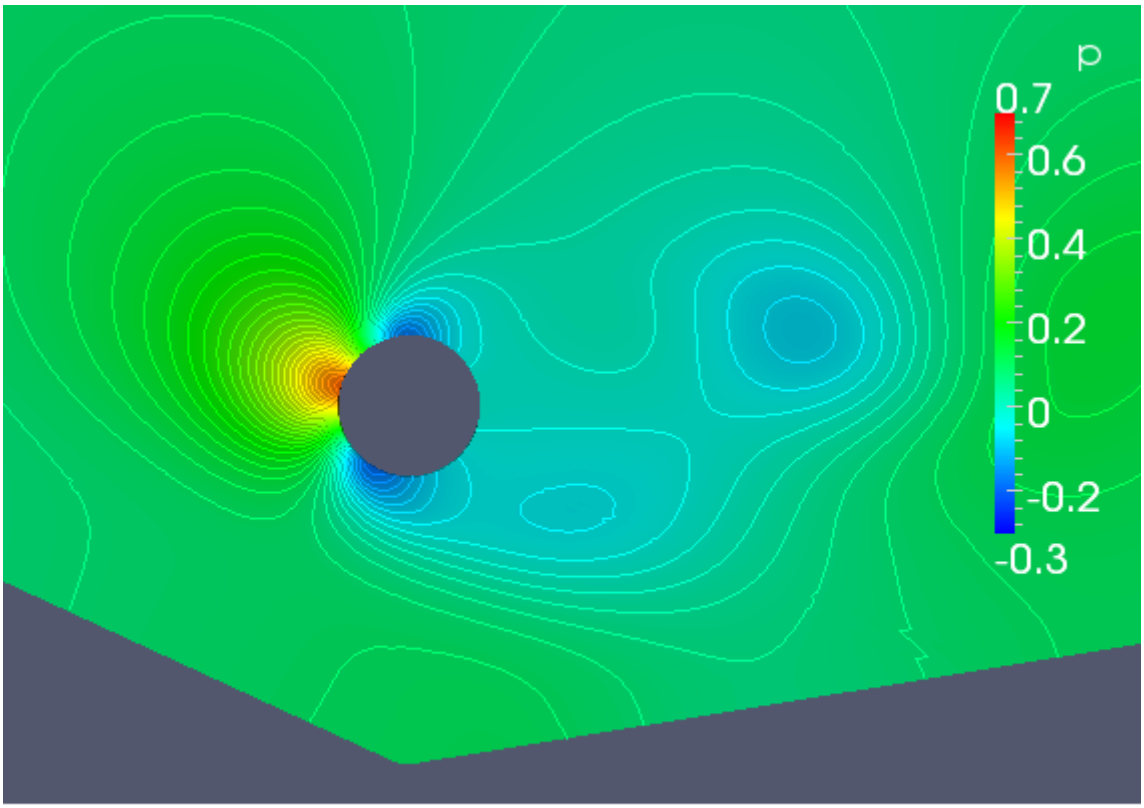

t = 587 sec

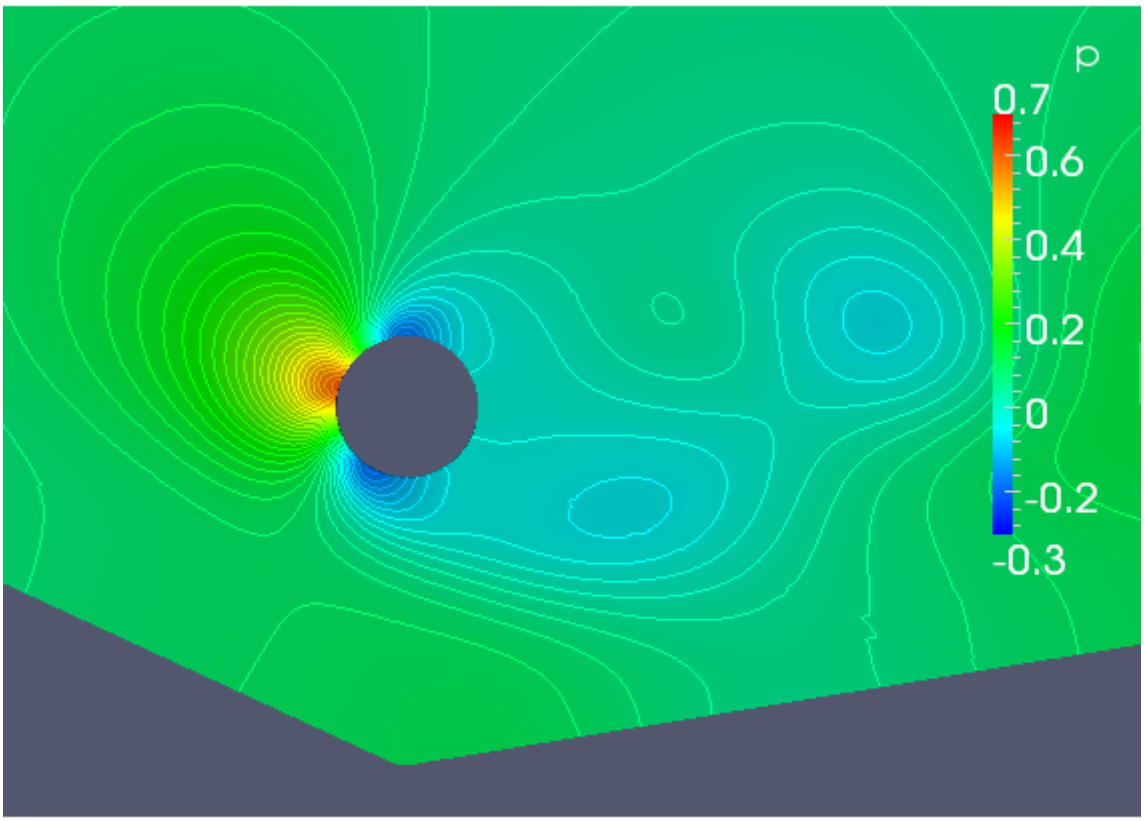

t = 588.5 sec

Appendix G.2: Velocity vectors in the upstream part of the scour hole

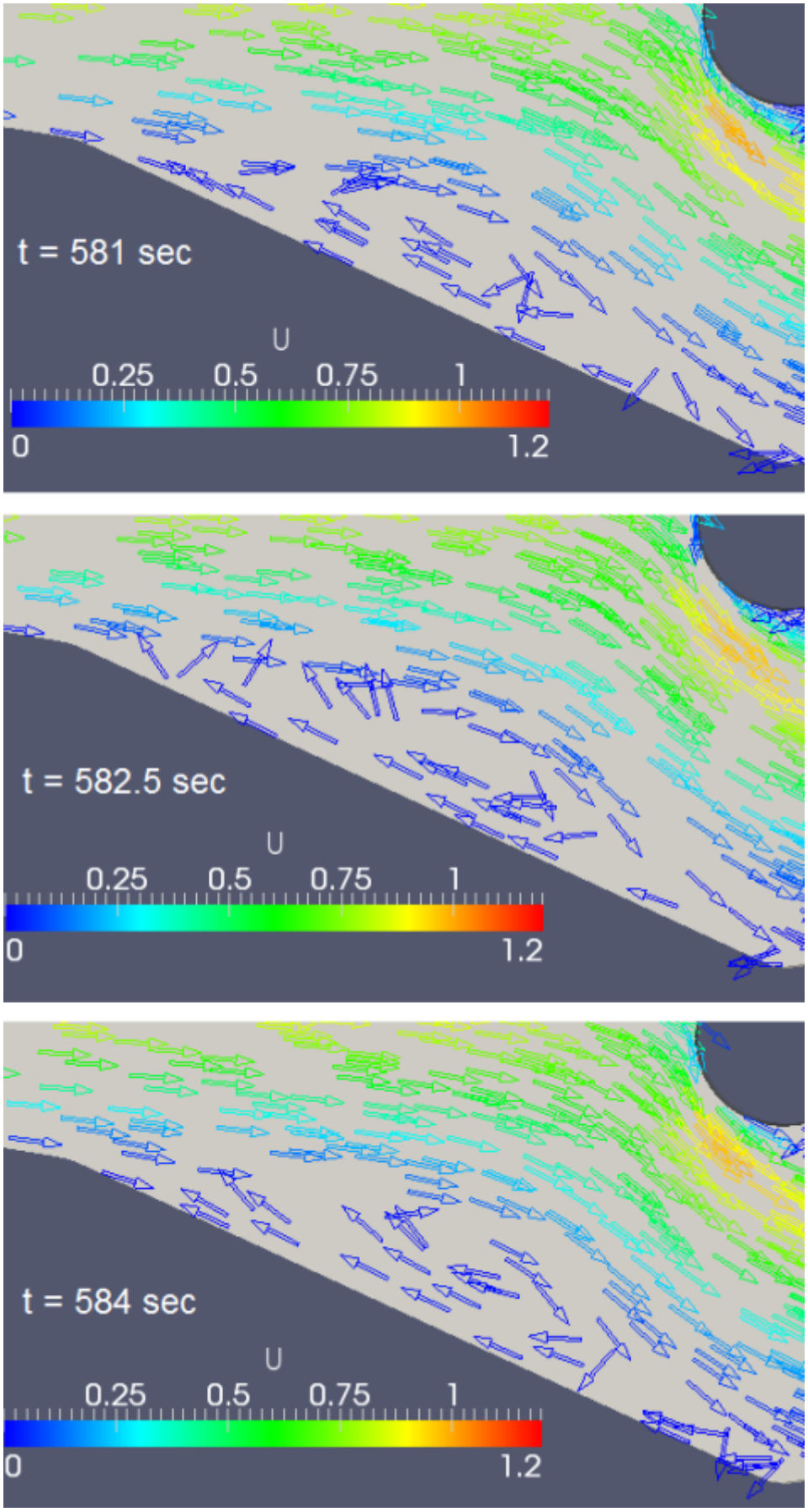

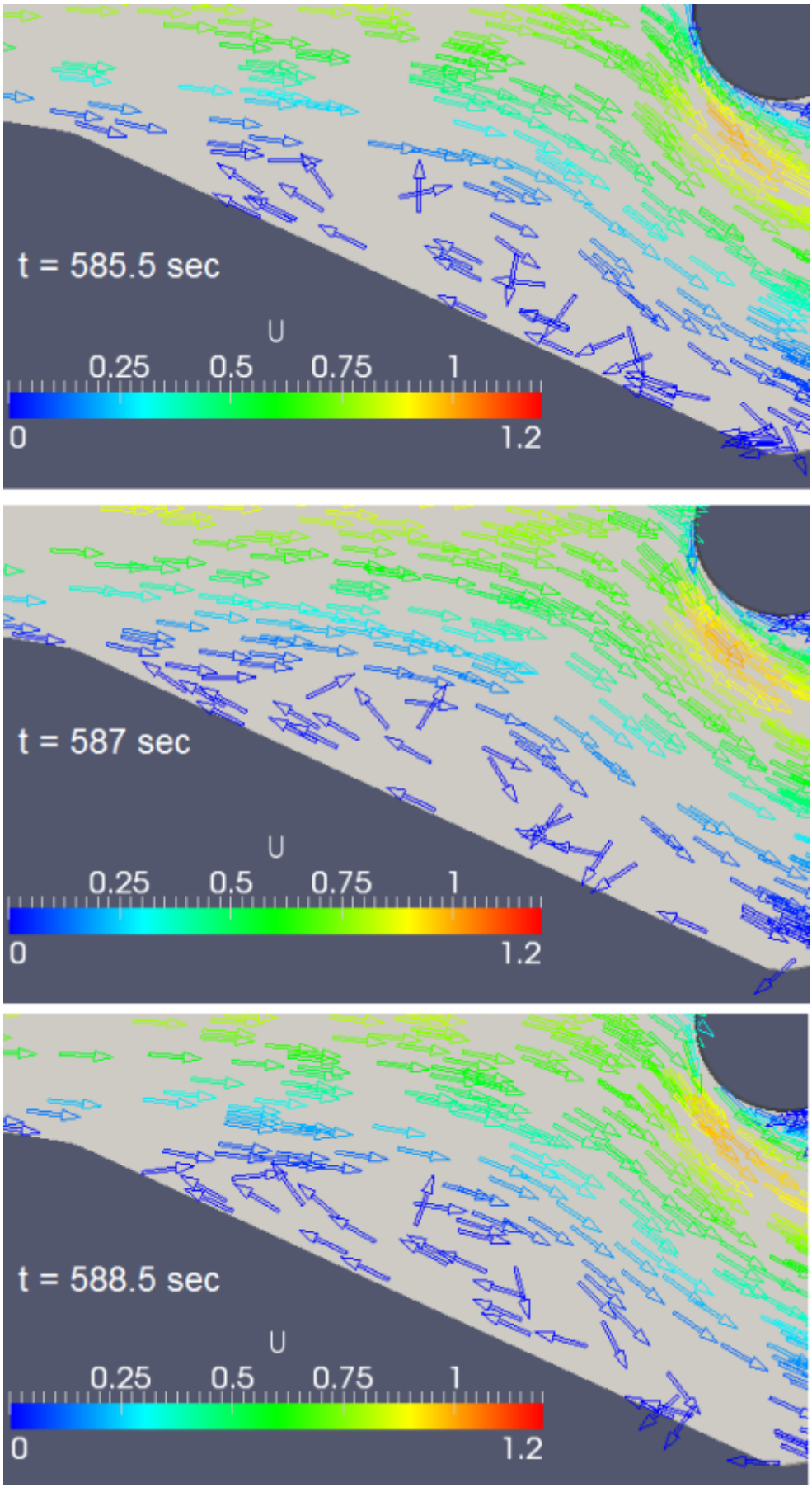
t = 585.5 sec
U
0.25
0.5
0.75
1
0
1.2
t = 587 sec
U
0.25
0.5
0.75
1
0
1.2
t = 588.5 sec
U
0.25
0.5
0.75
1
0
1.2

Appendix G.3: Velocity vectors in the downstream part of the scour hole

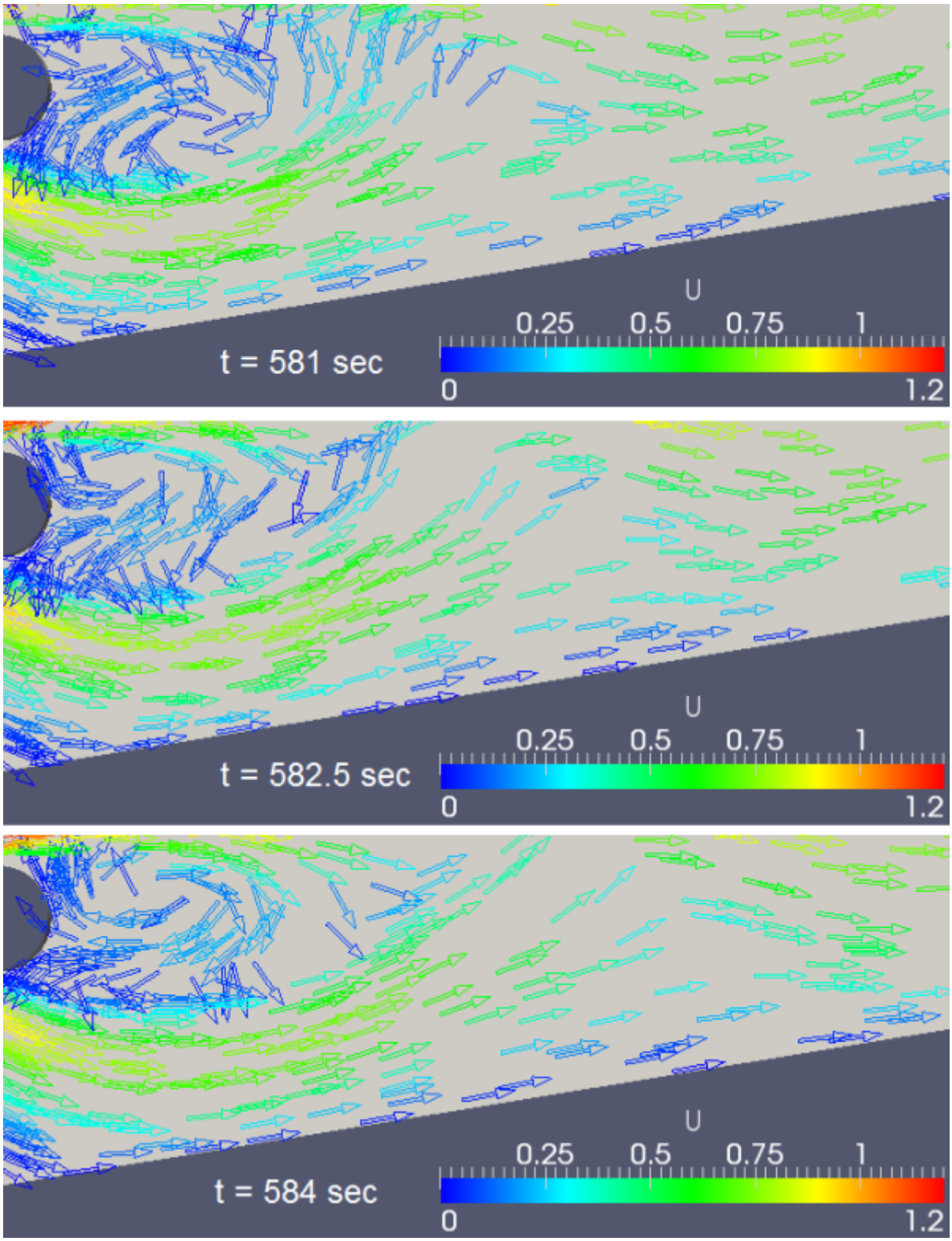

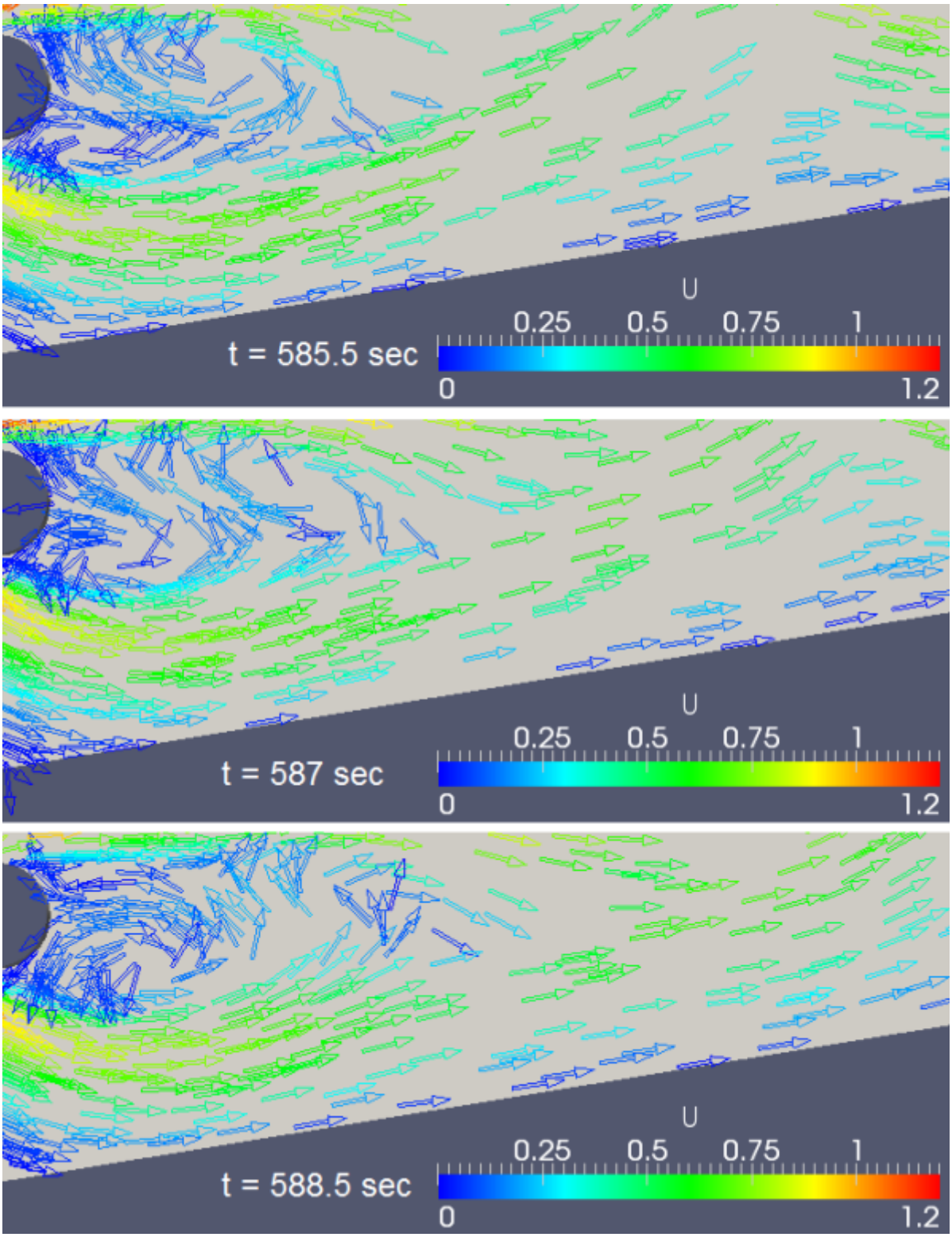
U
0.25
0.5
0.75
1
t = 585.5 sec
0
1.2
U
0.25
0.5
0.75
1
t = 587 sec
0
1.2
U
0.25
0.5
0.75
1
t = 588.5 sec
0
1.2

Appendix G.4: Vorticity contours in the near wake of a cylinder above a scour profile

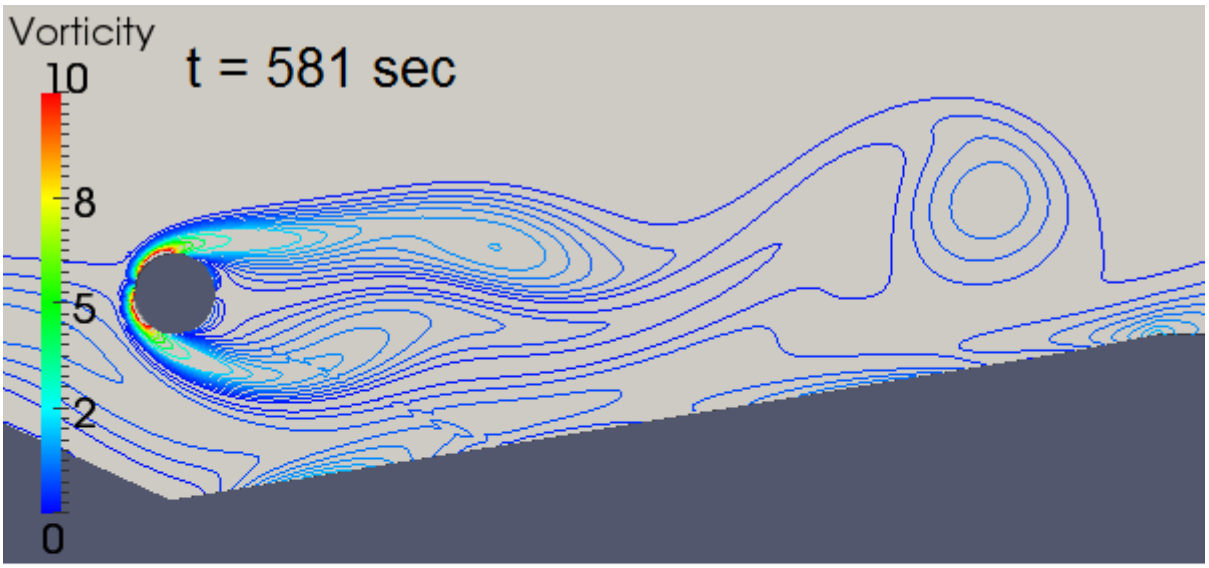

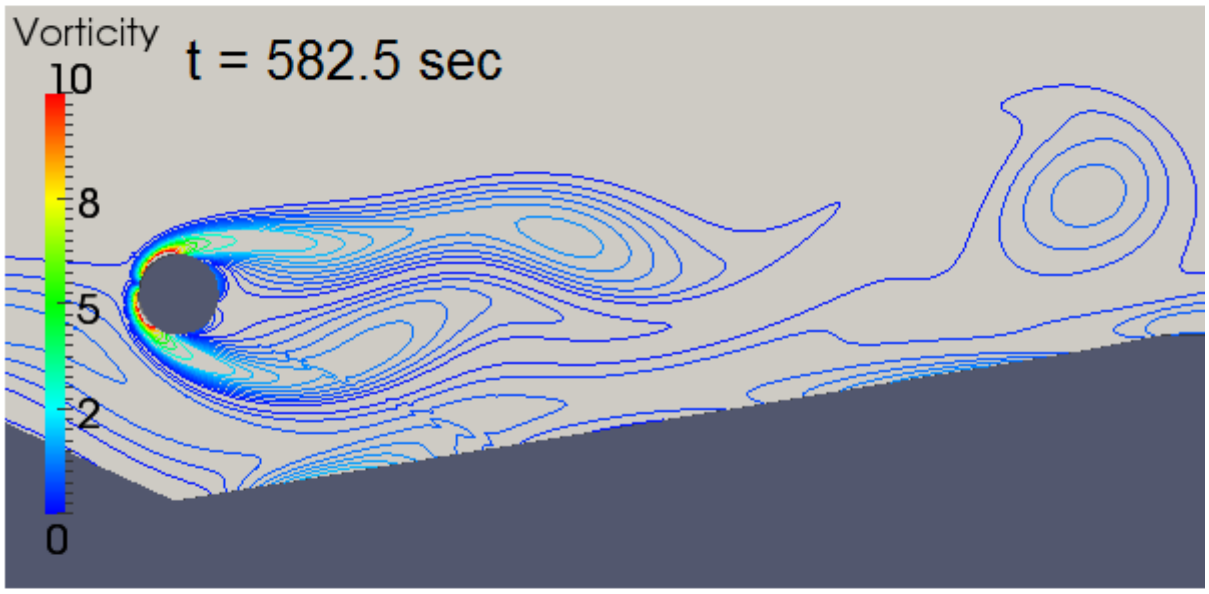

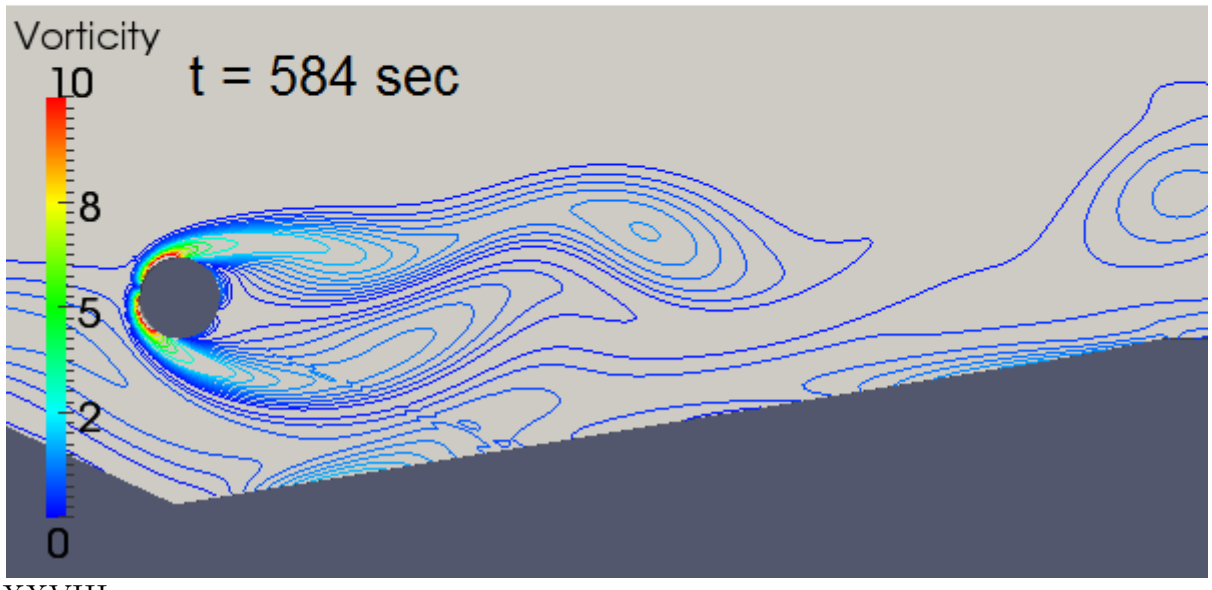

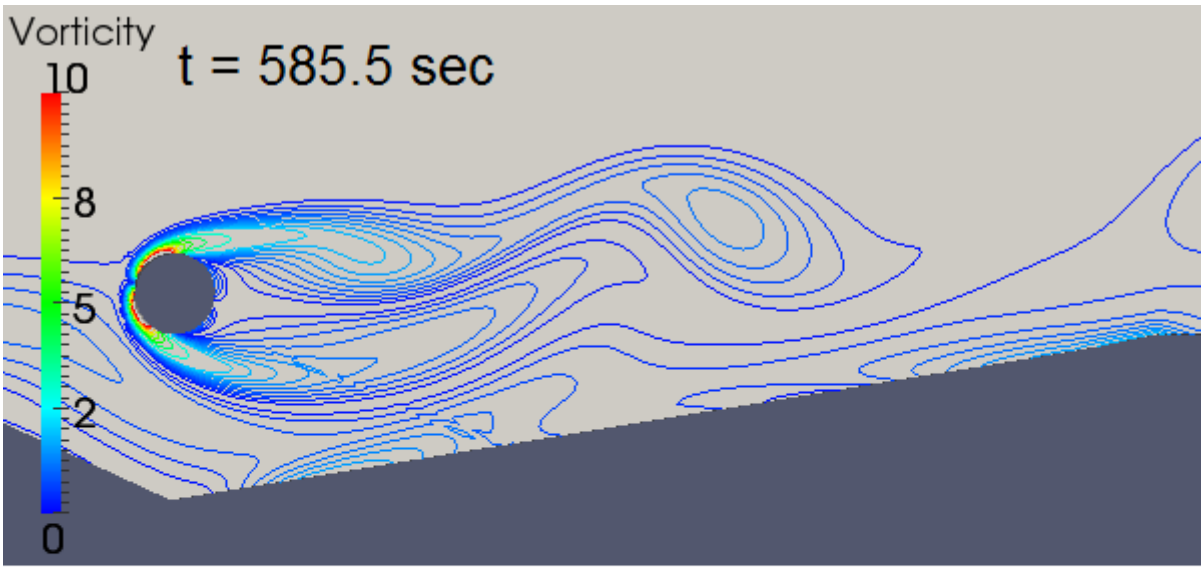
Vorticity
t = 585.5 sec
10
8
5
2
0

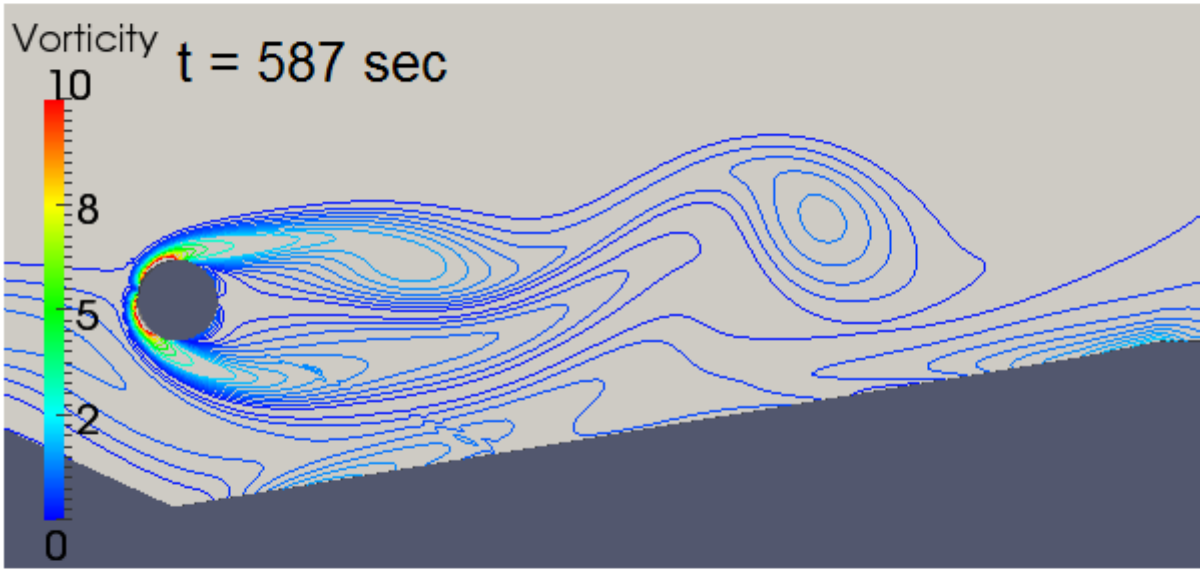
Vorticity
t = 587 sec
10
8
5
2
0

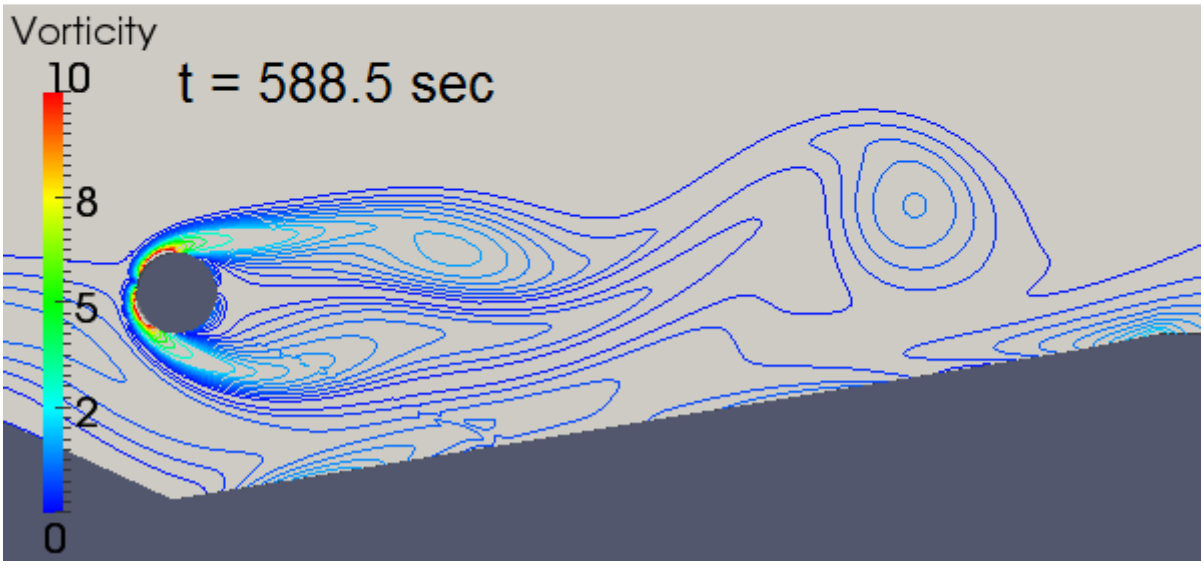
Vorticity
t = 588.5 sec
10
8
5
2
0